AFFDL-TR-79-3138
Volume I

CALCULATION OF HIGH SPEED INLET FLOWS USING THE NAVIER-STOKES EQUATIONS
Volume I:
Description of Results

DOYLE D. KNIGHT

DEPARTMENT OF MECHANICAL, INDUSTRIAL AND
 AEROSPACE ENGINEERING
RUTGERS UNIVERSITY   THE STATE UNIVERSITY OF NEW JERSEY
NEW BRUNSWICK, NEW JERSEY 08903

FEBRUARY 1980

Approved for public release; distribution unlimited.

AIR FORCE FLIGHT DYNAMICS LABORATORY
AIR FORCE WRIGHT AERONAUTICAL LABORATORIES
AIR FORCE SYSTEMS COMMAND
WRIGHT-PATTERSON AIR FORCE BASE, OHIO 45433
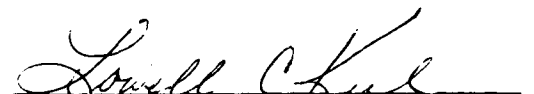
80 5 22 005

PROJECT ENGINEER

LOWELL C. KEEL, MAJOR, USAF
Chief, Aerodynamics & Airframe Br.
Aeromechanics Division

FOR THE COMMANDER

PETER J. BUTKEWICZ, Colonel, USAF
Aeromechanics Division

REPORT DOCUMENTATION PAGE	READ INSTRUCTIONS BEFORE COMPLETING FORM

1. REPORT NUMBER	2. GOVT ACCESSION NO.	3. RECIPIENT'S CATALOG NUMBER
AFFDL-TR-79-3138 - VOL -1	AD-A084 789	

4. TITLE (and Subtitle)	5. TYPE OF REPORT & PERIOD COVERED
CALCULATION OF HIGH SPEED INLET FLOWS USING THE NAVIER-STOKES EQUATIONS. VOLUME I. DESCRIPTION OF RESULTS	Final Report, April 1978-Sep 1979
	6. PERFORMING ORG. REPORT NUMBER

7. AUTHOR(s)	8. CONTRACT OR GRANT NUMBER(s)
Doyle D. Knight	F33615-78-C-3008

9. PERFORMING ORGANIZATION NAME AND ADDRESS	10. PROGRAM ELEMENT, PROJECT, TASK AREA & WORK UNIT NUMBERS
Department of Mechanical, Industrial and Aerospace Engineering Rutgers University, New Brunswick, New Jersey 08903	Program Element 61102F Work Unit No. 2307N415

11. CONTROLLING OFFICE NAME AND ADDRESS	12. REPORT DATE
Air Force Flight Dynamics Laboratory (FXM) Wright-Patterson AFB, Ohio 45433	February 1980
	13. NUMBER OF PAGES 112

14. MONITORING AGENCY NAME & ADDRESS(If different from Controlling Office)	15. SECURITY CLASS. (of this report)
	Unclassified
	15a. DECLASSIFICATION/DOWNGRADING SCHEDULE

16. DISTRIBUTION STATEMENT (of this Report)

Approved for public release; distribution unlimited

17. DISTRIBUTION STATEMENT (of the abstract entered in Block 20, If different from Report)

18. SUPPLEMENTARY NOTES

Presented at the AIAA 18th Aerospace Sciences Meeting at Pasadena, California in January 1980.

19. KEY WORDS (Continue on reverse side If necessary and Identify by block number)

High Speed Inlets
Computational Fluid Dynamics
Navier-Stokes Equations
Shock-Boundary Layer Interaction
Surface-Oriented Coordinates

20. ABSTRACT (Continue on reverse side If necessary and Identify by block number)

A set of computer programs has been developed to calculate the flowfield in two-dimensional mixed-compression high speed inlets. The full mean compressible Navier-Stokes equations are utilized, with turbulence represented by an algebraic eddy viscosity model which incorporates a relaxation correction. A curvilinear body-oriented coordinate system is employed to allow handling of arbitrary inlet contours. Boundary layer bleed is incorporated.

DD FORM 1473 EDITION OF 1 NOV 65 IS OBSOLETE
S/N 0102-LF-014-6601

The numerical algorithm of MacCormack is employed to solve the Navier-Stokes equations. A variety of techniques are incorporated to improve code efficiency, including time-splitting of the finite-difference operators, automatic mesh-splitting, and a separate algorithm for the treatment of the viscous sublayer portion of the turbulent boundary layers.

The numerical codes have been successfully applied to the calculation of a variety of flows including shock-boundary layer interaction on a flat plate (including both unseparated and separated cases), and three different simulated high speed inlet configurations. In all cases, good agreement was obtained with the experimental data.

The numerical codes represent a substantial improvement in computational efficiency. For a Mach 3.5 inlet at a Reynolds number of 13 million, the typical computer time on the CYBER 175 is two to four hours, depending on the amount of internal compression. This represents a decrease of approximately an order of magnitude compared to the author's previous work.

FOREWORD

A set of four user-oriented computer programs have been
developed to calculate the flowfield in two-dimensional mixed-
compression high speed inlets. The full mean compressible
Navier-Stokes equations are employed, with turbulence represented
by an algebraic turbulent eddy viscosity model. The method is
capable of handling arbitrary inlet contours through use of a
numerical body-oriented coordinate transformation.

The method has been successfully applied to a variety of
flows including the interaction of an oblique shock with a
boundary layer on flat plate, and three different simulated
high speed inlet configurations.

The results of the calculations are presented in Volume I.
Details of the numerical algorithms and information on the use
of the computer programs are provided in Volume II.

This report was prepared by Prof. Doyle Knight, Department
of Mechanical Engineering, Rutgers University, New Brunswick, New
Jersey, for the Air Force Flight Dynamics Laboratory, Air Force
Systems Command, Wright-Patterson AFB, Ohio. The study was
performed under Air Force Contract F33615-78-C-3008, "Analytical
Investigation of Inlet Internal Flow." The work was performed
from April 1978 through September 1979, with Mr. Don Stava
(AFFDL/FXM) of the Air Force Flight Dynamics Laboratory as Project
Engineer. The report was submitted in September 1979.

TABLE OF CONTENTS

LIST OF FIGURES

LIST OF FIGURES--CONTINUED

LIST OF TABLES

NOMENCLATURE

(Volumes I and II)

C	geometric mesh stretching factor; constant in compressible Law of the Wall
C_1, C_2	mesh stretching parameters
c	speed of sound
c_f	skin friction coefficient
c_p	specific heat at constant pressure
c_v	specific heat at constant volume
D	Van Driest damping factor
e	total energy per unit mass
e_i	internal energy per unit mass
$\bar{F}$	flux vector in ζ-direction
G	flux vector in η-direction
IL	number of mesh points in ζ-direction
J	Jacobian $\zeta_x \eta_y - \zeta_y \eta_x$
JL	number of mesh points in η-direction
JSL∅	number of mesh points in CSL on $\eta = 0$
JSL1	number of mesh points in CSL on $\eta = 1$
k_2	constant in eddy viscosity, $\kappa_2 = .0168$
L	finite-difference operator
L_ζ	finite-difference operator in ζ-direction
L_η	finite difference operator in η-direction
$\dot{m}$	bleed mass flux (units: mass/area – time)
M	Mach number
$\vec{n}$	unit normal on boundary

n	normal distance to boundary
N	modification to D due to mass bleed
Pr	molecular Prandtl number
Pr_t	turbulent Prandtl number
p	static pressure
P_p	pitot pressure
P_t	total pressure
R	gas constant
$°R$	degrees Rankine
Q_x, Q_y	cartesian components of heat transfer vector
$Q_{x'}$, $Q_{y'}$	components of heat transfer vector in locally orthogonal coordinates in CSL
$\vec{s}$	unit tangent vector on boundary
s	arc length along boundary from leading edge
T	static temperature
$T(\xi,\eta)$	coordinate stretching function
T_t	total temperature
t	time
t_c	characteristic time (i.e., the time required for a fluid particle in the inviscid region to travel from the upstream to the downstream boundary of a computational region)
U	vector of dependent variables
U	contravariant velocity component
u	velocity parallel to boundary
u	x component of vleocity
u'	velocity parallel to boundary in CSL

u_*	friction velocity $\sqrt{\tau_w/\rho_w}$
V	contravariant velocity component
v	y component of velocity
v'	velocity normal to boundary in CSL
x	cartesian coordinate
x'	distance parallel to boundary in CSL
y	cartesian coordinate
y'	distance normal to boundary in CSL
y'_m	height of CSL region

Greek Symbols

α	pressure damping coefficient; expression in coordinate transformation equation
β	damping coefficient; expression in coordinate transformation equation
Γ	transition factor
γ	ratio of specific heats; expression in coordinate transformation equation
Δx	mesh spacing in x-direction (variable)
Δy	mesh spacing in y-direction (variable)
t	time step
Δt_ζ	time step for L_ζ operator
Δt_η	time step for L_η operator
$\Delta \zeta$	mesh spacing in ζ-direction (constant)
$\Delta \eta$	mesh spacing in η-direction (constant)
δ	boundary layer thickness; expression in coordinate transformation equation

δ_0	boundary layer thickness at start of eddy viscosity relaxation; also at station immediately upstream of SBLI
δ_c	cowl angle
δ_i^*	"incompressible" displacement thickness
ε	turbulent eddy viscosity
ε_{eq_i} ε_{eq_o}	equilibrium eddy viscoisty
ζ	transformed coordinate
η	transformed coordinate
η_1, η_2	quantities in coordinate stretching
θ	angle of inclination of surface; incident shock angle; compressible displacement thickness
κ	Von Kármán's constant
Λ	parameter in transition model
λ	relaxation length in turbulent eddy viscosity model
λ_T	second coefficient of total viscosity $-\frac{2}{3}(\mu + \varepsilon)$
μ	dynamic molecular viscosity; Mach angle
ν	kinematic viscoisty
ξ	direction of characteristic
ρ	density
τ_{xx}, τ_{xy}, τ_{yy}	components of cartesian stress tensor in x,y coordinate system
τ_w	wall shear stress
$\tau_{x'x'}$, $\tau_{x'y'}$, $\tau_{y'y'}$	components of cartesian stress tensor in x',y' coordinate system
ω	acceleration parameter used in solution of coordinate transformation

NOMENCLATURE--<u>Continued</u>

Subscripts

e   evaluated at the edge of the boundary layer

m   evaluated at row of matching points

w   evaluated at the boundary

∞ evaluated upstream of the inlet entrance

Abbreviations

CSL   computational sublayer

MCAIR   McDonnell Aircraft Company

SBLI   shock-boundary layer interaction

SIP   shock impingement point

SECTION I

INTRODUCTION

The prediction of inlet performance is an important element in the
design of high speed aircraft. In the case of turbofan propulsion, the
function of the inlet is to provide an approximately uniform subsonic flow
with high total pressure recovery at the compressor face. A concurrent
objective is to minimize the drag penalties associated with inlet cowl lip
geometry, boundary layer bleed and bypass bleed flow.[1] A typical two-
dimensional mixed-compression high speed inlet[2] is shown in Figure 1. The
incoming supersonic flow is deflected by a pattern of oblique shock waves
formed by the general curvilinear shape of the ramp and cowl surfaces. The
shock wave train is terminated by an approximately normal shock (denoted as
the "terminal shock") which is typically positioned near the inlet throat.
The boundary layers on the ramp and cowl are turbulent over nearly the entire
length of the inlet owing to the typically high Reynolds numbers. Boundary
layer bleed is distributed in general along the ramp, cowl and sidewalls in
order to prevent flow separation at the intersection of the shock waves and
boundary layers.

Traditionally, the basic approach to theoretical inlet design and
analysis has been based on the separate, and sometimes coupled, treatment of
the inviscid and viscous portions of the inlet flow. The calculation of the
inviscid flow is accomplished either by the conventional method of charac-
teristics,[3,4] or inviscid finite-difference shock-capturing techniques.[5] The
effect of the boundary layer displacement thickness is either ignored,[6] or
incorporated as a correction.[7]. The calculation of the wall boundary layers
typically involves a finite-difference solution of the boundary layer
equations with a semi-empirical model of shock-boundary layer interaction.[7,8]
The determination of boundary layer bleed necessary to prevent flow
separation is typically achieved by means of empirical criteria based on the
velocity profile.[8,9]

The traditional approach, however, suffers from several major disadvan-
tages. First of all, the use of semi-empirical models of shock-boundary
layer interaction oftentimes yields incorrect predictions of the reflected
shock wave structure and subsequent unreliable performance predictions.[7,10]
Secondly, the conventional method of characteristics and inviscid finite-

1

difference shock-capturing techniques are limited to regions of supersonic flow.[3-5,7] In practice, both techniques perform a marching operation in the direction of the flow beginning at the inlet entrance. The development of any region of subsonic flow terminates the computation, which in practice may sometimes occur upstream of the inlet throat.[5,7] Of course, the interaction of the terminal shock with the boundary layers and the subsonic diffuser flowfield cannot be treated by these techniques. Thirdly, these methods are incapable of handling flow separation due to their inadequate modeling of strong viscous-inviscid interaction. The presence of large flow separation within inlets at high angle of attack is a major concern for aircraft designers.[11]

The result of this research is the development of a set of user-oriented computer programs which provide efficient computation of the flowfields of two-dimensional mixed compression high speed inlets, while overcoming the disadvantages of the traditional approach. The procedure is based on the solution of the full Navier-Stokes equations. The capability for calculation of high speed flows with strong viscous-inviscid interaction using the Navier-Stokes equations has been demonstrated in recent years for a variety of flows. A brief summary of results includes shock-boundary layer interaction on a flat plate,[12,13] supersonic flow in a compression corner,[14-16] three-dimensional high speed corner flow,[17] steady and unsteady transonic flows,[18,19] and high speed inlets.[20] The current method utilizes a body-oriented coordinate system, capable of handling arbitary inlet geometries, and permits arbitrary specification of boundary layer bleed on the ramp and cowl. The effects of turbulence are represented by an algebraic turbulent eddy viscosity, including a correction for the effects of the relaxation of the turbulence structure in the vicinity of strong viscous-inviscid interaction.

SECTION II

GOVERNING EQUATIONS

A. Coordinate Transformation

The general curvilinear shape of the inlet surfaces suggests the use of a surface-oriented coordinate transformation. As indicated schematically in Figure 2, a set of curvilinear coordinates $\zeta(x,y)$ and $\eta(x,y)$ are generated in the physical plane and effectively map the computational domain into the unit square in the transformed plane. The cowl and ramp surfaces are taken to be coincident with portions of the contours $\eta(x,y) = 0$ and $\eta(x,y) = 1$, respectively. The upstream and downstream boundaries of the computational domain are defined by the lines $\zeta(x,y) = 0$ and $\zeta(x,y) = 1$, respectively.

The coordinates are obtained using the basic approach of Thompson,[21] in which $\zeta(x,y)$ and $\eta(x,y)$ are determined by solution of the following Poisson equations

$$\nabla^2 \zeta = P(\zeta,\eta)$$
$$\nabla^2 \eta = Q(\zeta,\eta) \tag{1}$$

where ∇^2 is the Laplacean operator $\partial^2/\partial x^2 + \partial^2/\partial y^2$ and the functions P and Q are constructed in order to control the distribution of mesh points in the physical plane. In the present case, the following forms, utilized in previous investigations,[20] have been chosen:

$$P(\zeta,\eta) = 0 \tag{2}$$

$$Q(\zeta,\eta) = T(\zeta,\eta) \left[\left(\frac{\partial \eta}{\partial x}\right)^2 + \left(\frac{\partial \eta}{\partial y}\right)^2 \right]$$

where $T(\zeta,\eta)$ is taken to be

$$T(\zeta,\eta) = \begin{cases} - C_1/\eta_1 & 0 \leq \eta \leq \eta_1 \\ 0 & \eta_1 < \eta < \eta_2 \\ + C_2/(1 - \eta_2) & \eta_2 \leq \eta \leq 1 \end{cases} \tag{3}$$

In the above expression, the quantities C_1 C_2, η_1, and η_2 are slowly-varying functions of ζ. The effect of the expressions (2) and (3) is to produce approximately uniform mesh spacing in the streamwise or ζ-direction, an exponentially stretched mesh in the η-direction in the vicinity of the

lower and upper surfaces (i.e., within the regions $0 \leq \eta \leq \eta_1$ and $\eta_2 \leq \eta \leq 1$), and a uniform mesh spacing in the η-direction in the interior (i.e., $\eta_1 < \eta < \eta_2$). The quantities η_1, η_2, C_1 and C_2 are determined by the requirements of accurate resolution of the boundary layers on the ramp and cowl and controllable mesh spacing near the walls. Full details are given in Reference 22.

The coordinates $\zeta(x,y)$ and $\eta(x,y)$ are subject to Dirichlet boundary conditions, as indicated in Figure 2 (e.g., $\zeta = 0$ on the upstream boundary, etc.). The coordinate transformation is not necessarily orthogonal, although for typical inlet geometries an approximately orthogonal transformation can be obtained by judicious distribution of the mesh points on the ramp and cowl surfaces. The numerical algorithm employed for solution of the Navier-Stokes equations permits general non-orthogonal coordinate transformations. However, an approximately orthogonal coordinate transformation is desirable, for example, within the boundary layers in order to avoid the excessive truncation errors that may be introduced by highly skewed coordinates. Full details of the numerical solution of equations (1) are provided in Reference 22.

B. Inlet Flowfield

1. Navier-Stokes Equations

The governing equations are the full mean compressible Navier-Stokes equations utilizing mass-averaged variables[23] for two-dimensional turbulent flow. Written in strong conservation form, the equations are[24,25]

$$\frac{\partial U}{\partial t} + \frac{\partial F}{\partial \zeta} + \frac{\partial G}{\partial \eta} = 0 \tag{4}$$

where

$$U = \left\{ \begin{array}{c} \rho \\ \rho u \\ \rho v \\ \rho e \end{array} \right\} \tag{5}$$

4

$$F = \frac{1}{J} \left\{ \begin{array}{c} \rho U \\ \rho u U + \zeta_x(p - \tau_{xx}) - \zeta_y \tau_{xy} \\ \rho v U + \zeta_y(p - \tau_{yy}) - \zeta_x \tau_{xy} \\ (\rho e + p)U + \zeta_x \beta_x + \zeta_y \beta_y \end{array} \right\} \qquad (6)$$

$$G = \frac{1}{J} \left\{ \begin{array}{c} \rho V \\ \rho u V + \eta_x(p - \tau_{xx}) - \eta_y \tau_{xy} \\ \rho v V + \eta_y(p - \tau_{yy}) - \eta_x \tau_{xy} \\ (\rho e + p)V + \eta_x \beta_x + \eta_y \beta_y \end{array} \right\} \qquad (7)$$

Where $\zeta_x = \frac{\partial \zeta}{\partial x}$, etc. The quantities u and v denote the cartesian x and y velocity components, respectively. The density ρ, static pressure p, and absolute temperature T are related through the equation of state $p = \rho RT$, where R is the gas constant. The total energy per unit mass e is defined by $e = e_i + \frac{1}{2}(u^2 + v^2)$ where the internal energy per unit mass e_i is equal to $c_v T$ with c_v denoting the specific heat at constant volume. The contravariant velocity components and Jacobian J are

$$U = \zeta_x u + \zeta_y v$$
$$V = \zeta_x u + \eta_y v \qquad (8)$$
$$J = \zeta_x \eta_y - \zeta_y \eta_x$$

The components of the cartesian stress tensor are

$$\tau_{xx} = \lambda_T \operatorname{div} \vec{v} + 2(\mu + \epsilon)\frac{\partial u}{\partial x}$$

$$\tau_{xy} = (\mu + \epsilon)\left(\frac{\partial u}{\partial y} + \frac{\partial v}{\partial x}\right) \qquad (9)$$

$$\tau_{yy} = \lambda_T \operatorname{div} \vec{v} + 2(\mu + \epsilon)\frac{\partial v}{\partial y}$$

5

where μ is the molecular dynamic viscosity, ε is the turbulent eddy viscosity, $\lambda_T = -\frac{2}{3} (\mu + \varepsilon)$ and div $\vec{v} = \frac{\partial u}{\partial x} + \frac{\partial v}{\partial y}$. The quantities β_x and β_y in (6) and (7) are

$$\beta_x = Q_x - u\tau_{xx} - v\tau_{xy}$$

$$\beta_y = Q_y - u\tau_{xy} - v\tau_{yy}$$

(10)

where Q_x and Q_y are the components of the heat flux given by

$$Q_x = - \gamma(\frac{\mu}{Pr} + \frac{\varepsilon}{Pr_t}) \frac{\partial e_i}{\partial x}$$

$$Q_y = - \gamma(\frac{\mu}{Pr} + \frac{\varepsilon}{Pr_t}) \frac{\partial e_i}{\partial y}$$

(11)

where $\gamma = c_p/c_v$ is the ratio of specific heats, and Pr and Pr_t are the molecular and turbulent Prandtl numbers, respectively, with values of 0.72 (air) and 0.90.

The above equations neglect the effects of fluctuating molecular viscosity and thermal conductivity, the joint contribution of the fluctuating velocity and fluctuating viscous stresses to the total energy dissipation, and the contribution of the kinetic energy to the total energy and mean pressure gradient, in agreement with numerous investigations.[15,16,18,20]

The turbulent eddy viscosity is given by the two-layer equilibrium eddy viscosity of Cebeci and Smith,[26-28] with the transition model of Dhawan and Narasimha.[29] In addition, the relaxation model for the turbulent eddy viscosity developed by Shang and Hankey[15,30] is incorporated. Complete details are provided in Reference 22.

The four major types of boundary conditions for the Navier-Stokes equations are illustrated in Figure 3a. On the upstream boundary (curve AD), the flow variables are held fixed at the appropriate freestream values. At the downstream boundary (curve CF), the conventional zero-gradient boundary condition is applied, i.e.,

$$\frac{\partial u}{\partial \zeta} = 0$$

(12)

On the ramp and inlet surfaces, (curves BC and EF), the tangential velocity component is set equal to zero, while the normal velocity component is determined from the specified mass flux. In addition, the walls are assumed to be adiabatic ($\frac{\partial T}{\partial n} = 0$), and the normal gradient of the pressure is set

6

equal to zero ($\frac{\partial p}{\partial n} = 0$). The latter boundary condition is an approximation to the exact expression for $\frac{\partial p}{\partial n}$ at a solid surface, and has been successfully implemented in a variety of flows exhibiting shock-boundary layer interaction.[18,31,32] Finally, the contours AB and DE ahead of the leading edges of the ramp and cowl, respectively are assumed to be no-reflection boundaries, and the following boundary conditions are employed

$$\frac{\partial u}{\partial \xi} = 0$$

$$\frac{\partial v}{\partial \xi} = 0$$

$$\frac{\partial T}{\partial \xi} = 0 \tag{13}$$

$$\frac{\partial p}{\partial \xi} = 0$$

where the derivative $\partial / \partial \xi$ is taken along the outwards running characteristic at the boundary, which is oriented at the Mach angle $\mu = \sin^{-1} (1/M)$ with respect to the velocity vector as illustrated in Figure 3b. Further details regarding the implementation of the boundary conditions are given in Reference 22.

The explicit finite-difference algorithm of MacCormack,[12,13] is employed to integrate the Navier-Stokes equations from an assumed initial condition until a steady-state flowfield is obtained. The algorithm is a alternating-direction technique of second-order accuracy, and has been employed in a wide variety of problems in high speed flows involving strong viscous-inviscid interaction.[12,13,15-18,20,30] In the present case, a variety of techniques are incorporated with MacCormack's method in order to improve the efficiency of the calculation, including time-splitting of the finite-difference operators, and automatic optimized splitting of the computation domain into five interrelated regions. In addition, a number of forms of numerical damping are incorporated in order to control possible numerical instabilities associated with shock waves, initial transients and flow separation. Details of the numberical algorithm are presented in Reference 22.

2. Computational Sublayer

A major factor governing the efficiency of an explicit finite-difference algorithm (such as Mac Cormack's method) is the requirement of resolving all pertinent scales within the ramp and cowl boundary layers. Ordinarily, the

exceedingly fine mesh spacing needed to resolve the viscous sublayer portion of the turbulent boundary layers would imply that the allowable time step for integration of equations (4) in this region is exceptionally small compared to the allowable time step, for example, in the region outside the boundary layers. Since the steady-state solution is obtained by integration of the flowfield in time from an assumed initial condition, this exceptionally large disparity in permissible time steps implies that most of the computer time is spent in integrating the governing equations over a region comprising a small fraction of the computational domain.

In order to partially alleviate this difficulty, a separate and efficient treatment of the region containing the viscous sublayer and transition portion of the turbulent boundary layer is employed. This region is taken to be $0 \leq y' \leq 60 \ \nu_w/u_*$, where y' is the distance normal to the wall, $\nu_w = \mu_w/\rho_w$, $u_* = \sqrt{\tau_w/\rho_w}$, with τ_w denoting the wall shear stress and the subscript w implying evaluation at the wall. Following previous study,[27] the governing equations are taken to be the following:

$$\dot{m} \frac{\partial u'}{\partial y'} = - \frac{\partial p}{\partial x'} + \frac{\partial \tau_{x'y'}}{\partial y'} \tag{14}$$

$$\frac{\partial}{\partial y'} [\dot{m}(c_p T + \frac{1}{2} u'^2) - c_p (\frac{\mu}{Pr} + \frac{\epsilon}{Pr_t}) \frac{\partial T}{\partial y'} - u' \tau_{x'y'}] = 0 \tag{15}$$

$$\tau_{x'y'} = (\mu + \epsilon) \frac{\partial u'}{\partial y'} \tag{16}$$

where, in this case, x' and y' are local cartesian coordinates parallel and normal to the surface, respectively; u' is the velocity component parallel to the wall, $\tau_{x'y'}$ is the shear stress parallel to the wall, and $\dot{m}$ is the normal mass flux at the surface (bleed implying negative values of $\dot{m}$). These equations are obtained from the full equations of motion under the following assumptions:

a. Negligible streamwise variation in the convection of mass, momentum and total enthalpy, i.e., $\frac{\partial \rho u'}{\partial x'} \simeq 0$, $\frac{\partial \rho u'^2}{\partial x'} \simeq 0$

and $\frac{\partial}{\partial x'} \{\rho u' [c_p T + \frac{1}{2}(u'^2 + v'^2)]\} \simeq 0$

where v' is the velocity component normal to the wall

8

b. Boundary layer approximation

c. Negligible variation in $\partial p / \partial x'$ across the viscous sublayer and transition region

d. $v'^2 \ll \dfrac{2}{(\gamma-1)} c^2$, where $c = \sqrt{\gamma R T}$ is the local speed of sound

The equations (14) to (16) are solved within the region $0 \le y' \le 60 \; \nu_w/u_*$, which is denoted as the "computational sublayer." The validity of the above assumptions has been successfully demonstrated for the cases of a flat plate turbulent boundary layer, and shock-turbulent boundary layer interaction. Details are presented in Sections III.C and III.D.

The use of the computational sublayer technique substantially improves computational efficiency by permitting the mesh spacing used by MacCormack's algorithm near the walls to be as large as approximately $60 \; \nu_w/u_*$, with the region $0 < y' \le 60 \; \nu_w/u_*$ resolved by a separate finite-difference mesh on which equations (14) to (16) are solved. Without the computational sublayer technique, the mesh spacing for MacCormack's algorithm would need to be less than approximately $5 \; \nu_w/u_*$, thereby implying a substantial increase in computer time.

Details of the implementation of the computational sublayer technique are given in Appendix A. Information regarding the impact of the method on the coordinate transformation and details regarding the solution of (14) to (16) are provided in Reference 22.

9

SECTION III

RESULTS

A. Overview

A wide variety of flows were considered in order to investigate the accuracy, efficiency and general applicability of the approach. The calculations may be basically grouped into four major areas. In the first instance, the accuracy and efficiency of the numerical algorithms were investigated for the classical case of the interaction of a shock wave and a laminar boundary layer. The effect of the mesh distribution in the inviscid region was also considered. The second area consists of a detailed investigation of the accuracy, efficiency and sensitivity of the computational sublayer model, using an adiabatic flat plate turbulent boundary layer as the test case. Thirdly, the applicability of the computational sublayer technique for strong viscous-inviscid interactions with flow separation was scrutinized by investigating a shock-turbulent boundary layer interaction on a flat plate. Finally, the numerical code was applied to the calculation of three simulated high speed inlet flows. In each area, detailed comparison was made with experimental data and previous computations. The results are indicated in the following sections.

B. Shock-Laminar Boundary Layer Interaction

The importance of shock-boundary layer interaction in high speed inlets necessitates the validation of the numerical code for a flowfield of this type. The consideration of a laminar, as opposed to a turbulent, boundary layer allows the accuracy of the numerical algorithm to be examined without the additional physical limitations of the turbulence model.

The flowfield configuration is one of the classical experimental cases of shock-laminar boundary layer interaction investigated by Hakkinen et al.[33] The flow has also been computed previously by MacCormack and Baldwin.[13] As illustrated in Figure 4, a laminar boundary layer develops on a flat plate, with freestream Mach number $M_\infty = 2.0$, freestream total temperature $T_t = 527.4°K$ and freestream total pressure $p_{t_\infty} = 6.693$ psia. An oblique shockwave at an angle of 31.3471° relative to the horizontal intersects the plate at a distance of 1.92 in. from the leading edge, and imposes an overall wall static pressure rise from p_∞ to $1.2 p_\infty$.

The major objectives of the investigation were the demonstration of the accuracy and efficiency of the numerical code, and the determination of

sensitivity of the computed solution to the mesh distribution in the freestream or inviscid region. Previous investigations[34] have demonstrated that it is desirable for the mesh diagonals (see Figure 4) to be parallel to the incident shock front, (i.e., $\Delta y = \Delta x \tan\theta$) in order to obtain a more sharply defined shock wave structure. For high speed inlets, however, this criterion cannot in general be met everywhere within the inviscid region due to the general curvilinear shape of the inlet contours and the complexity of the oblique shock wave train (see Figure 1). It was therefore decided to investigate the flowfield for two different types of distributions of mesh points. A total of six cases were considered. In each case, the streamwise mesh spacing Δx was taken to be constant, although different values were used in various cases. For the distribution of mesh points in the y direction, two different types of distributions were employed. The first type (denoted as "geometric/uniform") consisted of a geometric stretching of the mesh points in the physical plane within the region $0 \leq y \leq 9\delta$, where $\delta = 0.026$ in. is the boundary layer thickness at $x = 1.50$ in. where the skin friction begins to depart from the compressible Blasius solution, and uniform mesh spacing $\Delta y = \Delta x \tan\theta$ in the region $9\delta \leq y \leq 51\delta$. Within the geometrically stretched region, the mesh spacing was given by

$$\Delta y_j = y_j - y_{j-1} = C \, \Delta y_{j-1}, \quad j = 3,4, \ldots , JM \qquad (17)$$

where y_j is the physical location of the jth point from the wall (with $y_1 = 0$), the quantity C is the geometric stretching factor (which in general depends on j), and JM is the number of points in the geometrically stretched region. The quantities Δy_2 and C are chosen to provide sufficiently fine mesh within the boundary layer. The second type of mesh spacing (denoted as "geometric") consisted of an entirely geometric mesh spacing in the y direction according to equation (17).

The details of the mesh distribution of the six cases are indicated in Table 1. The details of the mesh system of MacCormack and Baldwin[13] are also presented, in which a geometric mesh stretching is employed for $y \leq 3.7\delta$ and a uniform mesh spacing for $3.7\delta \leq y \leq 55.1\delta$. The geometric/uniform calculations consist of Cases 1 and 2, for which the non-dimensional streamwise mesh spacing $\Delta x/\delta = 4.92$ and vertical mesh spacing at the wall $\Delta y_2/\delta = .042$ and .058 are comparable to those of MacCormack and Baldwin. For the geometric only mesh calculations of Cases 3 and 4, the streamwise mesh

11

TABLE 1.   DETAILS OF MESH FOR SHOCK-LAMINAR
BOUNDARY LAYER INTERACTION

Case	Mesh Type	Mesh Pts. in x	Mesh Pts. in y	$\Delta x/\delta$	$\Delta y_2/\delta$	C	JM	y_{JL}/δ	Points in Boundary Layer at x = 1.5 in.
1	Geometric/Uniform	32	30	4.92	.042	1.329	16	51.0	8
2	Geometric/Uniform	32	32	4.92	.058	See Note 2	32	51.0	9
3	Geometric	32	32	4.92	.117	1.148	32	51.0	7
4	Geometric	32	32	4.92	.031	1.194	32	39.0	12
5	Geometric	63	32	2.46	.058	1.164	32	39.0	9
6	Geometric (See Note 3)	63	32	1.23	.058	1.164	32	39.0	9
MacCormack and Baldwin (Ref. 13) (See Note 4)		32	32	4.62	.046	Variable	16	55.1	7

Notes: 1. $\delta = 0.026$ in. is the boundary layer thickness at x = 1.5 in.

2. For Case 2, C = 1.164 for j = 3 to j = 13, and C = 1.561 for j= 14 to j = 18.

3. Calculation started at x = 1.504 in. using results of Case 5.

4. Since Mac Cormack and Baldwin employed an image point at the boundary, the value listed for Δy_2 is the distance between the boundary and the first mesh point above the wall.

spacing $\Delta x/\delta = 4.92$ is again close to that of MacCormack and Baldwin, while the corresponding values of $\Delta y_2/\delta = .117$ and $.031$, respectively, bracket the value of $\Delta y_2/\delta = .046$ used by MacCormack and Baldwin. Finally, for the geometric only mesh calculations of Cases 5 and 6, the values of $\Delta x/\delta$ are approximately one-half and one-fourth of those employed by Baldwin and MacCormack, while the value of $\Delta y_2/\delta$ is roughly comparable.

The general computational domain is shown in Figure 4. Depending on the particular case, the upstream boundary is taken at 0.448 to 0.48 in. ahead of the leading edge, while the downstream boundary is at 3.488 to 3.52 inches downstream of the leading edge. The lower boundary coincides with the surface of the plate, while the upper boundary is taken at 1.326 in. (for Cases 1 to 3) or 1.0136 in. (for Cases 4 to 6). The boundary conditions are indicated in Section II.B.1, except that on the upper boundary the values of the flow variables were held fixed at the appropriate freestream or Rankine-Hugoniot conditions.

In Figure 5, the experimental and calculated surface pressure distributions for Cases 1 through 4 are shown. Cases 5 and 6 are omitted for clarity, as all cases are virtually identical. The results of MacCormack and Baldwin are essentially identical to those indicated, except for a somewhat closer agreement with the experimental data in the vicinity of the peak pressure at x = 2.0 in., and have also been omitted for clarity. The agreement in all cases is good. As expected from earlier studies,[35] the surface pressure is seen to be relatively insensitive to the type of mesh distribution.

In Figure 6, the calculated skin friction coefficient $c_f = \tau_w/(\frac{1}{2}\rho_\infty U_\infty^2)$ for Cases 1 and 2 (see Table 1) with geometric uniform mesh is indicated together with the experimental data and the results of MacCormack and Baldwin. The computed results for Cases 1 and 2 are nearly identical except within a narrow region surrounding the minimum in c_f. The results are in generally good agreement with the experimental data, except for a "hump" in the region $1.0 \leq x \leq 1.5$ in. where the value of c_f is approximately 15% too high. The region of the hump coincides roughly with the value of x at which the incident shock intersects the upper boundary of the geometrically stretched mesh (y = 9δ), and the discrepancy is thus believed to be due to numerical distortion of the shock wave.

In Figure 7, the calculated skin friction coefficient for the geometric mesh of Cases 3 and 4 is displayed together with the experimental data. As

13

indicated in Table 1, the mesh spacing in the x direction was fixed at the same value as in Cases 1 and 2, while the vertical mesh spacing Δy_2 for Cases 3 and 4 was respectively coarser and finer than in Cases 1 and 2. Within the region $y > 9\delta$, the ratio $\Delta y/(\Delta x \tan\theta)$ varied from 0.43 to 2.17. It is clear that the computed minimum skin friction is virtually identical for Cases 3 and 4, although substantially greater than the experimental value and the results for Cases 1 and 2. In Cases 5 and 6, the streamwise mesh spacing was taken to be one-half and one-fourth, respectively, of the value of the previous cases, and the vertical mesh spacing Δy_2 was identical to that of Case 2. The mesh spacing in y was stretched geometrically, with $\Delta y/(\Delta x \tan\theta)$ varying from 0.47 to 1.85 in the region $y > 9\delta$. For both cases, the computed skin friction was virtually identical to Case 4, except in the vicinity of the minimum c_f where the computed skin friction decreased by less than 16%.

The results of Cases 1 through 6 demonstrate that the numerical code is capable of accurate prediction of the details of shock-boundary layer interactions. They also emphasize that the computed wall shear stress in the vicinity of shock-boundary layer interaction may be somewhat altered by the use of a non-uniform mesh spacing in the inviscid region which violates the criterion $\Delta y = \Delta x \tan\theta$. In general, this criterion cannot be satisfied everywhere for general high speed inlets due to their general curvilinear shape and the complexity of the oblique shock train. The coordinate generation program (see Section II.A) provides an approximately uniform mesh spacing in y in the interior (inviscid region) of the computational domain, which is preferable to a non-uniform mesh in that region.

Typical values of the computer time required on an IBM 370/168 (using Forth Opt=1 compiler) are 0.61 hours for Case 3 and 0.87 hours for Case 1. These particular calculations were run for a total physical time of 4.7 t_c and 4.0 t_c, respectively, where t_c is the characteristic time required for a fluid particle to traverse the computational domain in the freestream region from the upstream to the downstream boundary. It should be noted that the numerical code incorporates a full geometric capability through the coordinate transformation $\zeta(x,y)$ and $\eta(x,y)$, although such flexibility is not needed for the simple geometry of Figure 4. Consequently, the computer times listed above could be reduced even further for this specific geometry. The performance of the numerical code indicated above represents a reduction in computer time by a factor of 2.4 and 4.0, respectively, compared to the time

14

required for the same configuration using an earlier high speed inlet code.[20] This improvement is basically due to the incorporation of the split-mesh technique.[22]

C. Accuracy, Efficiency and Sensitivity of Computational Sublayer Model

The purpose of this area of investigation is to determine the effects of the computational sublayer technique on the accuracy and efficiency of the numerical code, and to develop an approximate criterion for the maximum allowable thickness of the computational sublayer region (i.e., the distance y'_m discussed in Appendix A).

The flowfield configuration is a simple turbulent boundary layer on an adiabatic flat plate at a freestream Mach number $M_\infty = 2.96$, freestream total temperature $T_{t_\infty} = 437°R$, and freestream total pressure $p_{t_\infty} = 54.7$ psia. The boundary layer is assumed to transition from laminar to turbulent in the immediate vicinity of the leading edge. A total of four cases were considered. In each case, the streamwise mesh spacing Δx was taken constant and equal to 1.56δ, where $\delta = 0.13$ in. is the boundary layer thickness at $x = 0.45$ ft., which is near the downstream boundary of the computational domain. The distribution of _ordinary_ mesh points (see Appendix A) in y was a combination of stretching given by equation (17), followed by uniform spacing. For those cases incorporating the computational sublayer model, the sublayer mesh points were distributed uniformly between the wall and the first row of ordinary mesh points adjacent to the wall.

The details of the mesh distribution for the four cases are presented in Table 2. The first three cases (numbers 7 through 9) incorporated the computational sublayer model, while in the last case (number 10) the computational sublayer model was _not_ employed in order to provide a direct comparison with the effects of the sublayer model. In order to evaluate the effect of the thickness Δy_2 of the sublayer region (i.e., the distance above the wall of the first row of ordinary points, denoted as y'_m in Appendix A), calculations for Cases 7 through 9 were performed at values of Δy_2^+ equal to 27.8, 52.1, and 97.3, respectively, where $\Delta y_2^+ = \Delta y_2 u_*/\nu_w$. Since a total of ten mesh points were employed in the sublayer region in each of Cases 7 through 9, the dimensionless mesh spacing Δy_{SL}^+ of the first row of sublayer points above the wall was 3.09, 5.79 and 10.8, respectively, which is

15

TABLE 2. DETAILS OF MESH FOR STUDY OF COMPUTATIONAL
SUBLAYER MODEL

Case	Type (Note 1)	Mesh Pts. in x	Ordinary Mesh Pts. in y	Sublayer Mesh Pts. in y	$\Delta x/\delta$	Δy_2^+ (Note 3)	Δy_{SL}^+ (Note 4)	C	JM	y_{JL}/δ
7	CSL	32	32	10	1.56	27.8	3.09	1.154	21	5.92
8	CSL	32	28	10	1.56	52.1	5.79	1.198	19	5.70
9	CSL	32	30	10	1.56	97.3	10.8	1.145	20	5.58
10	No CSL	32	35	No Sublayer	1.56	3.78	–	1.200	30	5.56

Notes: 1. CSL implies computational sublayer model incorporated.

2. $\delta = 0.13$ in. is the boundary layer thickness at $x = 0.45$ ft., which is near the downstream end of the mesh.

3. Δy_2 is the distance above the wall of the first row of ordinary points (see Appendix A), and $\Delta y_2^+ = \Delta y_2 u_*/\nu_w$ where $u_* = \sqrt{\tau_w/\rho_w}$ and ν_w are evaluated at $x = 0.45$ ft.

4. Δy_{SL} is distance above the wall of the first row of sublayer points, and $\Delta y_{SL}^+ = \dfrac{\Delta y_{SL} u_*}{\nu_w}$.

16

sufficient to resolve the viscous sublayer.* In Case 10, where the computational sublayer method was not used, the dimensionless mesh spacing at the wall $\Delta y_2^+ = 3.78$ provided adequate resolution of the viscous sublayer.

In Figure 8, the computed skin friction coefficient c_f is indicated for all four cases. Except in the vicinity of the leading edge of the plate, the values are in close agreement. In particular, at x = 0.45 ft. (corresponding to $Re_x = \rho_\infty U_\infty x/\mu_\infty = 5.40 \times 10^6$), the average value of c_f for the four cases is 1.737×10^{-3}, with a maximum deviation of 2.0%. Disregarding the results of Case 9 (which had $\Delta y_{SL}^+ = 10.8$ and $\Delta y_2^+ = 97.33$), the average value of c_f at the same location is 1.725×10^{-3}, with a maximum deviation of 1.2%. The results are in close agreement with the values predicted for c_f using the Van Driest II theory coupled with the Kármán-Schoenherr equation.[36] In particular, the values of c_f for Cases 7 and 10 (which are essentially identical for x > 0.1 ft.) are within 6.9% of the Kármán-Schoenherr value at x = 0.26 ft., and within 2.7% of the Kármán-Schoenherr value at x = 0.45 ft. ($Re_\theta = 5.9 \times 10^3$ and 7.7×10^3, respectively, where $Re_\theta = \rho_\infty \theta U_\infty/\mu_\infty$ and θ is the compressible displacement thickness). These results demonstrate that, in the calculations employing the computational sublayer model, the computed values of c_f are insensitive to the value of Δy_2 for $\Delta y_2^+ < 100$, and are in close agreement with the results obtained by the less efficient procedure of resolving the viscous sublayer with the ordinary mesh.

In Figure 9, the "incompressible" thickness δ_i^*, defined by

$$\delta_i^* = \int_0^\delta (1 - u/U_\infty)dy \tag{18}$$

is presented. This quantity is employed in the turbulent eddy viscosity within the outer region of the boundary layer.[22] It is evident that, except in the vicinity of a narrow "hump" near x = 0.15 ft., the computed values of δ_i^* for Cases 7, 8 and 10 are in close agreement. The values for Case 9 (which used $\Delta y_{SL}^+ = 10.8$ and $\Delta y_2^+ = 97.3$) are significantly above the others. This discrepancy suggests that the value $\Delta y_2^+ = 97.3$ was too large.** In view of these results, the conservative criterion $\Delta y_2^+ \leq 60$ (i.e., $y_m' < 60 \, \nu_w/u_*$ was adopted. For this reason, the results of Case 9 have been omitted from the remainder of this discussion.

---

*The mesh spacing $\Delta y_{SL}^+ = 10.8$ in Case 9 is somewhat larger than that normally desired for the resolution of the viscous sublayer, which is typically $\Delta y_{SL}^+ \leq 5$ (Ref. 22).

**Possibly the use of $\Delta y_{SL}^+ = 10.8$, which is somewhat larger than that employed in the other cases, was a contributing factor. Of course, Δy_{SL}^+ can be decreased by employing more sublayer points.

Comparison of the results of Cases 7, 8 and 10 for other flow
quantities also displayed close agreement. In Figures 10a and 10b, the
computed static temperature at x = 0.4 ft. is displayed for the entire and
near wall portions of the boundary layer, respectively. The results are
in very good agreement. In Figure 11, the computed streamwise velocity
profile at x = 0.4 ft. for Cases 7 and 10 is indicated. The results of
Case 8 are in close agreement and are omitted for clarity. For a
compressible adiabatic turbulent boundary layer, the Law of the Wall[37]
is expressed as

$$\frac{U_\infty}{A} \sin^{-1} [\frac{Au}{U_\infty}] = \frac{u_*}{\kappa} \ln(\frac{yu_*}{\nu_w}) + Cu_* \tag{19}$$

where

$$A^2 = Pr_t \, M_\infty^2 (\gamma - 1) \, T_\infty / (2T_w)$$

$$\kappa = 0.40, \quad C = 5.1$$

The results indicate the well-known accuracy of the turbulence model of
Ceoeci and Smith, and demonstrate the close agreement achieved between the
two cases.

The incorporation of the computational sublayer model provides for a
substantial increase in efficiency of the numerical code. The computer
time required on an IBM 370/168 (using Fortg compiler) for Case 7, which
employed the sublayer model, was 0.30 hours, which represents a decrease
by a factor of 8.2 compared to the time required for Case 10 which did not
utilize the sublayer technique. Furthermore, the computer time required for
Case 7 represents a reduction by a factor of approximately 20 compared to
the estimated performance of the previous high speed inlet code.[20] In
each case, the total physical time for the computation was $2.2t_c$.

In conclusion, the computational sublayer technique has been shown to
provide accurate flowfield solutions at a substantial improvement in
computational efficiency. A conservative criterion

$$y_m' \leq 60 \, \nu_w / u_* \tag{20}$$

has been adopted, and the computed flowfields have been shown to be
insensitive to the particular value of y_m' employed within the above limit.

18

D. Shock-Turbulent Boundary Layer Interaction

The purpose of this phase of the research is to demonstrate the
capability of the numerical code with the computational sublayer model
to accurately compute flows displaying shock-turbulent boundary layer
interaction. The configuration chosen is the interaction of an oblique
shock wave with a turbulent boundary layer on an adiabatic flat plate. The
freestream mach number M_∞ is 2.96, and the freestream total temperature
and total pressure are 437°R and 54.7 psia, respectively. An oblique
shock wave at an angle of 25.84 degrees with respect to the horizontal
intersects the plate at a distance x_{SHK} = 1 ft. from the leading edge. The
Reynolds number based on frestream conditions and the length x_{SHK} is
1.2×10^7. This configuration has been investigated experimentally by Law[38]
and computed by Shang et al.[30*] The calculations of Shang employed
MacCormack's method, and directly resolved the viscous sublayer without
use of the computational sublayer technique.

The calculation was performed in two steps. First, the region upstream
of the shock-boundary layer interaction extending from x = - 0.06 ft. to
x = 1.0 ft. was computed using a mesh with 64 points in the x direction,
30 points in the ordinary mesh in the y direction, and 10 points in the
computational sublayer. The profiles at x = 0.873 ft. were then employed
as the upstream condition for the calculation of the shock-boundary layer
interaction (SBLI) region extending from x = 0.873 ft. to x = 1.123 ft.
This overlapping procedure is identical to that employed by Shang. The
details of the mesh distribution in the upstream region (Case 11a) and
downstream SBLI region (Case 11b) are presented in Table 3, together with
that used by Shang in the SBLI region. Note that the dimensionless
distance of the first row of sublayer points above the wall is one-ninth
of Δy_2^+, i.e., $\Delta y_{SL}^+ = \Delta y_{SL} u_*/\nu_w = 2.69$, where Δy_{SL} is the mesh spacing in
the computational sublayer and the quantities u_* and ν_w are evaluated at
x = 0.873 ft. (the restart station). The turbulent eddy viscosity
relaxation model employed by Shang was included in an identical manner in
the calculations, with a relaxation length $\lambda = 20\delta$ (see Reference 22).

---

*The author is grateful to Drs. J. Shang and W. Hankey
for providing him with their detailed results.

19

TABLE 3. DETAILS OF MESH FOR SHOCK-TURBULENT BOUNDARY LAYER INTERACTION

Case	Region	Mesh Pts. in x	Ordinary Mesh Pts. in y	Sublayer Mesh Pts. in y	$\Delta x/\delta$ (Note 1)	Δy_2^+ (Note 2)	c	JM	y_{JL}/δ
11a	Upstream of SBLI	64	30	10	1.20	24.2	1.154	19	4.36
11b	SBLI Region	64	30	10	0.28	24.2	1.154	19	4.36
Shang et al.[30] (SBLI Region)		64	30	No Sublayer Model	0.28	9.6	Variable	18	4.42

Notes: 1. δ = 0.17 in. is the boundary layer thickness at x = 0.87 ft.

2. Δy_2^+ is evaluated at x = 0.87 ft. For Cases 11a, b, it is the dimensionless distance above the wall of the first row of ordinary mesh points. For the results of Shang et al.,[30] it is the dimensionless distance of the first row of mesh points above the wall.

20

The computed results in the upstream region are in close agreement with the calculations of Shang. In particular, the computer value of c_f at $x = 0.873$ ft. is 1.569×10^{-3}, while the value of Shang at the same location is 1.527×10^{-3}. The computed streamwise velocity profiles at $x = 0.873$ ft. agree to within 3%. The computed adiabatic wall temperature at the same location is 407.1°R, which compares favorably with the theoretical value of 409.5°R obtained from the expression

$$T_w = T_\infty \left(1 + \frac{(\gamma-1)}{2} Pr_t M_\infty^2\right) \tag{21}$$

The predicted value of Shang is 376.9°R. The disagreement between this value and the theoretical value from (21) may possibly be attributed to the fact that the value $\Delta y_2^+ = 9.6$ in Shang's calculation is approximately 3.6 times the effectively mesh spacing at the wall employed in the present case (i.e., $\Delta y_{SL}^+ = 2.69$).

In Figure 12, the computed surface pressure is compared with the previous calculation of Shang and the experimental data of Law. It is evident that the two calculations are in close agreement, thereby providing additional confirmation of the accuracy of the computational sublayer method. There is some disagreement with the experimental results ahead of the peak in the surface pressure, which may be attributed to the approximate nature of the turbulence model and uncertainty in the experimental measurements.[30]

In Figure 13, the computed skin friction coefficient is displayed vs. $x - x_s$, where x_s is the separation point, together with the previous results of Shang and the experimental separation-to-reattachment length of Law. The computed separation point, obtained by linear interpolation of c_f, is $x_s = 0.983$ ft., which is in close agreement with the value $x_s = 0.985$ ft. obtained by Shang. The results are in close agreement, particularly in the extent of the separation region. The present results, however, indicate a larger peak negative skin friction and slightly greater values downstream of reattachment. These differences may be attributed to the fact that in the present case an effectively finer mesh resolution is employed near the wall.[39]

In order to evaluate the effect of the approximations employed in the sublayer model, the full boundary layer equations may be integrated across the sublayer region $0 \leq y \leq y_m$ to yield the following general expression

21

for the wall shear stress:

$$\tau_w = \frac{\left[u_m - \frac{\partial p}{\partial x} \int_0^{y'_m} \frac{y\,dy}{(\mu+\varepsilon)} - \dot{m} \int_0^{y'_m} \frac{u\,dy}{(\mu+\varepsilon)} \right]}{\int_0^{y'_m} \frac{dy}{(\mu+\varepsilon)}}$$

$$- \frac{\int_0^{y'_m} \frac{1}{(\mu+\varepsilon)} \left[(\rho v - \dot{m})u + \int_0^{y} \frac{\partial}{\partial x}(\rho u^2)\,dy \right] dy}{\int_0^{y'_m} \frac{dy}{(\mu+\varepsilon)}}$$

(22)

where u_m is the velocity at y'_m and $\dot{m}$ is the bleed mass flux which is zero
in this case. The first term is equivalent to the expression employed for
τ_w in the sublayer model, and the second term represents the correction to
the wall shear stress due to the terms neglected in the sublayer equations.
Using the computed solution, this term was evaluated, and the corrected value
of the friction coefficient is displayed in Figure 13. It is evident that
the corrections to the wall shear stress are negligible everywhere,
including the region of separated flow. A similar analysis was performed
for the wall temperature, and the maximum correction was found to be 0.63%.

The computer time required on an IBM 370/168 was 0.94 hours for
Case 11a (using Forth Opt=1 compiler) and 1.37 hours for Case 11b (using
Forrg compilier). The calculations were run for a total physical time of
1.8 t_c and 4.76 t_c, respectively, where t_c is the characteristic time for
the respective regions.

In conclusion, the numerical code with the computational sublayer model
has demonstrated the capability for accurate solution of flows with shock-
turbulent boundary layer interaction, including regions of separated flow.

E. Simulated High Speed Inlet

1. Overview

The fourth and final phase of the research is the computation of the
flowfield for a representative high speed inlet. The configuration
investigated is the simulated high speed inlet developed and tested by the
McDonnell Aircraft Company[2] (MCAIR) illustrated in Figure 14. The model
consists of a converging supersonic diffuser formed by two non-parallel
flat plates followed by a constant height "throat." The upper and lower
surfaces are analogous to the ramp and cowl of a high speed inlet. A
single oblique shock wave train is formed in the converging section of the
model, which interacts with the turbulent boundary layers on the ramp and
cowl surfaces. The long straight ramp generates boundary conditions at the
inlet entrance which are similar to the conditions experienced in a mixed
compression high speed inlet. The distance from the ramp leading edge to
the inlet entrance (i.e., cowl leading edge) is approximately 15.0 in.
depending on the cowl angle δ_c, corresponding to a Reynolds number of
6.6×10^6. Boundary layer bleed is provided on the ramp and cowl by means
of porous metal plates. The model was instrumental to provide ramp and
cowl static pressure profiles, boundary layer pitot profiles and bleed mass
flow data. A variety of flow conditions and model configurations were
tested.

A total of three different configurations were considered, corresponding
to nominal cowl angles δ_c equal to 6, 8 and 10 degrees. In each case, the
freestream Mach number M_∞ = 3.51, and the freestream stagnation temperature
and pressure are 581°R and 49.4 psia, respectively. Details of the bleed
configurations are provided in Table 4.

The computation was performed in two separate phases. First, the
region upstream of the inlet entrance was computed using two overlapping
mesh regions in the manner discussed in Reference 22. These calculations
provided the upstream profiles near the inlet entrance for use in computing
the three separate inlet configurations. In the second phase, each inlet
flowfield was computed using a succession of overlapping mesh regions. The
details of the mesh for the upstream region (Case 12), and the three inlet
configurations (Cases 13 through 16) are indicated in Table 5. The mesh
was obtained from the solution of equations (1). As indicated previously,

23

TABLE 4. BOUNDARY LAYER BLEED CONFIGURATIONS

Case	MCAIR Run No.	δ_c (degrees)	Throat Height (in.)	Ramp Bleed Zone	Region (in.)	Bleed Flow (lbm/sec)	Cowl Bleed Zone	Region (in.)	Bleed Flow (lbm/sec)
13	174	6	0.796	No	ramp bleed		1	$22 \le x \le 23$	0.012
							2	$23 \le x \le 25$	0.023
14,15	35	8	0.798	1	$16.5 \le x \le 20.5$	0.031	1	$19.5 \le x \le 23.1$	0.021
				2	$20.5 \le x \le 25$	0.074	2	$23.1 \le x \le 25$	0.030
				3	$25 \le x \le 26.5$	0.042	3	$25.75 \le x \le 26.5$	0.015
16	36	10	0.798	1	$16.5 \le x \le 20.76$	0.034	1	$19.37 \le x \le 23.13$	0.026
				2	$20.76 \le x \le 25$	0.095	2	$23.13 \le x \le 24.87$	0.037
				3	$25 \le x \le 26.5$	0.055	3	$25.75 \le x \le 26.5$	0.024

the coordinate transformation technique is not limited to the relatively
simple geometry of Figure 14, and the ability to handle arbitrary
curvilinear inlet shapes has been demonstrated.[20] For one particular case
($\delta_c = 8°$), the flowfield was computed twice (for reasons discussed below)
using different streamwise mesh spacing.

As indicated in Table 5, sufficient resolution of the viscous sublayer
was provided by the computational sublayer mesh. The criterion[22]

$$\Delta y_{SL}^+ \leq 5$$

(where $\Delta y_{SL}^+ = \Delta y_{SL} u_* N/\nu_w$ and N is a modification due to the presence of
boundary layer bleed) is met everywhere on the ramp and cowl boundary
layers for each case. The criterion (20) on the height of the sublayer
region on the ramp and cowl is generally met at all positions. As the data
in Table 5 indicate, the maximum value of y_m' exceeded 60 ν_w/u_* at some
locations for certain cases. However, at nearly all locations the criterion
(20) was satisfied, and based on the rather conservative nature of the
estimate employed in (20), the calculations can all be deemed acceptable.

The streamwise mesh spacing Δx is required to be sufficiently fine in
order to resolve the boundary layer development, particularly within regions
of shock-boundary layer interaction, and to provide an accurate definition
of the computed shock structure. A generally accepted criterion for the
first requirement is that the ratio of streamwise mesh spacing Δx to the
boundary layer thickness δ immediately upstream of any shock-boundary layer
interaction should be less than 0.5, particularly for flows with
separation.[39] This criterion, however, provides only a rough estimate and
the actual mesh spacing required depends on the particular problem
considered. Typical values of $\Delta x/\delta$ for shock-turbulent boundary layer
interactions are 0.28 in Reference 30, 0.45 in Reference 15, and 1.0 in
Reference 40. The values of $\Delta x/\delta$ for all shock-boundary layer interactions
in the present case are given in Table 6. The values of $\Delta x/\delta$ are generally
between 0.5 and 2.0. In all of the calculations, flow separation was not
experienced due to the presence of substantial boundary layer bleed, and
therefore the criterion $\Delta x/\delta < 0.5$ was expected to be possibly too stringent.
In order to evaluate the effects of $\Delta x/\delta$ on the computed solution, the
$\delta_c = 8°$ configuration was computed twice using both a "coarse" and "fine"
streamwise mesh spacing. In the former instance (Case 14), the ratio $\Delta x/\delta$

TABLE 5. DETAILS OF MESH FOR MCAIR SIMULATED
HIGH SPEED INLET

Case	Definition	Extent (in.)	Δx (in.)	IL	JL	JSLØ	JSL1	Max Δy_{SL}^+ (Note 1)	Max $y_m'^+$ (Note 2)
12	Upstream	$-0.88 \le x \le 10.87$	0.25	48	30	10	–	2.2	19.8
		$8.63 \le x \le 20.38$	0.25	48	30	10	–	1.8	16.0
13	$\delta_c = 6°$	$13.875 \le x \le 23.625$	0.25	40	48	10	15	3.5	72.7
		$21.375 \le x \le 31.125$	0.25	40	48	10	15	5.7	78.9
14	$\delta_c = 8°$	$13.875 \le x \le 23.625$	0.25	40	48	20	20	1.7	42.1
		$21.375 \le x \le 31.125$	0.25	40	48	20	20	2.1	76.7
15	$\delta_c = 8°$	$13.9375 \le x \le 18.8125$	0.125	40	48	20	20	1.7	32.9
		$17.8125 \le x \le 22.6875$	0.125	40	48	20	20	1.7	42.3
		$21.6875 \le x \le 26.5625$	0.125	40	48	20	20	2.3	82.3
		$24.3125 \le x \le 29.1875$	0.125	40	48	20	20	2.2	80.3
16	$\delta_c = 10°$	$13.875 \le x \le 23.625$	0.25	40	48	20	20	1.9	44.1
		$21.625 \le x \le 26.500$	0.125	40	48	20	20	1.2	42.9
		$25.875 \le x \le 30.750$	0.125	40	48	20	20	1.1	39.2

Legend: δ_c = cowl angle
IL = number of mesh points in ζ direction
JL = number of mesh points in η direction
JSLØ = number of mesh points in computational sublayer on η = 0
JSL1 = number of mesh points in computational sublayer on η = 1

Note: 1. For this table, $\Delta y_{SL}^+ = \Delta y_{SL} u_* N / \nu_w$, where N is defined in Ref. 22. The maximum is taken in general over all points on the ramp and cowl.

2. For this table, $y_m'^+ = y_m' u_* / \nu_w$. The maximum is taken in general over all points on the ramp and cowl.

26

TABLE 6.   DETAILS OF STREAMWISE MESH
SPACING FOR MCAIR SIMULATED
HIGH SPEED INLET

Case	δ_c (Degrees)	Ramp SBLI No.*	$\Delta x/\delta$	Ramp SBLI No.*	$\Delta x/\delta$
13	6	1	0.83	1	1.7
		2	0.89	2	2.0
		3	1.16		
14	8	1	0.96	1	2.1
		2	1.8	2	3.1
		3	1.9		
15	8	1	0.48	1	1.0
		2	0.89	2	1.6
		3	0.96		
16	10	1	0.86	1	0.96
		2	0.89	2	1.0
		3	0.96		

*Shock-boundary layer interaction number, identified as shock
impingement No. 1, etc., on Figures 16,17, 25, 26, 34 and 35.

27

on the ramp is between approximately 1.0 and 2.0, while for the fine mesh (Case 15), the ratio is between approximately 0.5 and 1.0. The results are discussed in the following section.

The location and extent of the region of transition from laminar to turbulent flow was estimated using the method of Deem and Murphy,[41] and the generally accepted criterion that the Reynolds number (based on distance from the leading edge) approximately doubles across the transition region.[29] The turbulent eddy viscosity relaxation model of Shang and Hankey was employed only in Case 13, and was limited to the first shock-boundary layer interaction on the ramp.* This choice was motivated by the fact that there was no boundary bleed present at the first SBLI on the ramp in Case 13. For all other shock-boundary layer interactions in the cases considered, boundary layer bleed was provided in the vicinity of the SBLI and the boundary layers did not show any strong tendency towards separation. The fourth order pressure damping of MacCormack[22] was utilized with a damping coefficient $\alpha = -5.0$ as suggested by previous investigations.[20]

The experimental data obtained by the MCAIR study consists of ramp and cowl static pressure measurements, and boundary layer pitot profiles taken at various streamwise locations within the inlet. The static pressure taps were all located on the duct centerline, with the exception of two additional off-centerline taps each at x = 17, 22.75 and 26 in. on the ramp. There were two pitot rakes each at five stations on the ramp, positioned off the duct centerline. The general location of these rakes is indicated by the symbols [1] through [5] in Figure 15. As illustrated, the rakes were generally positioned upstream and downstream of the shock-boundary layer interactions on the ramp. The rake pairs at stations [1] through [3] were attached to the movable bleed plenum separators, while all remaining rakes were fixed in the duct. There were single fixed rakes located off-centerline at stations [6] and [7] .

---

*The values employed for λ and s_o are 0.208 ft. and 1.469 ft., respectively. The value of λ corresponds to $10 \, \delta_o$, where is the boundary layer thickness at x = 1.469 ft. See Ref. 22 for details of the relaxation model.

2. Results for $\delta_c = 6°$

The duct height for the $\delta_c = 6°$ configuration varies from 1.839 in. at the inlet entrance (x = 14.98 in.) to 0.796 in. at the inlet throat (x > 25.0 in.). Boundary layer bleed was provided on the cowl only as indicated in Table 4, with a total bleed flow (excluding sidewall bleed) of 1.5% of the inlet mass flow.

The computed ramp surface pressure is displayed in Figure 16, together with the experimental data. The intersection of the oblique shock wave train with the ramp at x = 20, 25 and 28 in. is indicated by the sharp pressure rise in the vicinity of these locations. The agreement is very good in the region upstream of the second shock impingement point (SIP). Downstream of the second shock, the computed static pressure shows strong qualitative agreement with the measured profiles, although the peak pressures at x   25.7 in. and x = 28.8 in. are below the experimental values. The source of this discrepancy is not clear, although two possible explanations may be offered. First, the streamwise mesh spacing Δx may not be sufficiently fine to resolve the shock-boundary layer interaction at the second and third SIP on the ramp. As indicated in Table 6, the values of $\Delta x/\delta$ are 0.89 and 1.16 at these points, respectively. However, results for Case 15 ($\delta_c = 8°$) using similar values for $\Delta x/\delta$ are in close agreement with the experimental results (see next section), which suggests that the mesh spacing Δx is adequate. Secondly, the discrepancy may be attributed to three-dimensional effects within the experimental flowfield in the vicinity of the second and third SIP. In particular, the static pressure measured by the three spanwise pressure taps at x = 26 in. varied between 2.56 and 4.70 psia.

In Figure 17, the computed and experimental cowl static pressure is shown. The agreement upstream of the second shock impingement point is very good. The computed pressure, however, does not display the double shock structure evident in the experimental data between x = 26 in. and 27.5 in. The disagreement may possibly be due to three-dimensional effects in the vicinity of the second shock impingement point; however, this conjecture is not verifiable as there were no off-centerline static pressure measurements taken on the cowl. The computed pressure downstream of the second shock impingement point is in good agreement with measured values.

29

The development of the boundary layer on the ramp is indicated in Figures 18 through 22, which display computed and measured pitot profiles at five stations. In each figure, the data from the two pitot rakes located at each station is plotted with the pitot pressure p_p non-dimensionalized by the freestream total pressure p_{t_∞}. In Figure 18, the ramp pitot profile is shown at x = 18.7 in. (station 1 on Figure 15) which is upstream of the first shock impingement point on the ramp. The computed and measured values are in close agreement.

In Figure 19, the ramp pitot profile is displayed at x = 21.3 in. (station 2 on Figure 15) which is immediately downstream of the first shock impingement point on the ramp. The computed values are in general agreement with the measured profiles.

The pitot profile at x = 23.75 in. (station 3 on Figure 15) is indicated in Figure 20. This location is immediately upstream of the second shock impingement point on the ramp. The computed results are in very close agreement with the experimental data.

In Figure 21, the pitot profile is shown at x = 25.75 in. (station 4 on Figure 15) which is immediately downstream of the second shock impingement point on the ramp. Although the computed values display general agreement with the data, the computed pitot pressure is roughly 20% higher in the outer portion of the boundary layer (0.1 in. < y < 0.2 in.). This discrepancy may possibly be attributed to the existence of significant three-dimensional effects in the vicinity of the second and third ramp shock impingement points as discussed earlier.

In Figure 22, the pitot profile is displayed at x = 27.5 in. (station 5 on Figure 15) which is immediately upstream of the third ramp shock impingement point. The computed profiles are in good agreement with the data.

The cowl boundary layer development is indicated in Figures 23 and 24, which show the computed and measured pitot pressure at two stations.* In Figure 23, the pitot pressure is shown at x = 25.75 in. (station 6 on Figure 15) which is in the vicinity of the second cowl shock impingement point. There is a marked disagreement in the region 0.1 in. < y < 0.2 in. where the experimental results suggest the presence of a reflected shock

---

*The distance y is measured from the cowl surface.

30

wave emanating from a point on the cowl upstream of x = 25.75 in. As
discussed earlier, the computed cowl pressure does not display the double
shock structure apparent in the experimental cowl pressure between x = 26 in.
and x = 27.5 in. The computed cowl pressure displays instead a shock wave
intersecting the cowl at approximately x = 27 in., downstream of station ⑥ .
The disagreement in the pitot pressure in Figure 23, therefore, is an
indication of the difference between the computed and experimental shock wave
pattern in the region between x = 26 in. and x = 27.5 in. As indicated
earlier, this disagreement may be due to three-dimensional effects in the
experimental flowfield.

In Figure 24, the pitot profile is shown at x = 27.5 in. (station ⑦
on Figure 15). The agreement is generally good, except in a region immedi-
ately outside the boundary layer between y = 0.1 in. and y = 0.3 in. where
the computed values are between 10% and 20% below the experimental values.
As indicated above, this station is in the region in which there is a
difference between the computed and experimental shock wave pattern in the
vicinity of the cowl.

The calculations for Case 13 were performed twice, using both an
IBM 370/168 and a CYBER 175 computer. The calculations on the IBM 370/168
employed single-precision arithmetic with a word length of 32 bits, while
the CYBER 175 uses a word length of 60 bits. The computed results were
essentially identical. For example, the maximum difference in the ramp or
cowl pressure distributions between the two cases is 1 %. This result
implies that the numerical algorithm is capable of taking advantage of the
improved efficiency afforded by the 32-bit arithmetic capability of such
machines as the vector-processing CDC STAR 100. Earlier calculations on the
CDC STAR using MacCormack's method with both 32-bit and 64-bit arithmetic
obtained similar conclusions.[42]

The computer time required for Case 13 on the CYBER 175 computer (using
FTN Opt=1 compiler) was 1.63 hours, which represents an estimated decrease
in computer time by a factor of 9 compared to the performance of the previous
high speed inlet code.[20] The total physical time for each of the two
regions (see Table 5) was approximately 2.7 t_c, where t_c is the character-
istic time for the particular region.

31

3. Results for $\delta_c = 8°$

The duct height for the $\delta_c = 8°$ configuration varies from 2.192 in. at the inlet entrance (x = 14.99 in.) to 0.798 in. at the inlet throat (x > 25.0 in.). Boundary layer bleed was provided on both the ramp and cowl surfaces as indicated in Table 4, with a total bleed flow (excluding sidewall bleed) of 6.8% of the inlet mass flow. As discussed previously, the $\delta_c = 8°$ configuration was computed twice using both a "coarse" mesh (Case 14) with values $\Delta x/\delta$ on the ramp ranging from 1.0 to 2.0, and a "fine" mesh (Case 15) with corresponding values $\Delta x/\delta$ between 0.5 and 1.0 .

The computed ramp static pressures for Cases 14 and 15 are indicated in Figure 25, together with the experimental data. In the vicinity of the first shock impingement point (SIP), the computed pressures are identical. The pitot profiles (discussed later) are also essentially the same for the two cases in this vicinity. As indicated in Table 6, the values of $\Delta x/\delta$ for Cases 14 and 15 are 1.0 and 0.5, respectively, thus indicating that a mesh spacing with $\Delta x/\delta < 1.0$ is sufficiently fine to resolve the flow in this region. The experimental ramp pressures downstream of the first SIP are somewhat higher than the computed results, and display two slight "humps" at approximately x = 21.5 and 24 in. The cause of this discrepancy is not clear, although a similar though less pronounced hump is apparent in Case 13 downstream of the first SIP (see Figure 16). The computed pressure in the vicinity of the second SIP for Case 15 is in close agreement with experimental values, while the results of Case 14 underpredict the peak pressure by 15%. The values of $\Delta x/\delta$ at this point for Cases 14 and 15 are 1.8 and 0.9, respectively, confirming the earlier observation that an accurate pressure profile is obtained in this region for $\Delta x/\delta$ less than one (see Table 6). Finally, the computed peak pressures at the third SIP for Cases 14 and 15 are 24% and 16%, respectively, below the maximum experimental values. The value of $\Delta x/\delta$ for Case 15 at the third SIP is 0.96, suggesting that the requirement $\Delta x/\delta < 1$ needs to be reduced further in this region. The computed pressure rise is also shifted approximately 0.5 in. downstream. This small displacement of the shock structure, observable to a much smaller degree at the second SIP, is due to the shock-capturing character of the numerical algorithm.

32

The computed cowl pressures for Cases 14 and 15 are displayed in Figure 26, together with the experimental results. Between x = 18.5 in. and 22 in., the observed pressures are 10% to 25% lower than the computed values. However, within the portion of this region that is coincident with cowl bleed zone 1 (i.e., x = 19.5 to 22 in. as shown in Table 4), the experimental data indicate that the cowl surface pressure is slightly less than the pressure within the bleed plenum underneath the surface, suggesting the possibility of negative bleed flow (i.e., surface blowing), which may account for the discrepancy in cowl pressure. The computed results for the first SIP are in excellent agreement with the data, with the maximum pressure predicted within 4%. At the second SIP, the computed peak pressures for Cases 14 and 15 are 23% and 11%, respectively, below the experimental values. The values of $\Delta x/\delta$ are 1.9 and 0.96, respectively, at the second cowl SIP.

The above results indicate that for the present case, the requirement $\Delta x/\delta < 1$ is sufficient for accurate prediction of the peak ramp and cowl pressures associated with the first three reflections of the incident cowl shock. For further reflections (i.e., the second SIP on cowl and third SIP on ramp), a mesh spacing of $\Delta x/\delta \approx 1$ yields peak pressures that are 11% to 16% low, implying that the requirement on $\Delta x/\delta$ needs to be reduced further in these regions. The results also indicate that the effect of the shock-capturing nature of the numerical algorithm is to cause a slight downstream displacement of the shock structure after a number of reflections. It should be emphasized that the above conclusions regarding the criteria for $\Delta x/\delta$ are based on a nonseparated flowfield, and that in the event of separation the more stringent criterion $\Delta x/\delta < 0.5$ is generally required for all shock-boundary layer interactions.

The computed and measured pitot profiles at the five stations on the ramp are indicated in Figures 27 through 31. In each case, the pitot pressure p_p nondimensionalized by the freestream total pressure p_{t_∞} is plotted versus the distance from the ramp surface. The locations of the five stations are shown schematically in Figure 15. In Figures 27a,b the pitot pressure is shown for Cases 14 and 15, respectively, at x = 19.2 in. (station 1 in Figure 15), which is upstream of the first SIP on the ramp.

The agreement with the experimental data is excellent, indicating the proper conditions for the ramp boundary layer at the inlet entrance have been achieved.

In Figures 28a,b the pitot pressure is shown at x = 21.8 in. (station 2), which is downstream of the first SIP on the ramp. The results for Cases 14 and 15 are essentially identical, and in reasonable agreement with experimental data.

The ramp pitot pressure profile at x = 24 in. (station 3), which is upstream of the second SIP, is displayed in Figures 29a,b. The results for Cases 14 and 15 are nearly identical, and in reasonable agreement with experimental results.

In Figures 30a,b the pitot pressure is shown at x = 25.75 in. (station 4), which is located downstream of the second SIP. The computed profiles are in reasonable agreement, with the peak values of p_p differing by 5%. There is, however, a notable disagreement with the experimental profile for y less than 0.25 in. It is evident from Figure 25 that there is substantial spanwise variation in the ramp static pressure at x = 26 in., with values ranging from 3.34 psia and 3.97 psia at the off-centerline taps to 6.24 psia on the centerline. Because of possible slight spanwise variations in the duct throat height,[43] the differences in ramp static pressure at x = 26 in. may be due to a spanwise curvature in the shock wave striking the ramp. This interpretation implies, from Figure 25, that the shock is curved slightly upstream. Since the pitot rakes at station 4 are located off-centerline, the above supposition implies that the data should be compared with computed values at a point slightly downstream of x = 25.75 in. Based on the observed off-centerline static pressure measurements at x = 26 in. and the computed ramp pressure, the pitot pressure at x = 26.3 in. is also plotted in Figure 30b, and is seen to be in better agreement with the experimental data.

The pitot pressure at station 5 , located upstream of the third SIP, is indicated in Figures 31a,b. The results of Cases 14 and 15 are in close agreement, with the latter indicating a more sharply defined incoming shock at approximately y = 0.4 in. The experimental profiles display the incoming shock at somewhat lower elevation (y = 0.25 in.), indicating that the computed shock structure is displaced slightly downstream as indicated earlier.

In Figures 32a,b the cowl pitot pressure at x = 25.75 in. (station $\boxed{6}$) is shown. The computed profiles agree within 6% within the boundary layer, and the results of Case 15 are within 7% of the experimental data. The final cowl pitot profiles at x = 27.5 in. (station $\boxed{7}$) are displayed in Figures 33a,b. The computed profiles agree within 6%, and the results of Case 15 are within 12% of the experimental values.

The computer time required on the CYBER 175 computer (using FTN Opt =1 compiler) was 2.37 hours for Case 14 and 1.93 hours for Case 15. The total physical time for each region was approximately 2.7 t_c, where t_c is the characteristic time for the particular region. It is interesting to note that the time required for Case 15 (with $\Delta x = 0.125$ in.) is less than for Case 14 (with $\Delta x = 0.25$ in.). This fortunate occurrence arises from the manner in which the structure of the flowfield affects the allowable time step (and hence code efficiency) within each region.

4. **Results for $\delta_c = 10°$**

The duct height for the $\delta_c = 10°$ configuration varies from 2.547 in. at the inlet entrance (x = 15.02 in.) to 0.797 in. at the inlet throat (x > 25.0 in.). As indicated in Table 4, boundary layer bleed was provided on both the ramp and cowl, with a total bleed flow (excluding sidewall bleed) of 7.4% of the inlet mass flow.

The computed ramp static pressure is displayed in Figure 34, together with the experimental data. As indicated in Table 6, the value of $\Delta x/\delta$ is less than one for all shock-boundary layer interactions on the ramp. Downstream of the first SIP, the computed pressure is typically 14% below the experimental centerline pressure data. The experimental results indicate the existence of three-dimensionality in this region, however, with a 29% total spanwise variation in pressure at x = 22.75 in. The computed results in the vicinity of the second SIP are in close agreement with experimental data, although the peak pressure is approximately 18% too low. Judging from the exceptionally abrupt pressure rise, it is possible that this discrepancy could be eliminated by use of a finer streamwise mesh spacing near the second SIP, indicating that the criterion $\Delta x/\delta < 1$ needs to be reduced further in this region. The computed pressure profile at the third SIP is displaced slightly downstream of the experimental data in a

manner similar to that observed for Cases 14 and 15. The peak pressure is within 5% of the data.

The computed cowl pressure is indicated in Figure 35, along with the experimental results. Between x = 19.5 in. and 22.5 in., the computed pressure is between 24% and 36% above the measured values. However, within this region the experimental data indicate that the cowl surface pressure is slightly less than the pressure within the bleed plenum underneath the surface, suggesting as in the $\delta_c = 8°$ configuration the possibility of negative bleed flow, which may account for the discrepancy in cowl pressure. At the first SIP, the computed pressure is in close agreement with the experimental results. The comparison at the second SIP is also reasonable, with the peak pressure within 12%. The computed profile also displays the slight characteristic downstream displacement seen previously.

The computed and measured pitot profiles at the five stations on the ramp are indicated in Figures 36 through 40. In Figure 36, the profiles are indicated at x = 19.46 in. (station [1]), and display excellent agreement with the data.

In Figure 37, the pitot pressure is shown at x = 22.06 in. (station [2]), which is downstream of the first SIP on the ramp. The agreement between the computed and measured profiles is good. In Figure 38, results are presented at x = 24 in. (station [3]), which is upstream of the second SIP on the ramp. The computed results display a somewhat fuller profile within the boundary layer.

In Figure 39, results are presented at x = 25.75 in. (station [4]), which is immediately downstream of the second SIP on the ramp. There is a substantial discrepancy between the computed and measured profiles for y less than 0.25 in. The ramp static pressure measurements at x = 26 in. display a substantial spanwise variation, with values ranging from 4.49 and 4.1 psia at the off-centerline taps to 6.9 psia on the centerline of the duct. As indicated in the discussion of the $\delta_c = 8°$ configuration, the observed differences in p_p may be partially attributed to a spanwise variation in the incident shock impingement location.

The final ramp pitot profile at x = 27.5 in. (station [5]) is shown in Figure 40. The computed profiles are seen to be in excellent agreement with the experimental results.

36

In Figure 41, the cowl pitot profile at x = 25.75 in. (station $\boxed{6}$) is shown. Within the boundary layer (y < 0.15 in.), the computed profile is in close agreement with the experimental results, with a maximum discrepancy of 4%. Outside the boundary layer, the computed profile indicates an incoming shock at approximately 0.5 in. from the cowl, which is farther away than the actual shock at approximately y = 0.22 in. This discrepancy is another indication of the characteristic downstream displacement of the second SIP on the cowl, as seen in Figure 35.

The final cowl pitot profile at x = 27.5 in. (station $\boxed{7}$) is displayed in Figure 42. The agreement between the computed and measured results is very good.

The computer time required on the CYBER 175 computer (using FTN Opt=1 compiler) was 4.02 hours. The total physical time for each region was approximately 2.9 t_c, where t_c is the characteristic time for the particular region. As expected, the computer time required increases with cowl angle δ_c, due to the higher surface pressures and consequently thinner boundary layers.

5. Accuracy of Computational Sublayer Model

In order to evaluate the effect of the approximations employed in the computational model, the expression (22) for the wall shear stress obtained from the full boundary layer equations may be employed to estimate the correction to the wall shear stress. In all cases, the corrections were found to be negligible. For example, the average percent correction to τ_w for the δ_c = 8° configuration was found to be 1.0% for Case 14 and 1.2% for Case 15, while for the δ_c = 10° configuration (Case 16), the average percent correction was 0.7%. In determining the average percentage correction, those pairs of mesh points between which the bleed mass flux m changes discontinuously (due to the separation of the ramp and cowl bleed into separate zones) have in general been omitted. Naturally, at these points the assumption of negligible streamwise variation in the mass, momentum and enthalpy fluxes [assumption a) in Section II.B.2] is invalid. However, these points account for a very small number of mesh points on the boundary (less than 4.6% of the boundary points in all cases), and the effect therefore on the flowfield is small.

37

SECTION IV

CONCLUSIONS AND RECOMMENDATIONS

A. Conclusions

A set of user-oriented computer programs have been developed which
provide accurate and efficient computation of the flowfields of two-
dimensional mixed-compression high speed inlets. The full Navier-Stokes
equations are employed, with turbulence represented by an algebraic turbulent
eddy viscosity together with a relaxation correction for regions of strong
viscous-inviscid interaction. A curvilinear body-oriented coordinate
system is utilized to permit the handling of arbitrary inlet contours.
Provision is included for the general specification of boundary layer bleed
on the ramp and cowl surfaces.

The numerical algorithm of MacCormack is employed to solve the Navier-
Stokes equations. A number of techniques are utilized to improve
computational efficiency, including time-splitting of the finite-difference
operators, automatic mesh-splitting, and a separate algorithm for the
treatment of the viscous sublayer portion of the turbulent boundary layers.

The numerical codes have been successfully applied to the calculation
of a variety of flows, including the interaction of an oblique snock wave
with the boundary layer on a flat plate (including separated and unseparated
flows), and three different simulated high speed inlet configurations. In
all cases, overall good agreement was obtained with the experimental data.

A substantial improvement in computational efficiency has been achieved
compared to an earlier high speed inlet code.[20] In particular, calculations
for a Mach 3.5 simulated high speed inlet at a Reynolds number of 13 million
(based on inlet length) required two to four hours of computer time on a
CYBER 175. This represents a decrease in computer time of approximately an
order of magnitude compared to the earlier work.[20]

B. Recommendations

On the basis of the present study, a number of recommendations may be
made. With regards to further experimental investigations using the MCAIR
simulated high speed inlet configuration, it is recommended that additional
instrumentation be incorporated for extensive off-centerline measurements of
the ramp and cowl static pressure at a large number of streamwise locations
in order to determine the extent of three-dimensionality in the flowfield.
As indicated previously, the ramp static pressure measurements downstream of

the second shock impingement point exhibit significant spanwise variation. It is further recommended that additional pitot pressure rakes be included on the ramp and cowl at the seven stations employed in order to provide additional information on the three-dimensional character of the ramp and cowl boundary layers. In addition, flow visualization results consisting of surface oil-flow patterns and schlieren photographs would be helpful.

In regards to future analytical research, the success of the current study strongly suggests that a full three-dimensional analytical high speed inlet capability be developed. The recent advent of high speed vector-processing computers such as the CDC STAR and CRAY I has lead to a dramatic decrease in computer time required for a given flowfield calculation. The results of recent cooperative research between the Air Force Flight Dynamics Laboratory and the NASA Langley Research Center involving a three-dimensional high speed corner flow calculation on the CDC-STAR have shown a decrease in computer time by a factor of more than 100 compared to the performance on the older-generation CYBER 74 computer.[42*] Earlier work at NASA Langley on an unsteady two-dimensional shock-boundary layer flow showed similarily impressive results.[44] These results suggest that accurate and efficient numerical simulation of three-dimensional high speed inlet flows is feasible.

_____

*The CYBER 175 computer is approximately twice as fast as the CYBER 74.

REFERENCES

1. Antonatos, P., Surber, L., and Stava, D. J., "Inlet/Airplane Interference and Integration," in Airfarme/Engine Integration, AGARD LS-53, May 1972.

2. Carter, T. D., and Spong, E. D., "High Speed Inlet Investigation. Vol. 1: Description of Program and Results. Vol. II: Data Summary," AFFDL-TR-77-105, November 1977.

3. Sorensen, V. L., "Computer Program for Calculating Flow Fields in Supersonic Inlets," NASA TND-2897, 1965.

4. Vadyak, J., and Hoffman, J. D., "Calculation of the Three-Dimensional Flow Field in Supersonic Inlete at Angle of Attack Using a Bicharacteristic Method with Discrete Shock Fitting," AIAA Paper 79-0379, January 1979.

5. Presley, L. L., "A Comparison of a Shock-Capturing Technique with Experimental Data for Three-Dimensional Internal Flows," in Aerodynamic Analysis Requiring Advanced Computers, NASA SP-347, 1975, pp. 623-642.

6. Sorensen, N. E., Smeltzer, D. B., and Latham, E. A., "Advanced Supersonic Inlet Technology," J. Aircraft, 10, 1973, pp. 278-282.

7. Reyhner, T. A., and Hickcox, T. E., "Combined Viscous-Inviscid Analysis of Supersonic Inlet Flowfields," J. Aircraft, 9, 1972, pp. 589-595.

8. Sorensen, N. E., and Smeltzer, D. B, "Performance Estimates for a Supersonic Axi-symmetric Inlet System," J. Aircraft, 9, 1972, pp. 703-706.

9. Syberg, J., and Koncsek, J. L., "Experimental Evaluation of an Analytically Derived Bleed System for a Supersonic Inlet," J. Aircraft, 13, 1976, pp. 792-797.

10. Gnos, A. V., Watson, E. C., Seebaugh, W. R., Sanator, R. J. and De Carlo, J. P., "Investigation of Flow Fields within Large-Scale Hypersonic Inlet Models," NASA TN D-7150, 1973.

11. Surber, L., and Sedlock, D., "Effects of Airframe-Inlet Integration on Half-Axisymmetric and Two-Dimensional Supersonic Inlet Performance," AIAA Paper 78-960, July 1978.

12. MacCormack, R. W., "Numerical Solution of the Interaction of a Shock Wave with a Laminar Boundary Layer," Lecture Notes in Physics, 8, 1971, pp. 151-163.

13. MacCormack, R. W., and Baldwin, B. W., "A Numerical Method for Solving the Navier-Stokes Equations with Application to Shock Boundary Layer Interactions," AIAA Paper 75-1, AIAA 13th Aerospace Sciences Meeting, 1975.

14. Carter, J. E., "Numerical Solutions of the Navier-Stokes Equations for the Supersonic Laminar Flow over a Two-Dimensional Compression Corner," NASA TR R.385, July 1972.

15. Shang, J. S., and Hankey, W. L., Jr., "Numerical Solution for Supersonic Turbulent Flow over a Compression Ramp," AIAA J., 13, 1975, pp. 1368-1374.

16. Hung, C. M., and MacCormack, R. W., "Numerical Solutions of Supersonic and Hypersonic Laminar Compression Corner Flows," AIAA J., 14, 1976, pp. 475-481.

17. Shang, J. S., and Hankey, W. L., "Numerical Solution of the Navier-Stokes Equations for a Three-Dimensional Corner," AIAA J., 15, 1977 pp. 1575-5182.

18. Deiwert, G. S., "Numerical Simulation of High Reynolds Number Transonic Flows," AIAA J., 13, 1975, pp. 1354-1359.

19. Steger, J. L., and Bailey, H. L., "Calculation of Transonic Aileron Buzz," AIAA Paper 79-0134, AIAA 17th Aerospace Sciences Mtg., Jan. 1979.

20. Knight, D. D., "Numerical Simulation of Realistic High Speed Inlets Using the Navier-Stokes Equations," AIAA J., 15, 1977, pp. 1583-1589.

21. Thompson, J. R., Thames, F. C., and Mastin, C. W., "Automatic Numerical Generation of Body-Fitted Coordinate System for Field Containing Any Number of Arbitrary Two-Dimensional Bodies," J. Comp. Physics, 15, 1974, pp. 299-319.

22. Knight, D. D., "Calculation of High Speed Inlet Flows Using the Navier-Stokes Equations. Volume II: User's and Programmer's Guide," AFFDL TR-79-3138.

23. Rubesin, M. W., and Rose, W. C., "The Turbulent Mean-Flow, Reynolds-Stress, and Heat-Flux Equations in Mass-Averaged Dependent Variables," NASA TMX-62,248, March 1973.

24. Lapidus, A., "A Detached Shock Calculation by Second-Order Finite Difference," J. Comp. Physics, 2, 1967, pp. 154-177.

25. Steger, J. L., "Implicit Finite-Difference Simulation of Flow about Arbitrary Two-Dimensional Geometries," AIAA J., 16, 1978, pp. 679-686.

26. Cebeci, T., Smith, A. M. O., and Mosinskis, G., "Calculations of Compressible Adiabatic Turbulent Boundary Layers," AIAA J., 8, 1970, pp. 1974-1982.

27. Cebeci, T., "Calculations of Compressible Turbulent Boundary Layers with Heat and Mass Transfer," AIAA J., 9, 1971, pp. 1091-1097.

28. Cebeci, T., and Smith, A. M. O., Analysis of Turbulent Boundary Layers, Academic Press, 1974.

29. Harris, J. E., "Numerical Solution of the Equations for Compressible Laminar, Transitional and Turbulent Boundary Layers and Comparison with Experimental Data," NASA TR T-368, 1971.

30. Shang, J. S., Hankey, W. L., Jr., and Law, C. H., "Numerical Simulation of Shock Wave-Turbulent Boundary Layer Interaction," AIAA J., 14, 1976, pp. 1451-1457.

31. Kutler, P., Chakravarthy, S. R., and Lombard, C. P., "Supersonic Flow over Ablated Nosetips Using an Unsteady Implicit Numerical Procedure," AIAA Paper 78-213, AIAA 16th Aerospace Sciences Meeting, 1978.

32. Rakich, J. V., Vigneron, Y. C., and Tannehill, J. C., "Navier-Stokes Calculations for Laminar and Turbulent Hypersonic Flow over Indented Nosetips," AIAA Paper 78-260, AIAA 16th Aerospace Sciences Meeting, 1978.

33. Hakkinen, R. J., Greber, I., Trilling, L., and Abarbanel, S. S., "The Interaction of an Oblique Shock Wave with a Laminar Boundary Layer," NASA Memo 2-18-59W, 1959.

34. MacCormack, R., and Paullay, A., "The Influence of the Computational Mesh on Accuracy for Initial Value Problems with Discontinuous or Nonunique Solutions," _Computers and Fluids_, 2, 1974, pp. 339-362.

35. Rose, W. C., "Practical Aspects of Using Navier-Stokes Codes for Predicting Separated Flows," AIAA Paper 76-96, AIAA 14th Aerospace Sciences Meeting, 1976.

36. Hopkins, E. J., and Inouye, M., "An Evaluation of Theories for Predicting Turbulent Skin Friction and Heat Transfer on Flat Plates at Supersonic and Hypersonic Mach Numbers," _AIAA J._, 9, 1971, pp. 993-1003.

37. Sun, C. C., and Childs, M. E., "Wall-Wake Velocity Profile for Compressible Nonadiabatic Flows," _AIAA J._, 14, 1976, pp. 820-822.

38. Law, C. H., "Supersonic Shock Wave Turbulent Boundary Layer Interactions," _AIAA J._, 14, 1976, pp. 730-734.

39. Shang, J. S., Private Communication, June 1979.

40. Horstman, C. C., and Hung, C. M., "Computation of Three-Dimensional Turbulent Separated Flows at Supersonic Speeds," AIAA Paper 79-0002, AIAA 17th Aerospace Sciences Meeting, 1979.

41. Hopkins, E. J., Jillie, D. W., and Sorensen, V. L., "Charts for Estimating Boundary-Layer Transition on Flat Plates," NASA TN-D-5846, June 1970.

42. Shang, J. S., Buning, P. G., Hankey, W. L., Jr., and Wirth, W. C., "The Performance of a Vectorized 3-D Navier-Stokes Code on the CRAY-1 Computer," AIAA 4th Computational Fluid Dynamics Conference, July 1979.

43. Stava, D. J., Private Communication, June 1979.

44. Weilmuenster, K. J., and Howser, L. M., "Solution of a Large Hydrodynamic Problem Using the STAR 100 Computer," NASA TMX-73904, May 1976.

APPENDIX

Details of Computational Sublayer Technique

The finite-difference algorithm of MacCormack as employed in the present case consists of the application of a sequence of one-dimensional finite-difference operators. Denote a sequence of time levels $t^n = n\Delta t$, $n = 1, 2, 3, \ldots$, where Δt is the time step, and a set of finite-difference mesh points (ζ_i, η_j) where

$$\zeta_i = (i - 1)\Delta\zeta \qquad\qquad i = 1, 2, \ldots, IL$$

$$\eta_j = (j - 1)\Delta\eta \qquad\qquad j = 1, 2, \ldots, JL$$

where $\Delta\zeta = 1/(IL - 1)$ and $\Delta\eta = 1/(JL - L)$ are constant. The vector $U_{i,j}$ at position (ζ_i, η_j) and time t^n is updated to time t^{n+1} according to

$$U_{i,j}^{n+1} = L(\Delta t) U_{i,j}^n \tag{A-1}$$

where $L(\Delta t)$ is a symmetric sequence of one-dimensional difference operators $L_\zeta(\Delta t_\zeta)$ and $L_\eta(\Delta t_\eta)$. Using the dummy time indices $*$ and $**$ with

$$U_{i,j}^{**} = L_\zeta(\Delta t_\zeta) U_{i,j}^* \tag{A-2}$$

the L_ζ operator is given by the following two-step predictor-corrector method:

Predictor step: $\quad \overline{U_{i,j}^{**}} = U_{i,j}^* - \dfrac{\Delta t_\zeta}{\Delta\zeta} (F_{i,j}^* - F_{i-1,j}^*)$

$$\tag{A-3}$$

Corrector step: $\quad U_{i,j}^{**} = \frac{1}{2}[U_{i,j}^* + \overline{U_{i,j}^{**}} - \dfrac{\Delta t_\zeta}{\Delta\zeta} (\overline{F_{i+1,j}^{**}} - \overline{F_{i,j}^{**}})]$

where $F_{i,j}^*$ implies the flux terms are evaluated using $U_{i,j}^*$ and so forth. Similarly, the $L_\eta(\Delta t_\eta)$ operator is given by

Predictor Step: $\quad \overline{U_{i,j}^{**}} = U_{i,j}^* - \dfrac{\Delta t_\eta}{\Delta\eta} (G_{i,j}^* - G_{i,j-1}^*)$

$$\tag{A-4}$$

Corrector step: $\quad U_{i,j}^{**} = \frac{1}{2}[U_{i,j}^* + \overline{U_{i,j}^{**}} - \dfrac{\Delta t_\eta}{\Delta\eta} (\overline{G_{i,j+1}^{**}} - \overline{G_{i,j}^{**}})]$

The details of the construction of the $L(\Delta t)$ operator from the operators L_ζ and L_η are indicated in Reference A-1, and the treatment of the stress terms in the fluxes F and G is discussed in References A-2 and A-3.

The details of the mesh arrangement in the computational sublayer (CSL) are illustrated in Figure A-1. The set of mesh points on which MacCormack's method is applied (called the "ordinary" mesh) is denoted by the open symbols. The row of ordinary points adjacent to the wall is called the "matching" points (i.e., the rows $j = 2$ and $j = JL - 1$). The region between the row of matching points and the wall is the computational sublayer, in which a separate mesh of points (indicated by the closed symbols) is employed.

The mesh spacing for the ordinary points provides sufficient resolution of all pertinent flow features, except at the row of matching points. Specifically, in updating the flow variables on the row of matching points near $\eta = 0$, among the quantities required are the components of the cartesian stress tensor τ_{xx}, τ_{xy}, τ_{yy} and heat transfer vector Q_x and Q_y at the wall (in the predictor step of the L_η operator) and at the row of matching points (in the corrector step of the L_η operator and in both steps of the L_ζ operator). In these specific instances, the η-derivatives of the temperature and velocity components would be approximated using values at $j = 1$ and $j = 2$ or $j = 1$ and $j = 3$ depending on the operator. However, with the computational sublayer technique, the mesh spacing y_m is substantially greater than the viscous sublayer thickness, and such an approximation for the derivatives would be highly inaccurate. Instead, the computational sublayer technique is used to provide accurate values for τ_{xx}, τ_{xy}, τ_{yy}, Q_x and Q_y when updating the flowfield at the row of matching points, according to the following table.

TABLE A-1. INCORPORATION OF COMPUTATIONAL
SUBLAYER METHOD

Row of Matching Points	Rows on which CSL supplies values for stress and heat transfer components	
	L_ζ operator	L_η operator
$j = 2$	$j = 2$ (Predictor) $j = 2$ (Corrector)	$j = 1$ (Predictor) $J = 2$ (Corrector
$j = JL -1$	$j = JL - 1$ (Predictor) $j = JL - 1$ (Corrector)	$j = JL - 1$ (Predictor) $j = JL$ (Corrector)

The components of the cartesian stress tensor are obtained from the sublayer solution by a simple coordinate transformation, under the reasonable assumption that the normal stresses in the (x',y') coordinate system (i.e., $\tau_{x'x'}$ and $\tau_{y'y'}$) are small compared to $\tau_{x'y'}$. For the computational sublayer on $\eta = 0$,

$$\tau_{xx} = -2 \sin\theta \cos\theta \, \tau_{x'y'}$$

$$\tau_{xy} = (\cos^2\theta - \sin^2\theta)\tau_{x'y'} \qquad \text{(A-5)}$$

$$\tau_{yy} = +2 \sin\theta \cos\theta \, \tau_{x'y'}$$

Similarly, the components of the heat transfer vector are obtained assuming that $Q_{x'} \ll Q_{y'}$, and thus

$$Q_x = -\sin\theta \, Q_{y'}$$

$$Q_y = \cos\theta \, Q_{y'} \qquad \text{(A-6)}$$

Expressions can be similarily derived for the computational sublayer on $\eta = 1$.

The method of solution of the sublayer equations (14) to (16) is discussed in Reference A-1. The computational sublayer technique is similar to previous work by Baldwin and MacCormack (Ref. A-4) and Baldwin and Lomax (Ref. A-5). In the former case, an iterative procedure was employed using the full boundary layer equations to provide values of all variables at the second row of ordinary mesh points from the wall. The method differs from the present technique principally in its inclusion of the streamwise flux terms (i.e., $\frac{\partial \rho u'}{\partial x'}$, $\frac{\partial \rho u'}{\partial x'}$, etc.) which were found in all present calculations to be insignificant as indicated in Sections III.D and III.E. A similar conclusion was reached by Baldwin and MacCormack for the cases considered in Reference A-4. The latter technique (Reference A-5) differs from the present method in its assumption that $\tau_{x'y'}$ is constant throughout the sublayer (taken to be $0 < y'_m \leq 50 \, \nu_w/u_*$ in Ref. A-5) which is invalid in the vicinity of large streamwise pressure gradients.

References

A-1. Knight, D. D., "Calculation of High Speed Inlet Flows Using the Navier-Stokes Equations. Volume II: User's and Programmer's Guide," AFFDL-TR

A-2 MacCormack, R. W., and Baldwin, B. S., "A Numerical Method for Solving the Navier-Stokes Equations with Application to Shock-Boundary Layer Interactions," AIAA Paper 75-1, AIAA 13th Aerospace Sciences Meeting, 1975.

A-3. Knight, D. D., and Hankey, W. L., Jr., "Numerical Simulation of Non-Chemically Reacting Supersonic Diffusion Laser," AIAA Paper 76-60, AIAA 14th Aerospace Sciences Meeting, 1976.

A-4. Baldwin, B. S., and MacCormack, R. W., "Numerical Solution of the Interaction of a Strong Shock Wave with a Hypersonic Turbulent Boundary Layer," AIAA Paper 74-558, June 1974.

A-5 Baldwin, B. S., and Lomax, H., "Thin Layer Approximation and Algebraic Model for Separated Turbulent Flows," AIAA Paper 78-257, January 1978.
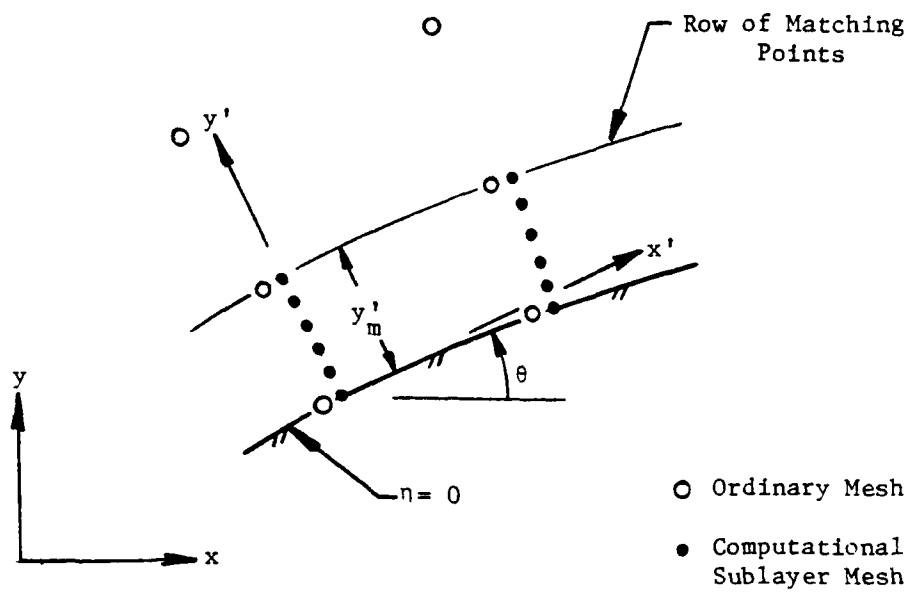
a) Computational Sublayer on $\eta = 0$
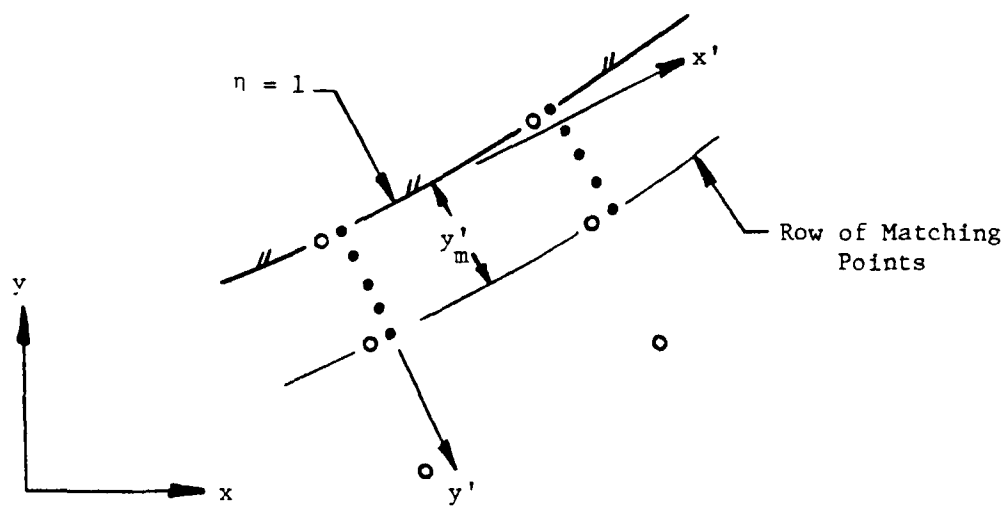
b) Computational Sublayer on $\eta = 1$

Figure A-1.   Computational Sublayer Geometry
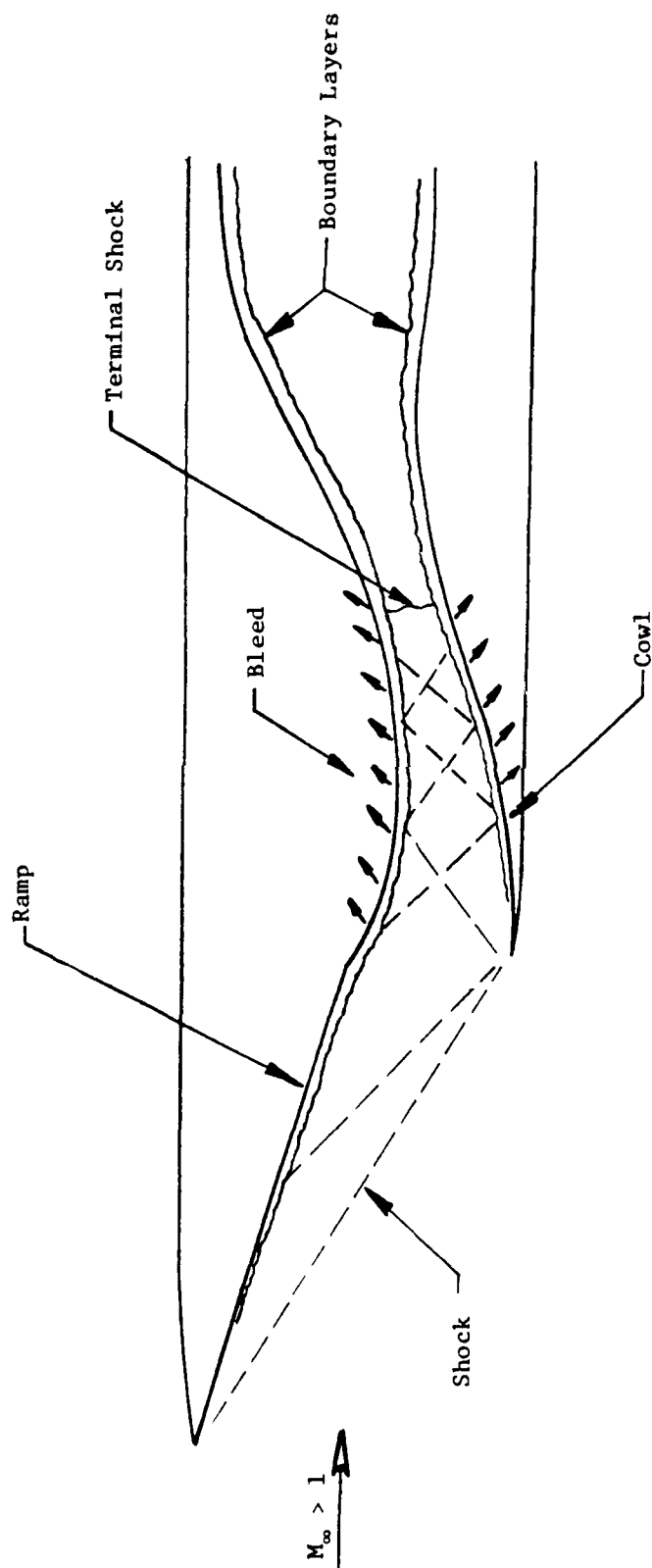
Figure 1. Characteristics of Mixed Compression High Speed Inlet (from Ref. 2).

48
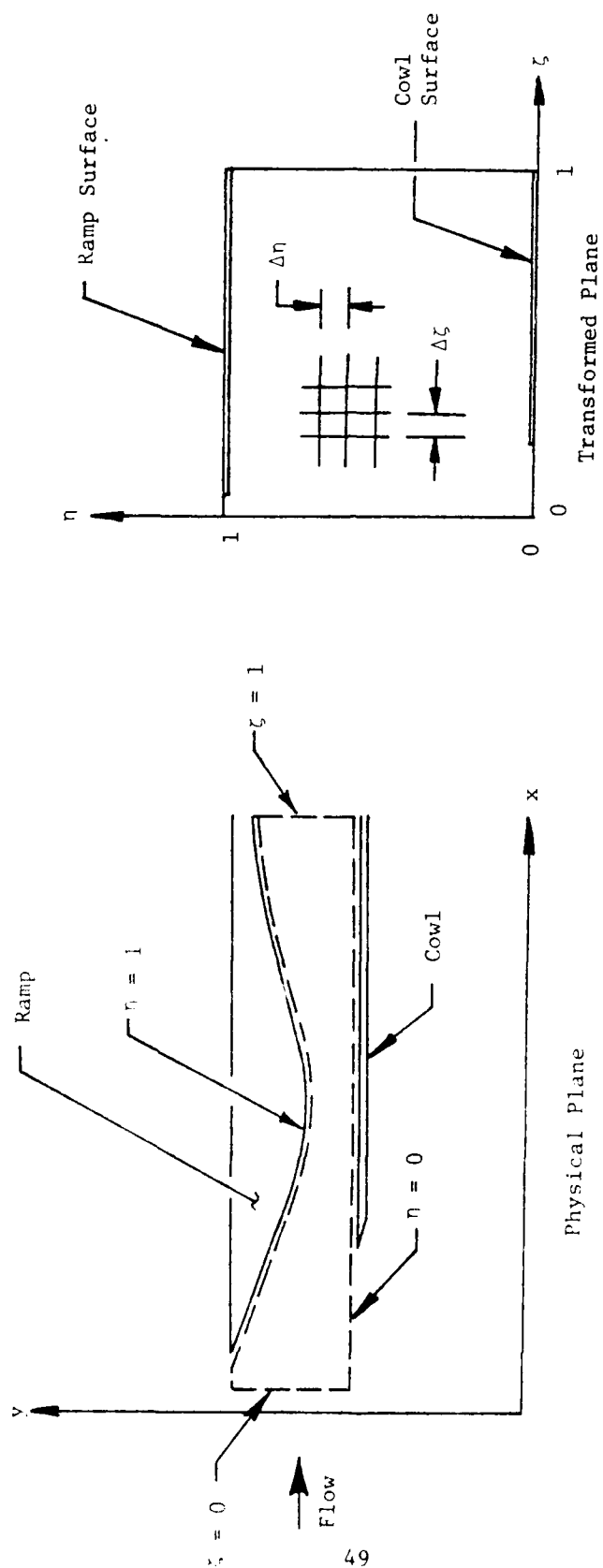
Figure 2. Coordinate Transformation

49

Upstream Boundary: AD
Downstream Boundary: CF
Wall Boundary: BC and EF
No-Reflection Boundary: AB and DE
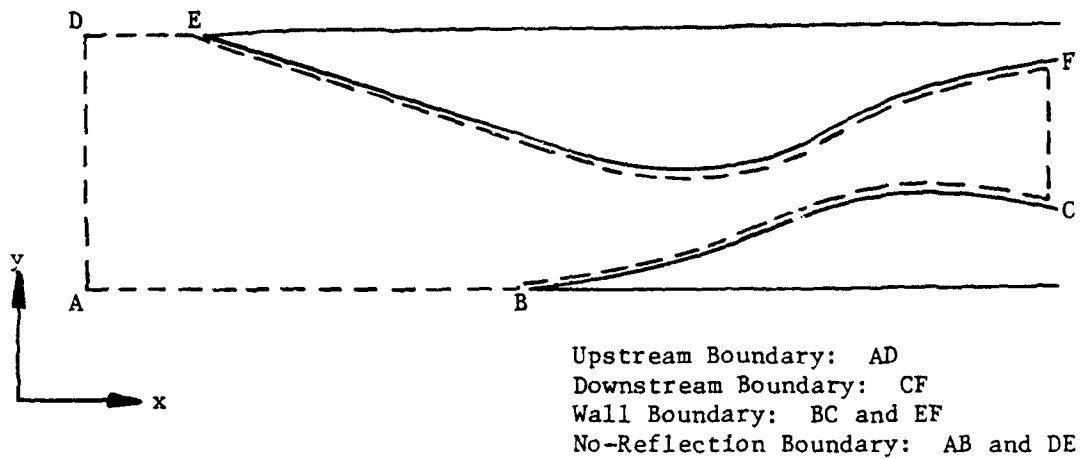
a) Types of Boundary Conditions
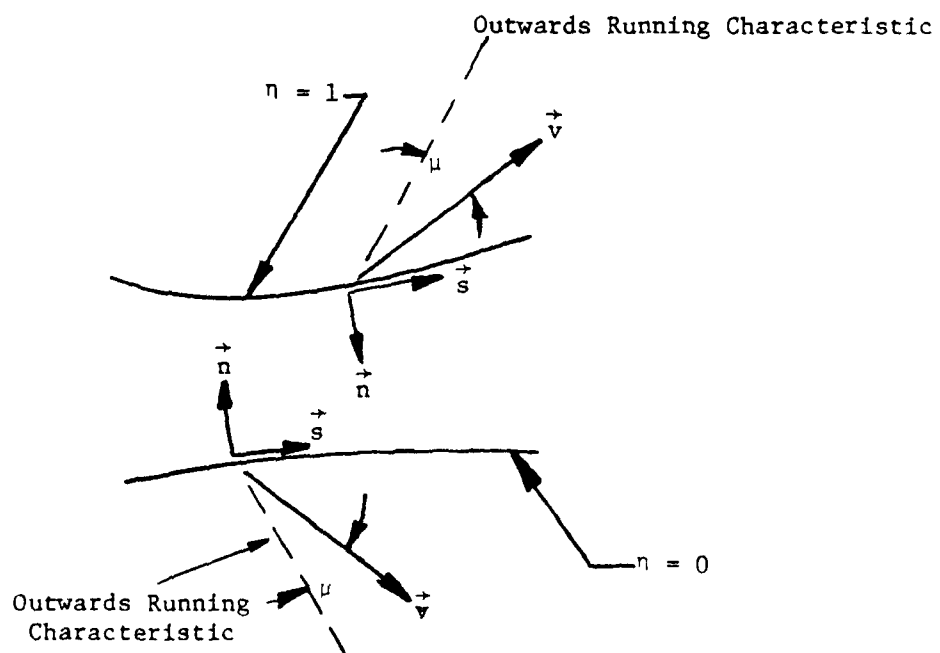
b) Orientation of Unit Vectors and
Outwards Running Characteristics

Figure 3. Boundary Conditions
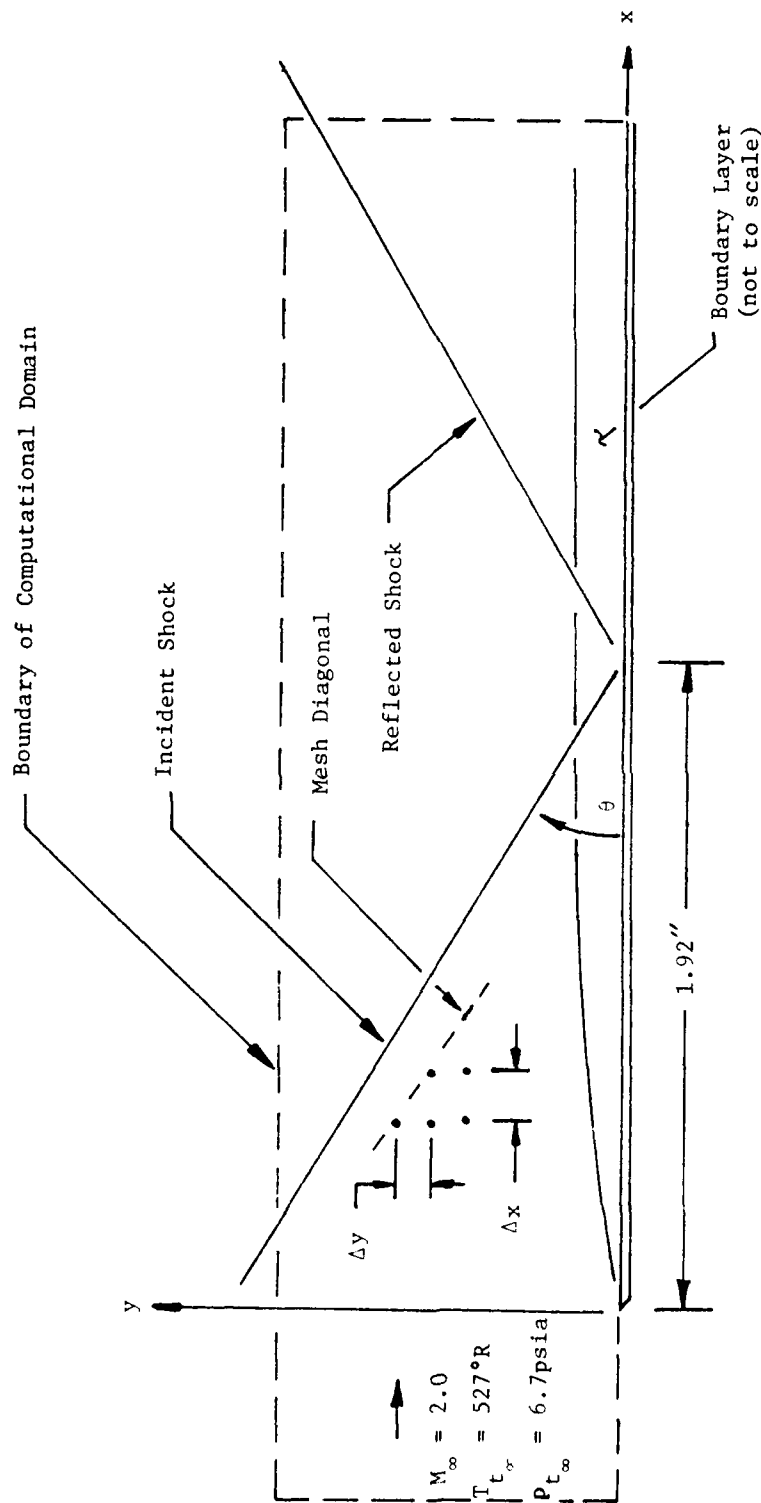
Figure 4. Shock-Laminar Boundary Layer Interaction

51
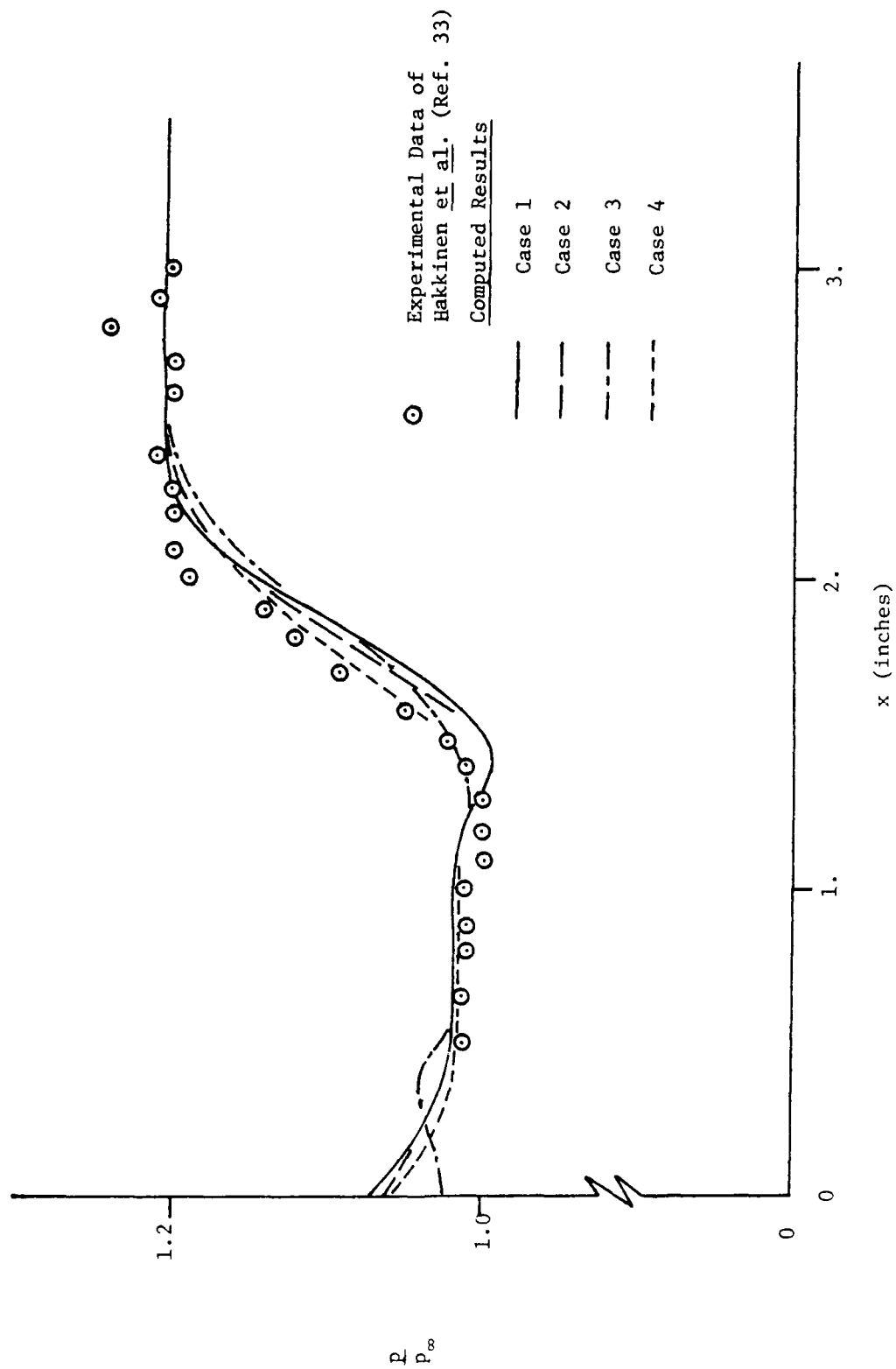
Figure 5. Surface Pressure for Shock-Laminar Boundary Layer Interaction

52
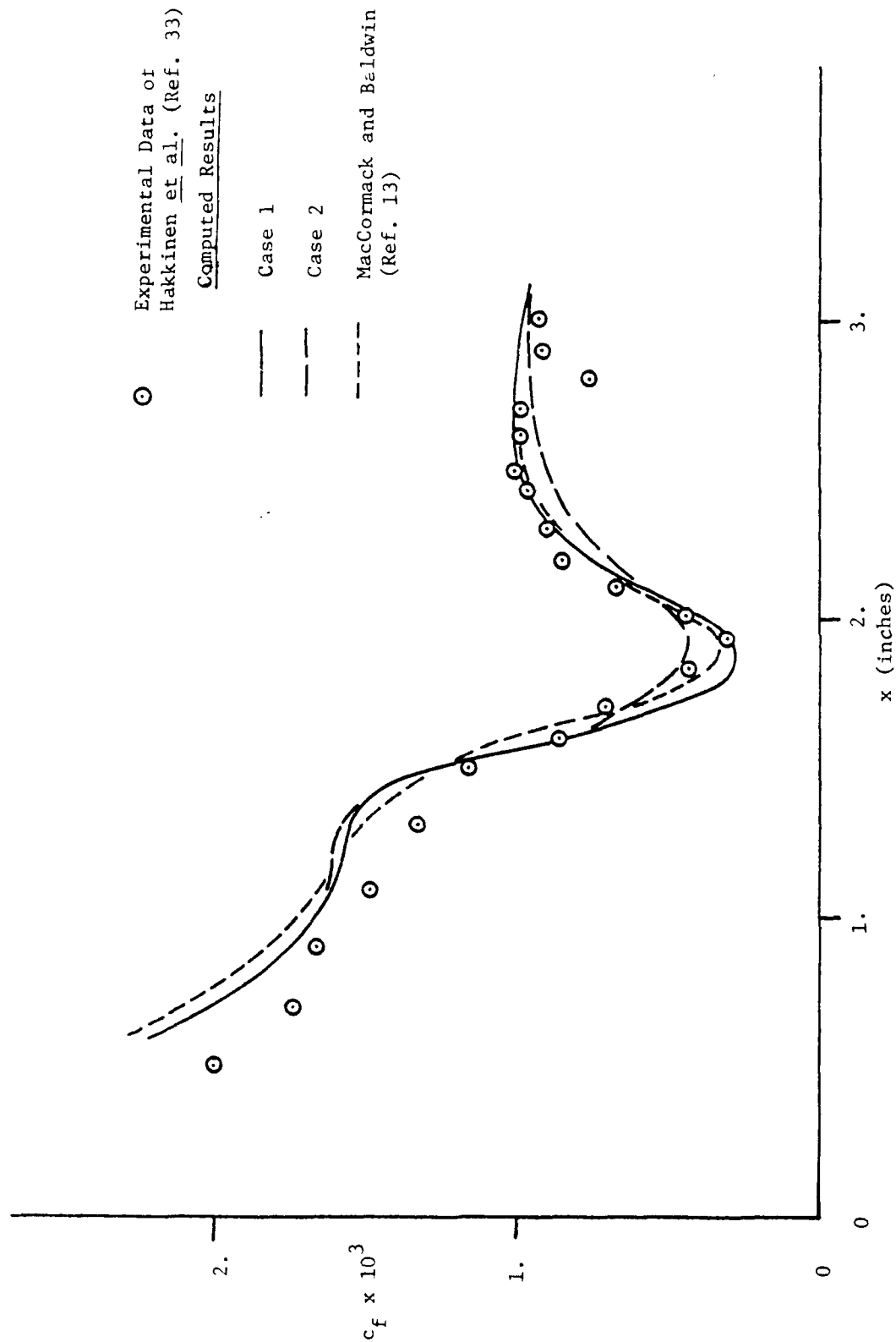
Figure 6. Skin Friction Coefficient for Shock-Laminar Boundary Layer Interaction (Geometric/Uniform Mesh Distribution)

53
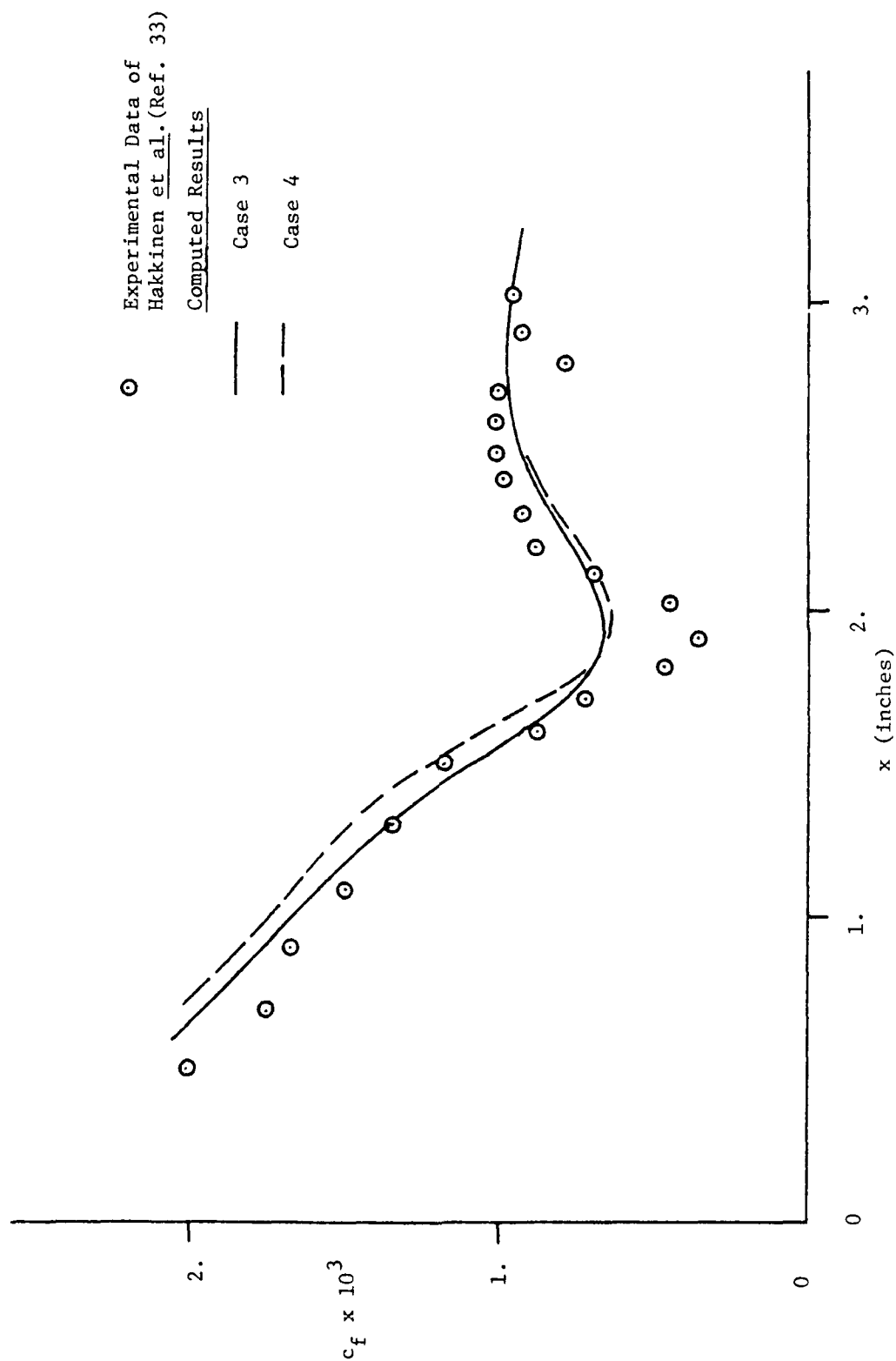
Figure 7. Skin Friction Coefficient for Shock-Laminar Boundary Layer Interaction (Geometric Mesh Distribution)

54

Figure 8. Skin Friction Coefficient for Flat Plate
Turbulent Boundary Layer

Symbol	Case	Sublayer Model Used?	Δy_2^+
□	7	Yes	27.8
○	8	Yes	52.1
◇	9	Yes	97.3
△	10	No	3.78
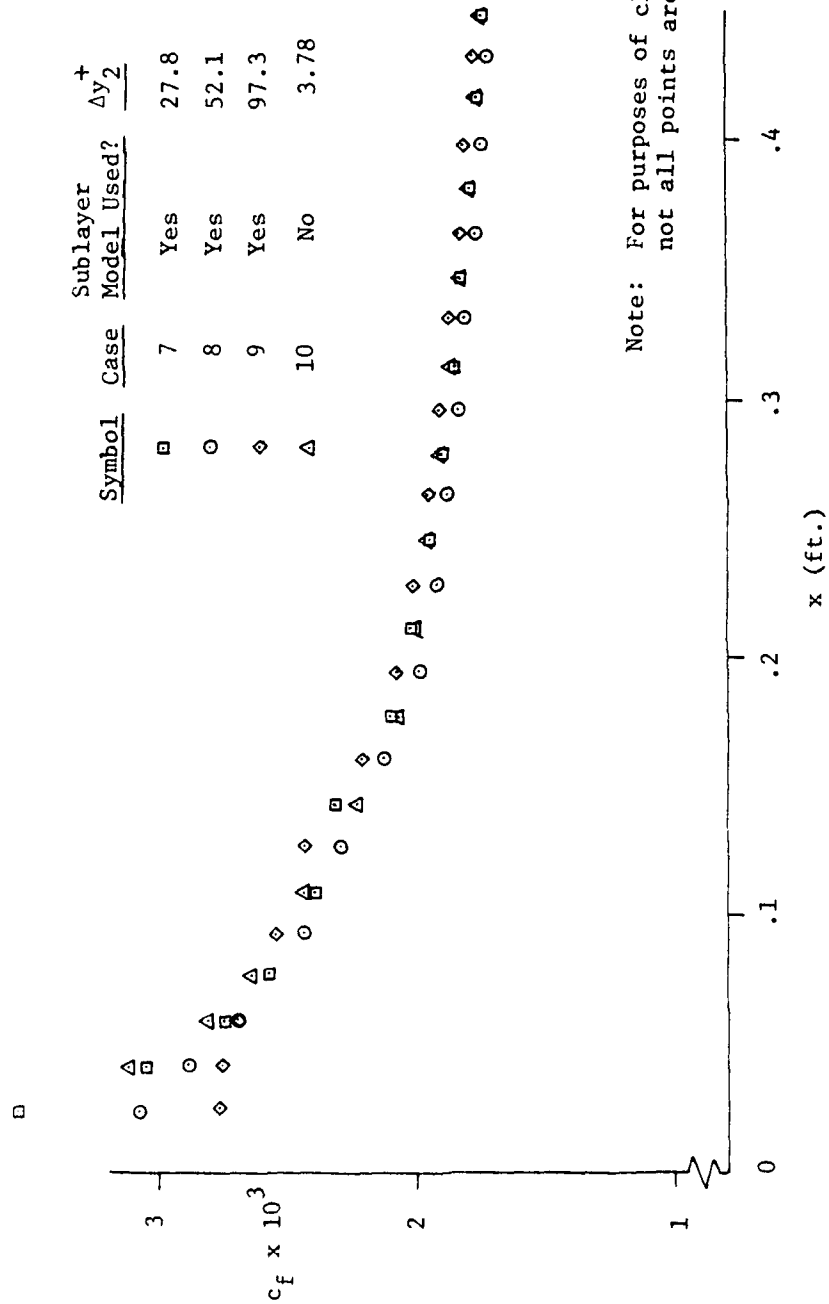
Note: For purposes of clarity,
not all points are shown.
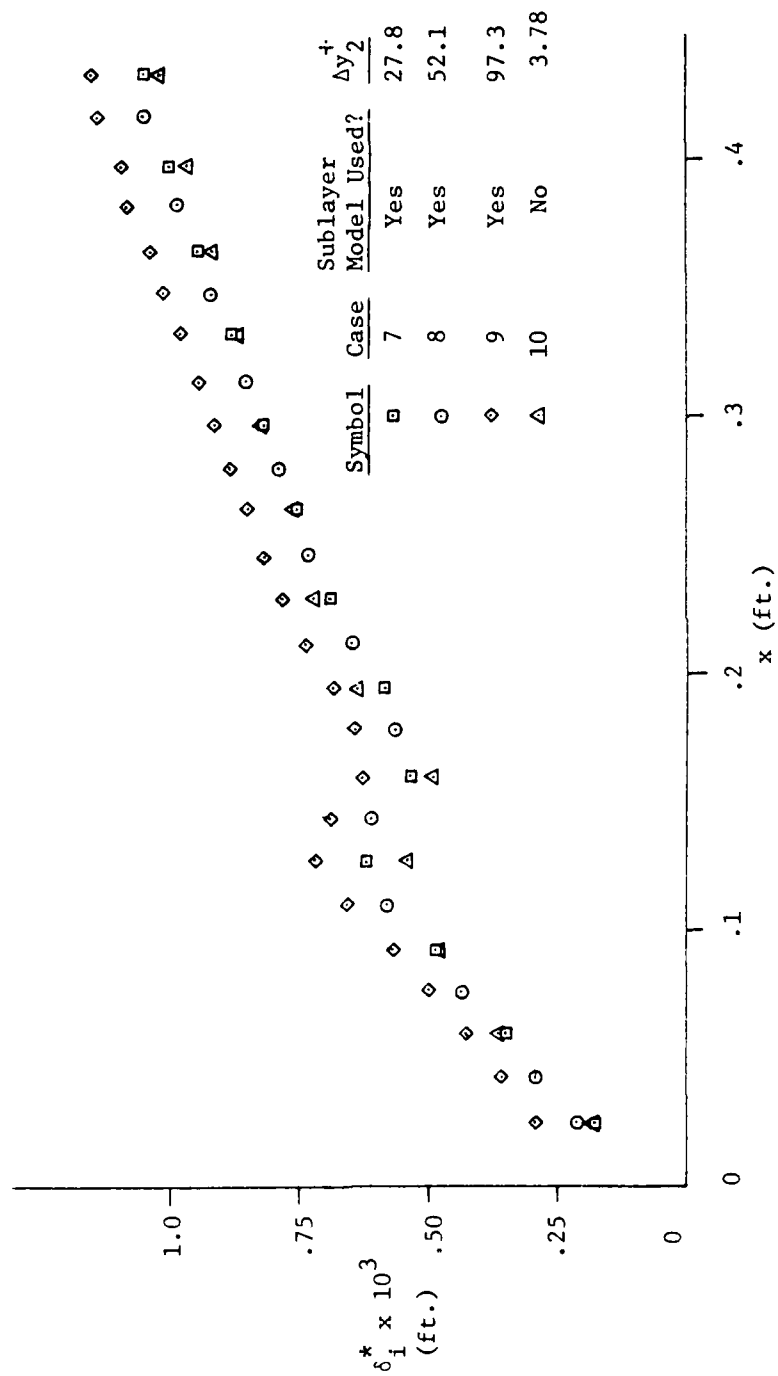
Figure 9. Displacement Thickness for Flat Plate
Turbulent Boundary Layer

1.0

0.8

0.6

$\frac{y}{\delta}$

0.4

0.2

0

Symbol	Case	Sublayer Model Used?	Δy_2^+
▣	7	Yes	27.8
⊙	8	Yes	52.1
△	10	No	3.78

0   0.2   0.4   0.6   0.8   1.0

$(T - T_\infty)/(T_w - T_\infty)$
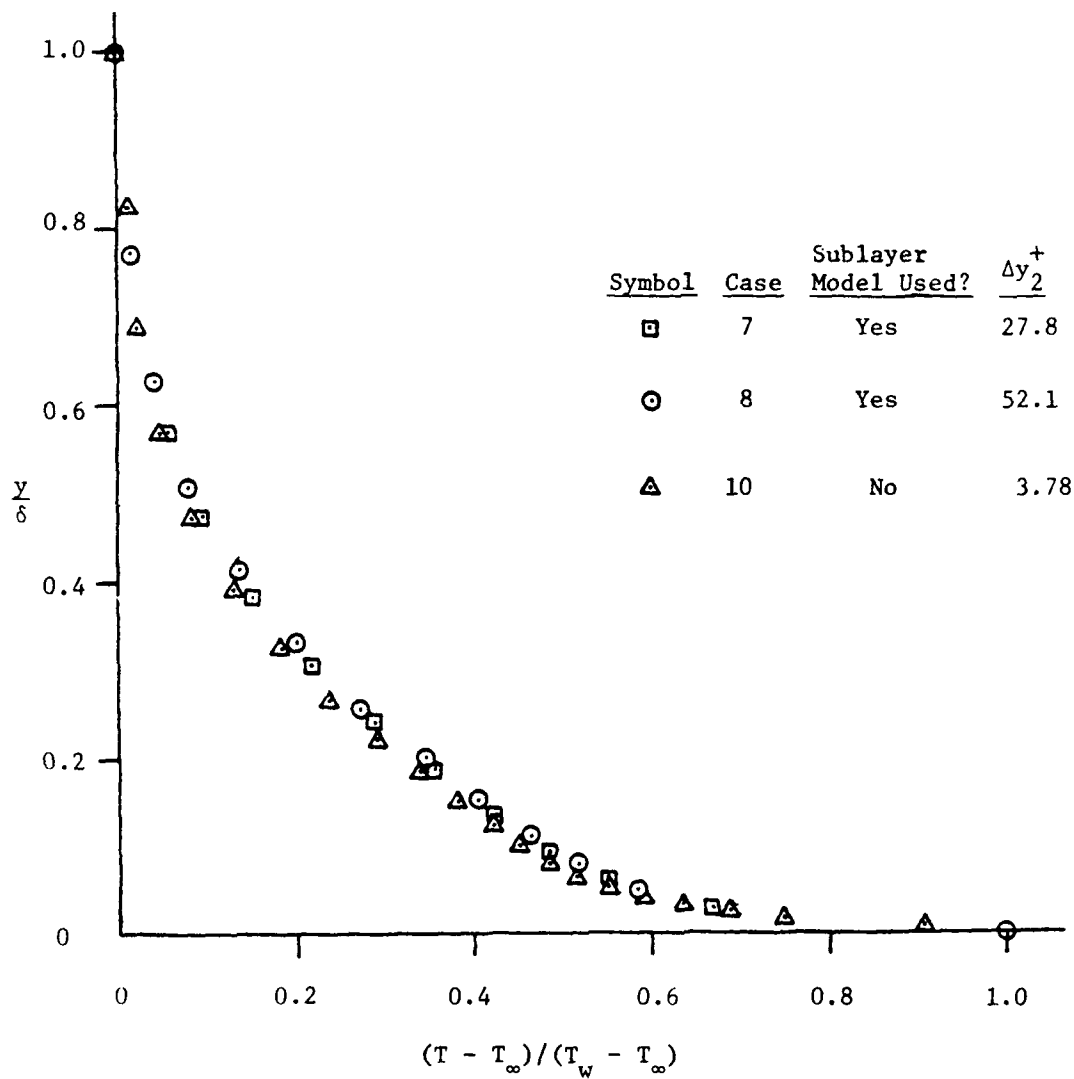
Figure 10a. Static Temperature for Flat Plate Turbulent
Boundary Layer at x = 0.4 ft.

57
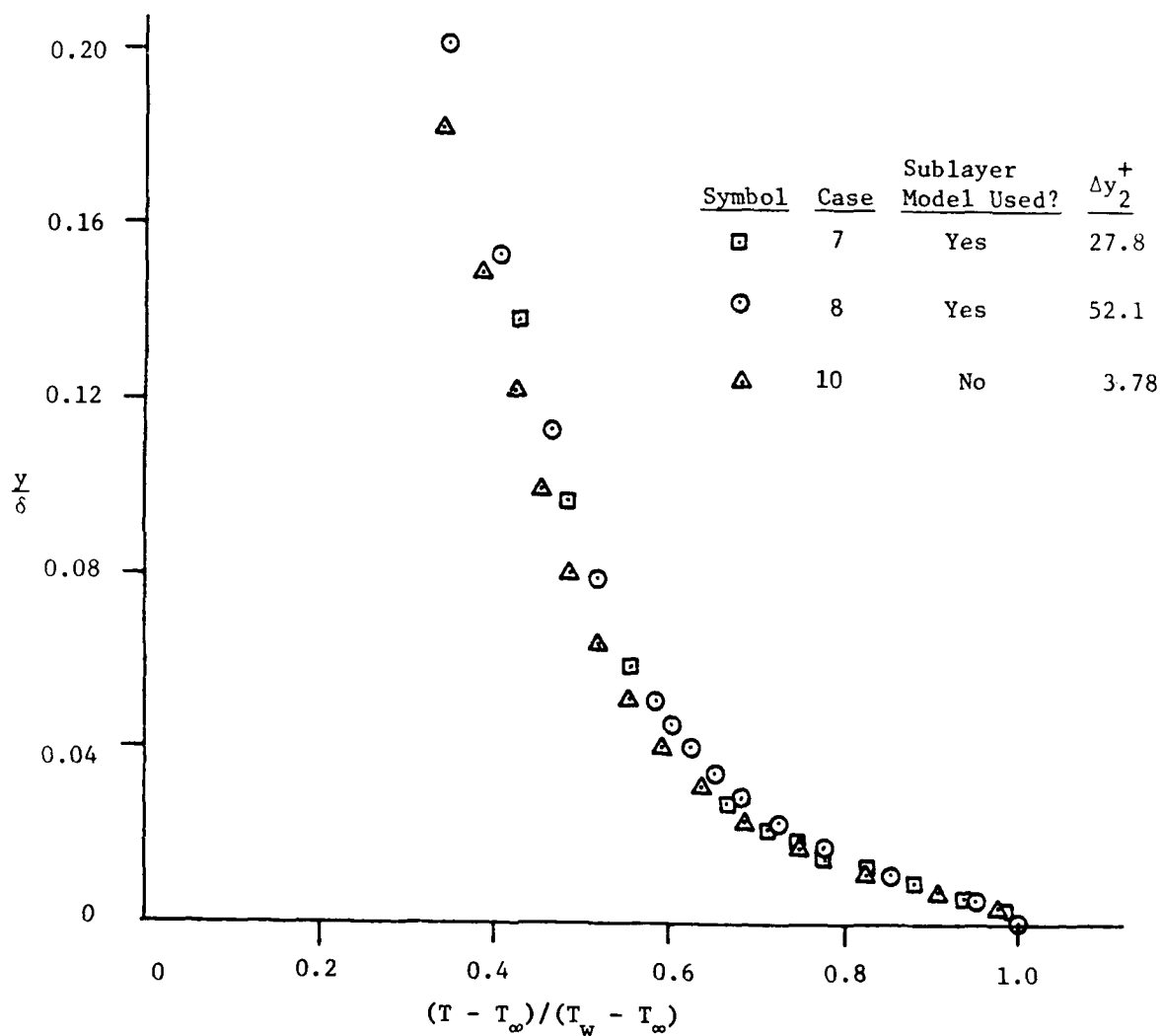
Figure 10b. Static Temperature for Flat Plate Turbulent
Boundary Layer at x = 0.4 ft.
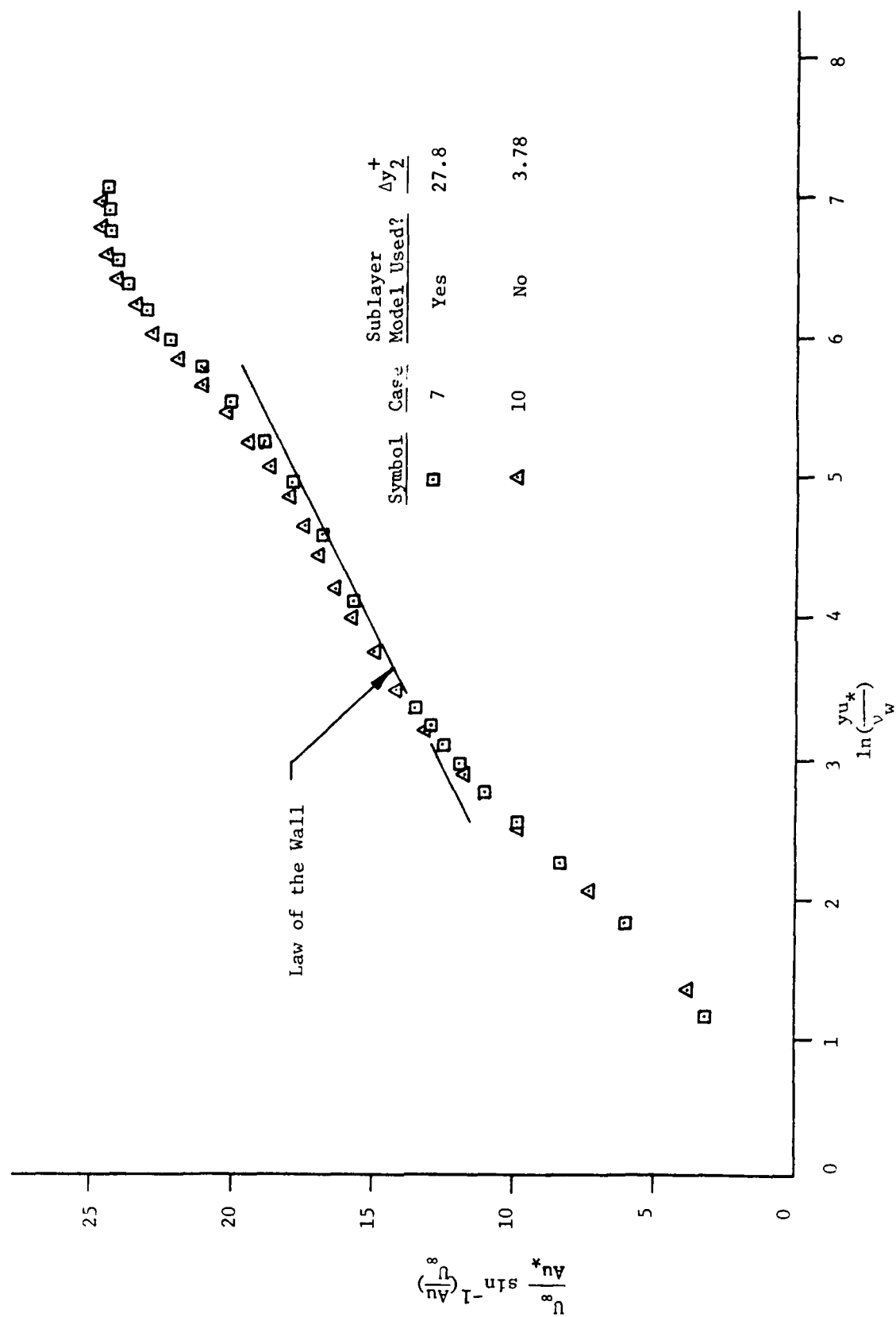
Figure 11. Velocity for Flat Plate Turbulent Boundary Layer at x = 0.4 ft.
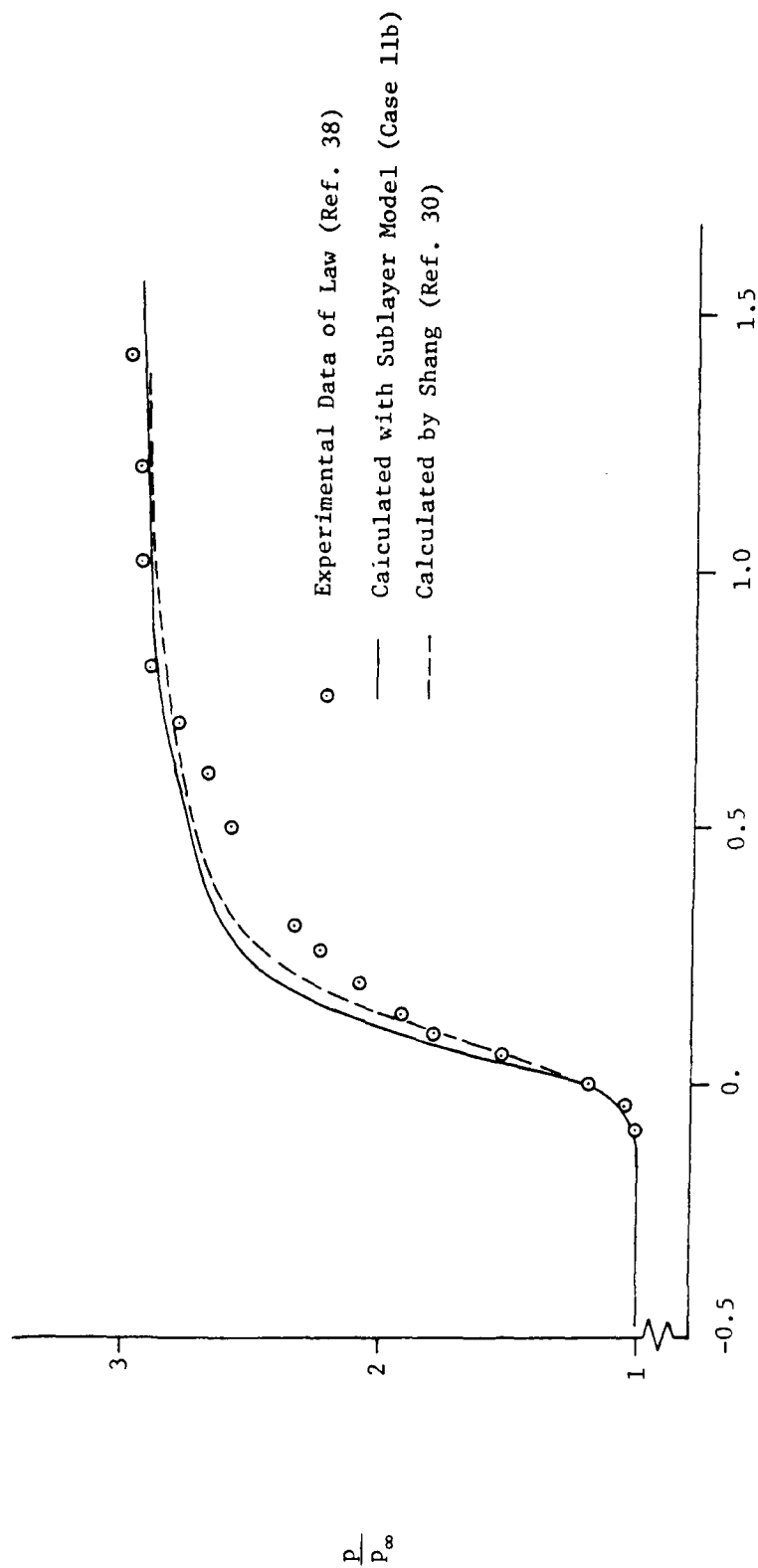
Figure 12. Surface Pressure for Shock-Turbulent
Boundary Layer Interaction

o   Experimental Data of Law (Ref. 38)
———   Calculated with Sublayer Model (Case 11b)
– – – Calculated by Shang (Ref. 30)

$\frac{p}{p_\infty}$
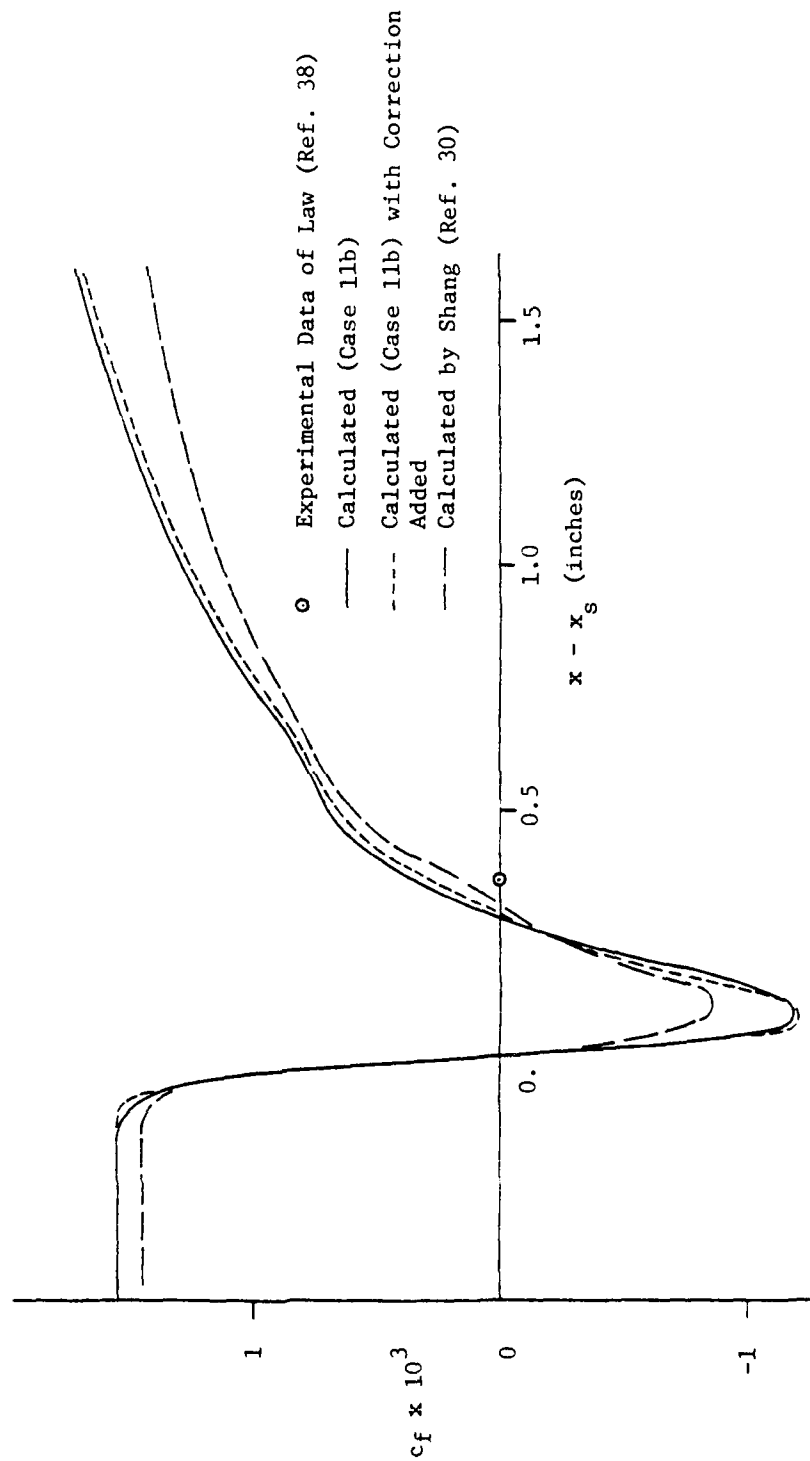
Figure 13. Skin Friction Coefficient for Shock-Turbulent
Boundary Layer Interaction

⊙   Experimental Data of Law (Ref. 38)

———   Calculated (Case 11b)

- - - - Calculated (Case 11b) with Correction
         Added

— —   Calculated by Shang (Ref. 30)

$x - x_s$ (inches)

$c_f \times 10^3$
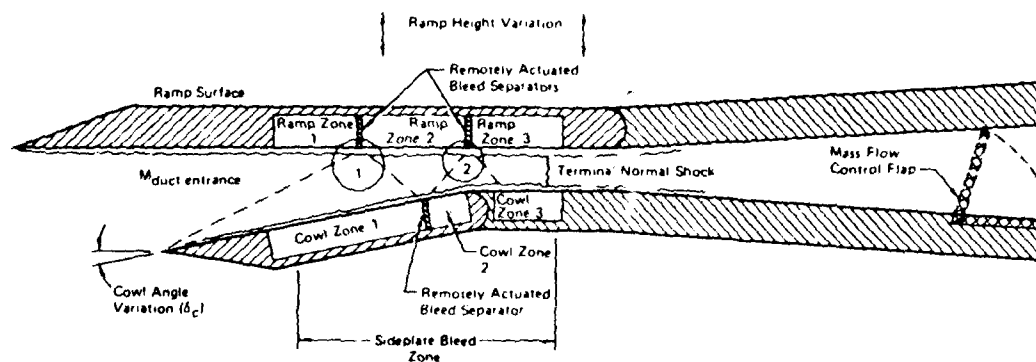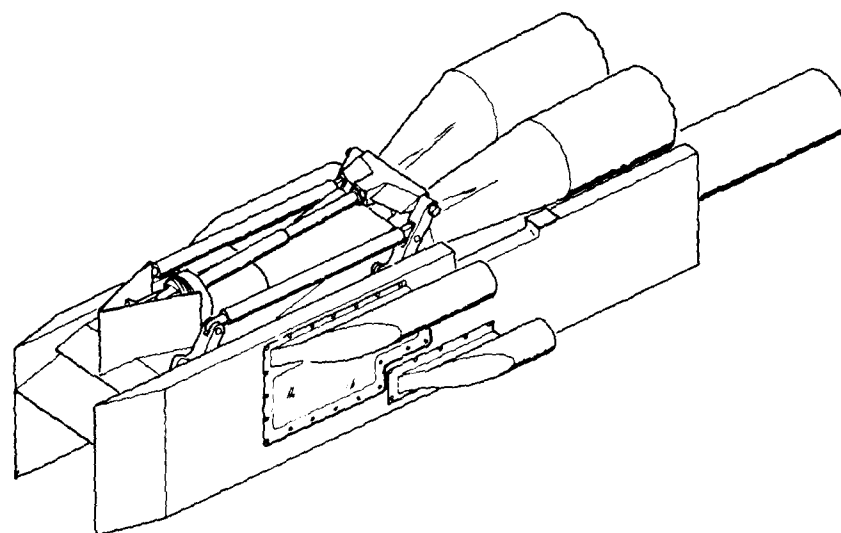
Not to Scale

Figure 14. Simulated High Speed Inlet
McDonnell Aircraft Company (MCAIR)
(from Ref. 2)
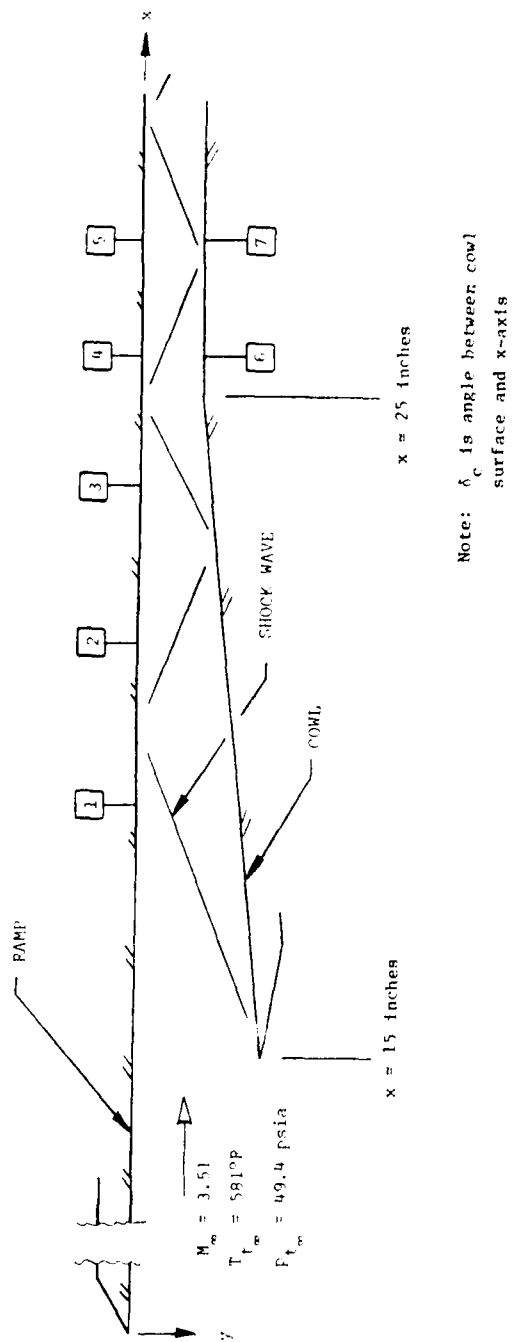
Figure 15. Simulated High Speed Inlet: Location of Pitot Rakes

RAMP

$M_\infty = 3.51$
$T_{t_\infty} = 581^\circ R$
$P_{t_\infty} = 49.4$ psia

x = 15 inches

COWL

SHOCK WAVE

x = 25 inches

Note: δ_c is angle between cowl surface and x-axis

x

63
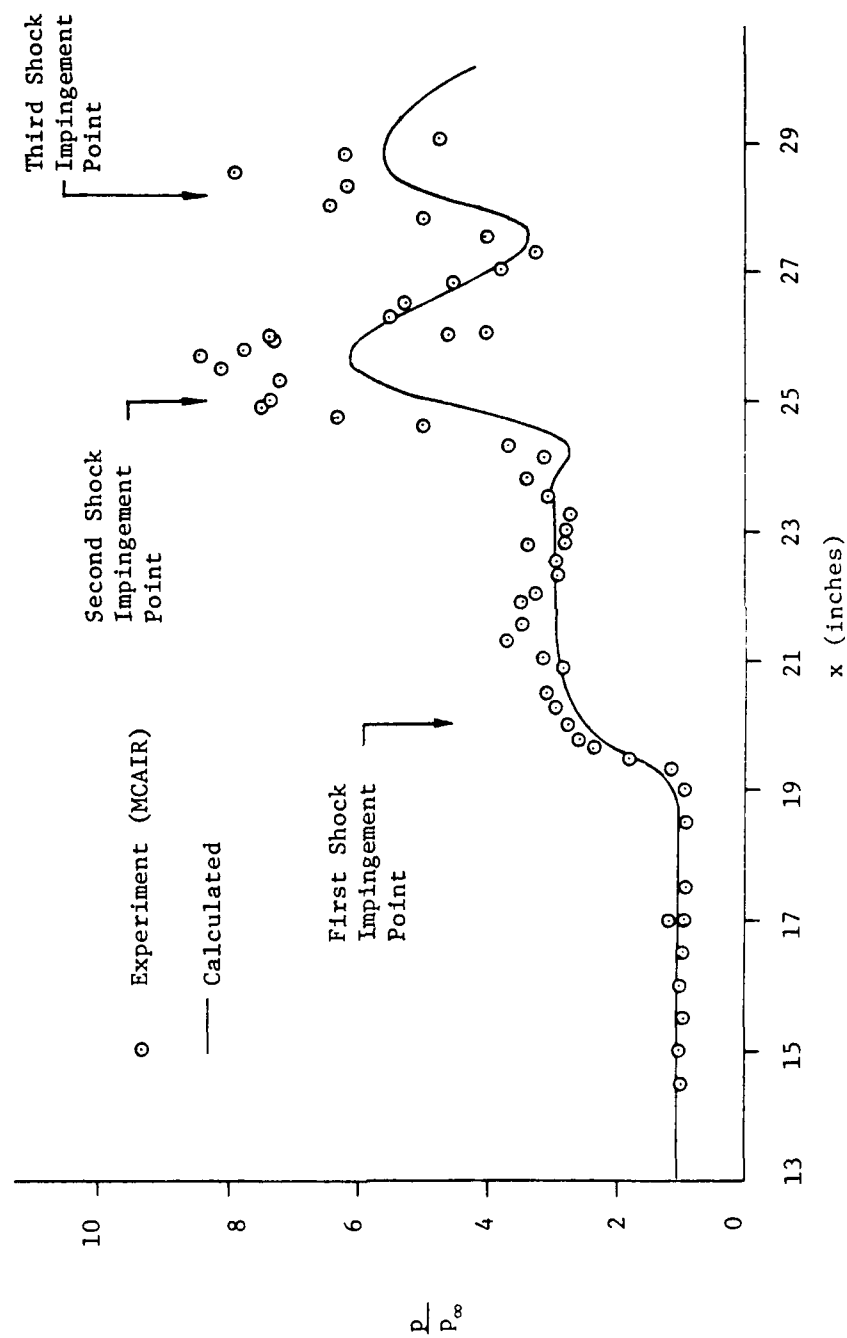
Figure 16. Ramp Surface Pressure for $\delta_c = 6°$
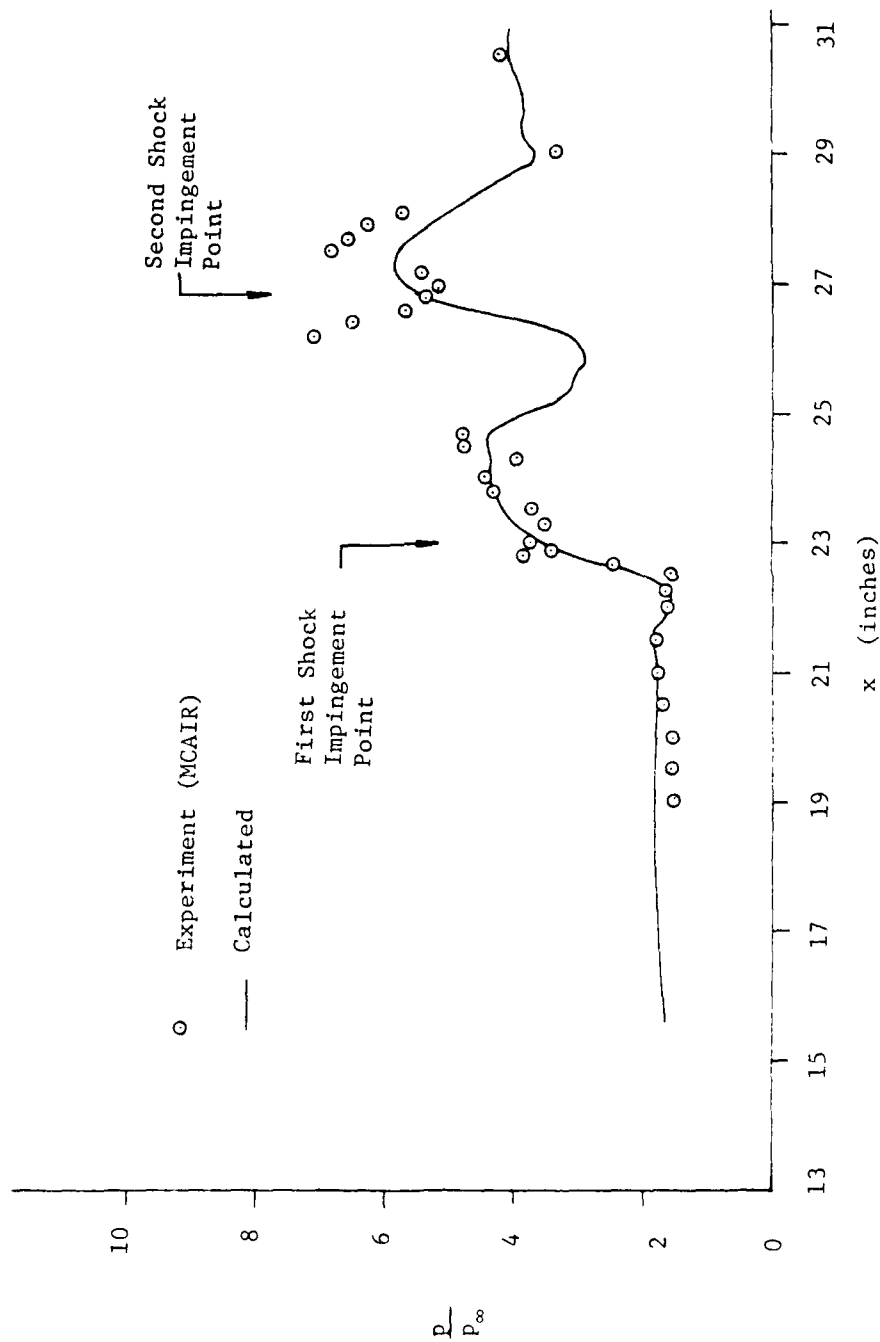
Figure 17. Cowl Surface Pressure for $\delta_c = 6°$
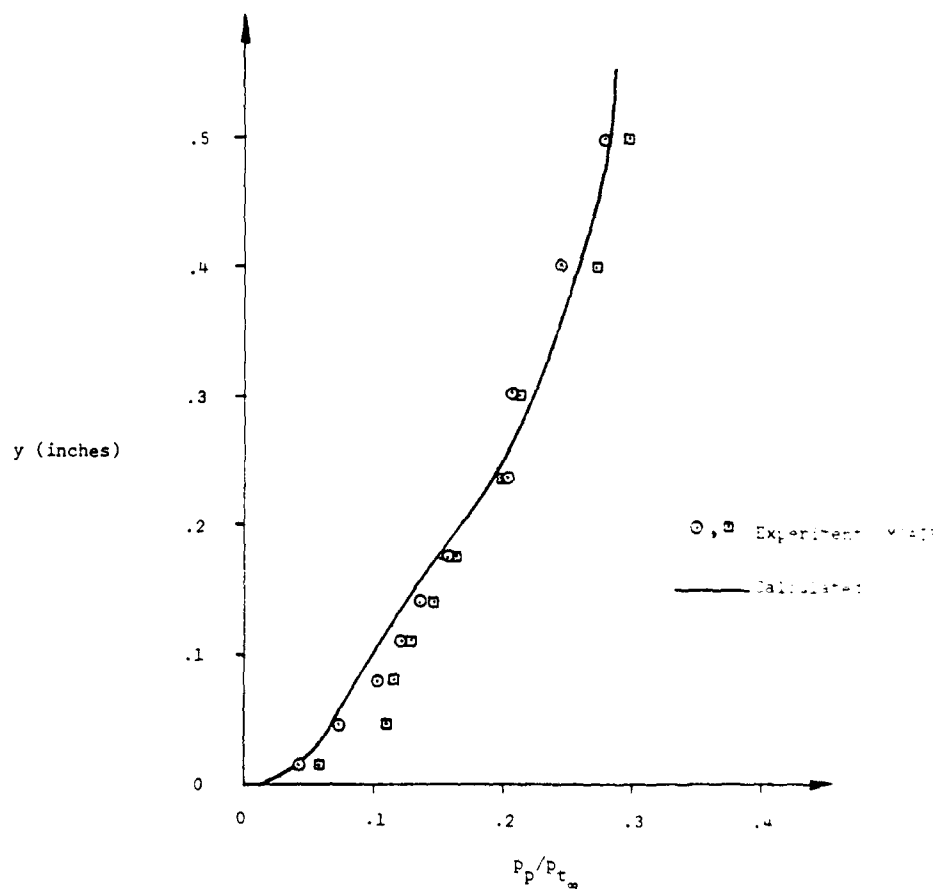
Figure 18. Pitot Pressure on Ramp at Station $\boxed{1}$
for $\delta_c = 6°$
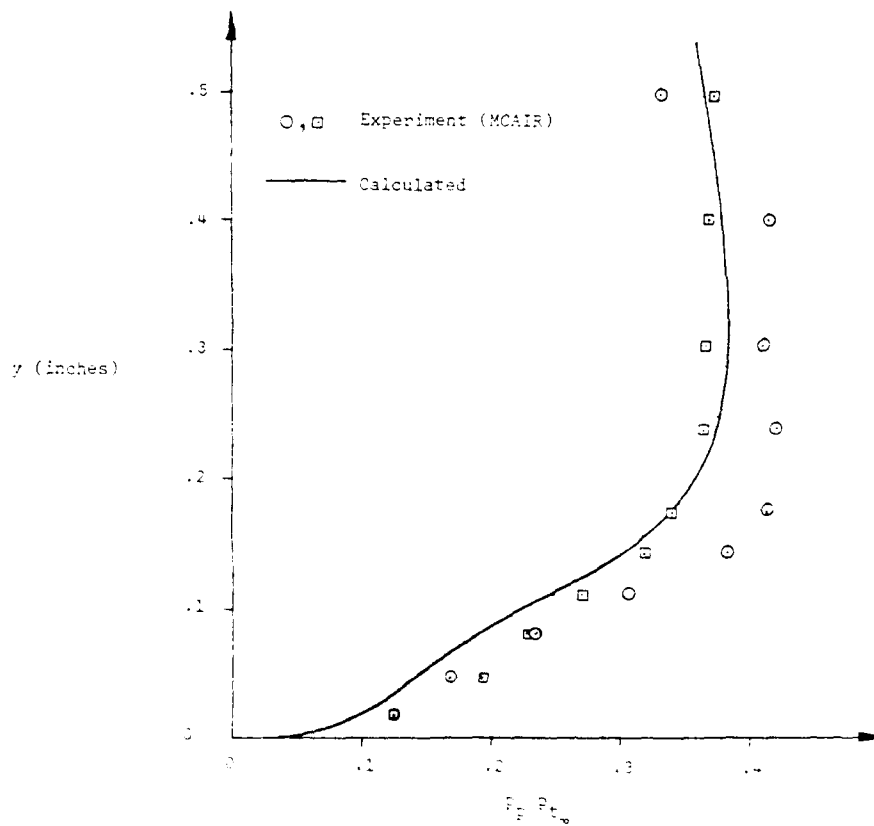
Figure 19. Pitot Pressure on Ramp at Station ②
for $\delta_c = 6°$

67
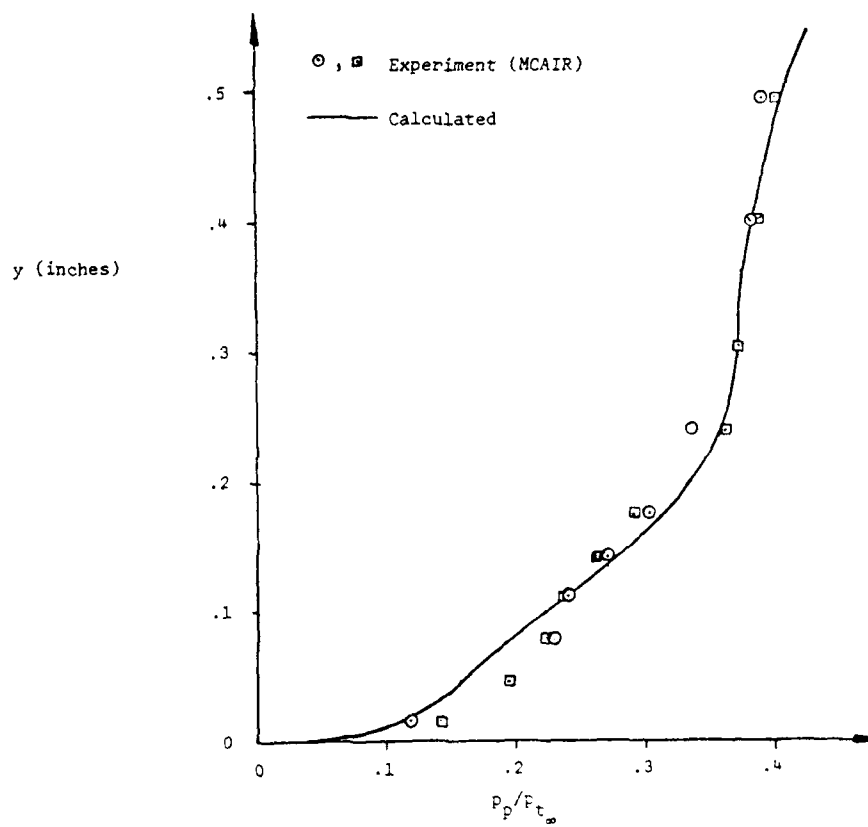
Figure 20. Pitot Pressure on Ramp at Station $\boxed{3}$
for $\delta_c = 6°$
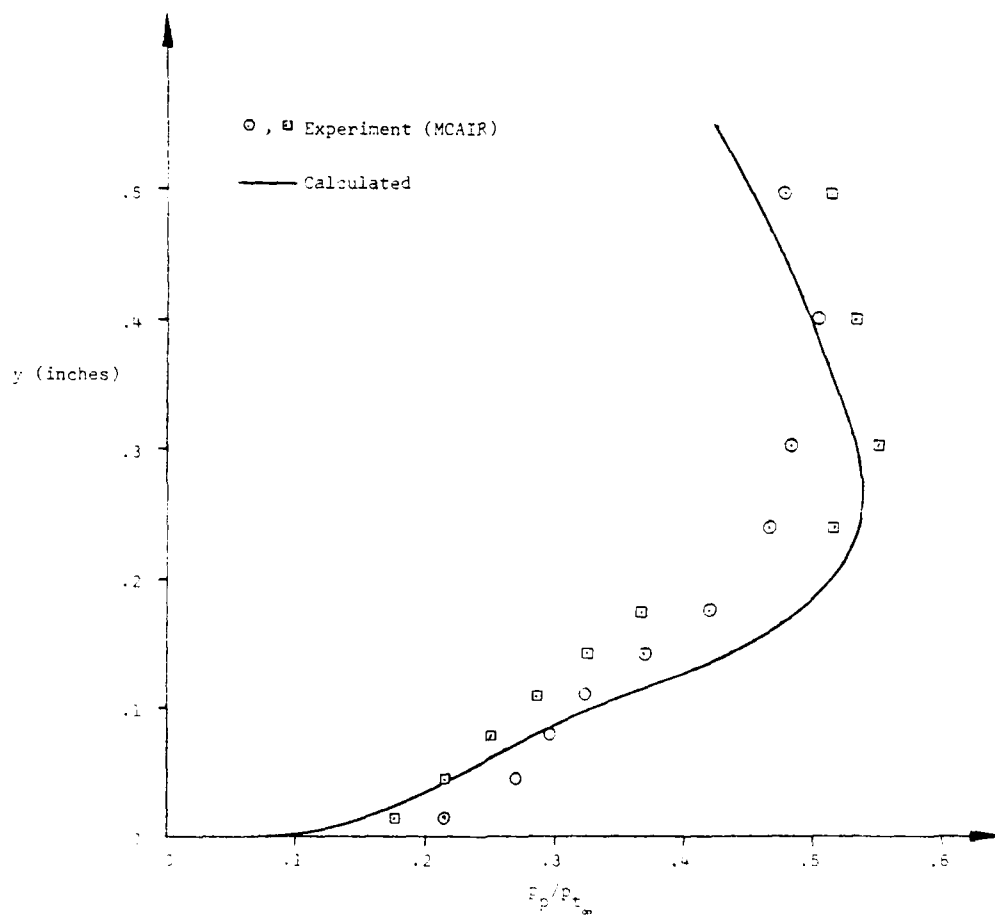
Figure 21.   Pitot Pressure on Ramp at Station $\boxed{4}$
for $\delta_c = 6°$

69
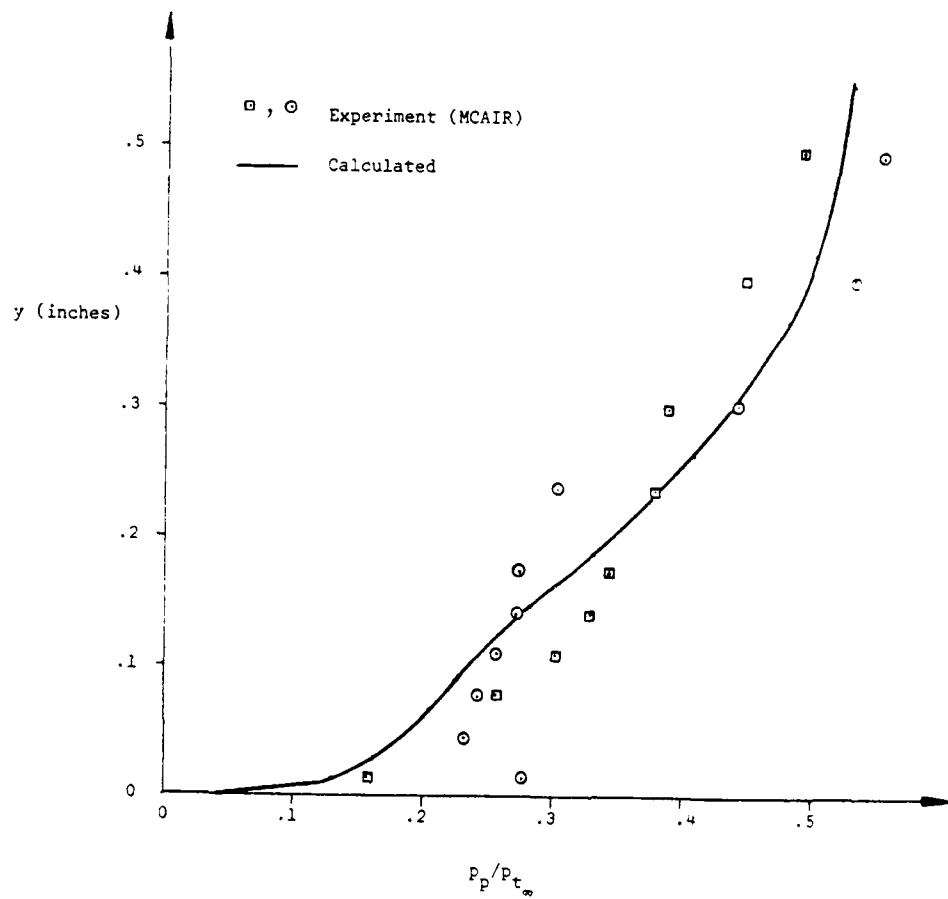
Figure 22. Pitot Pressure on Ramp at Station [5] for $\delta_c = 6°$
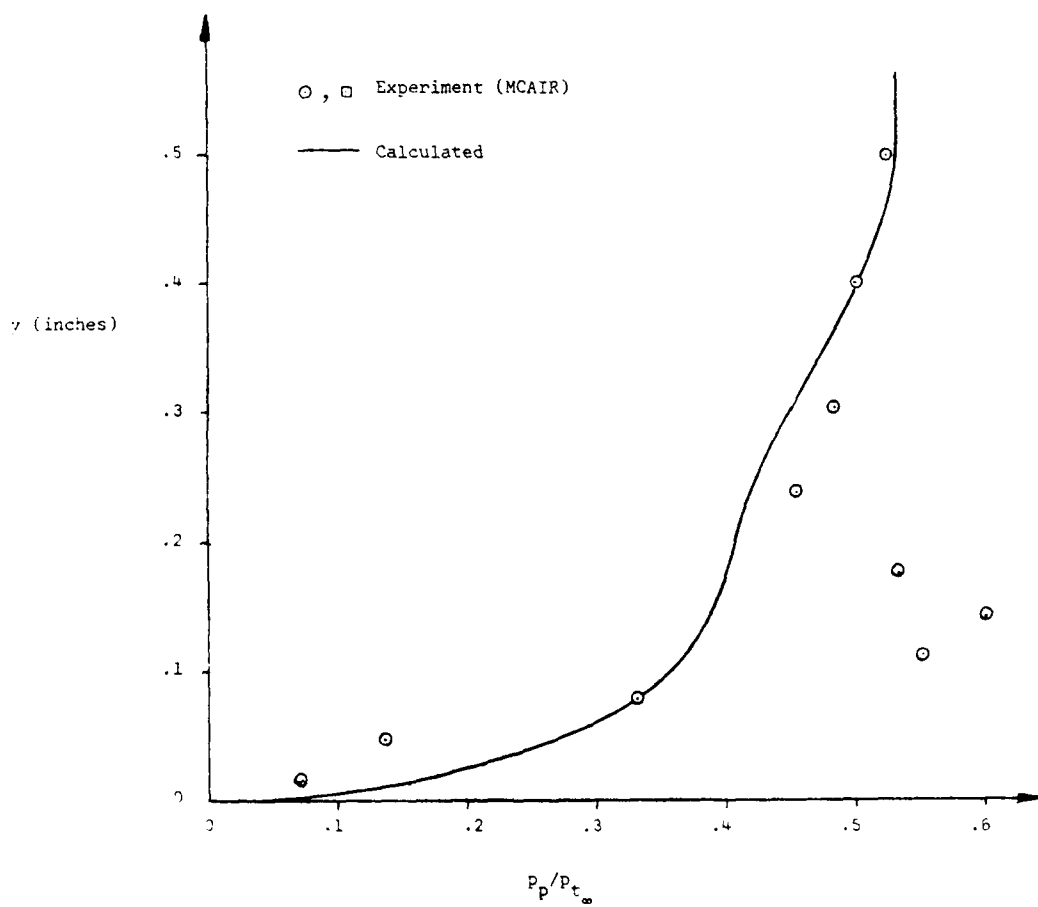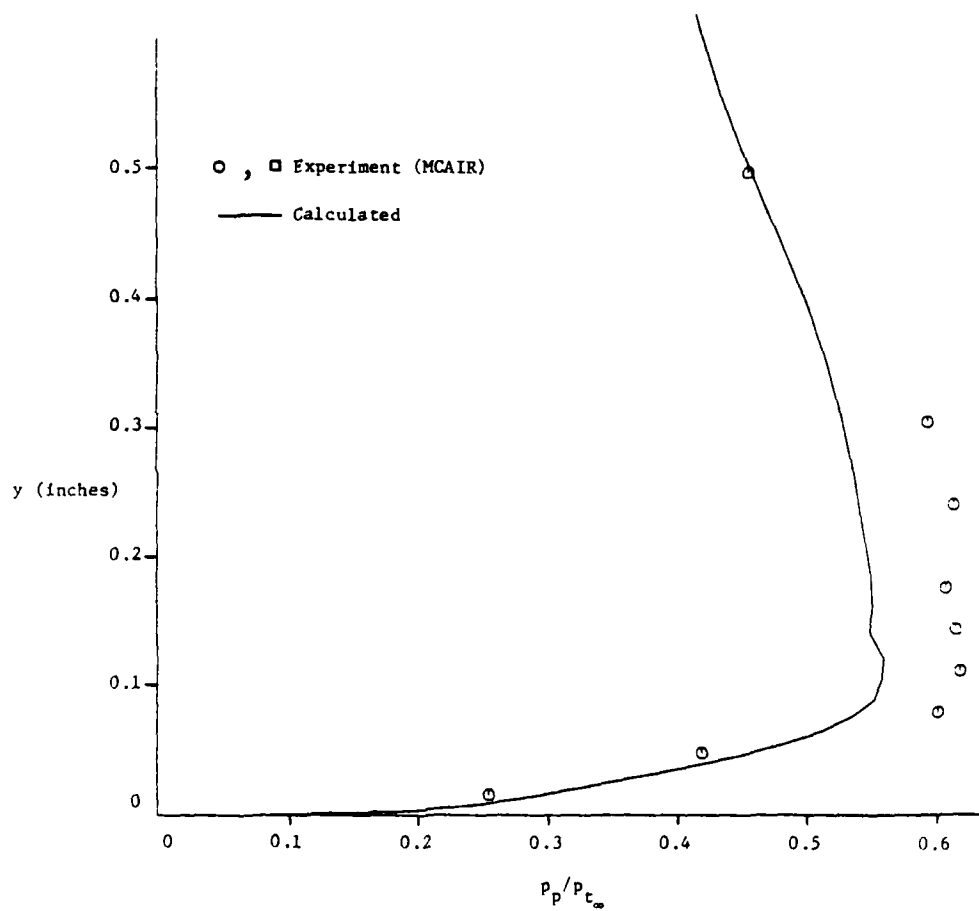
Figure 23. Pitot Pressure on Cowl at Station 6 for $\delta_c = 6°$
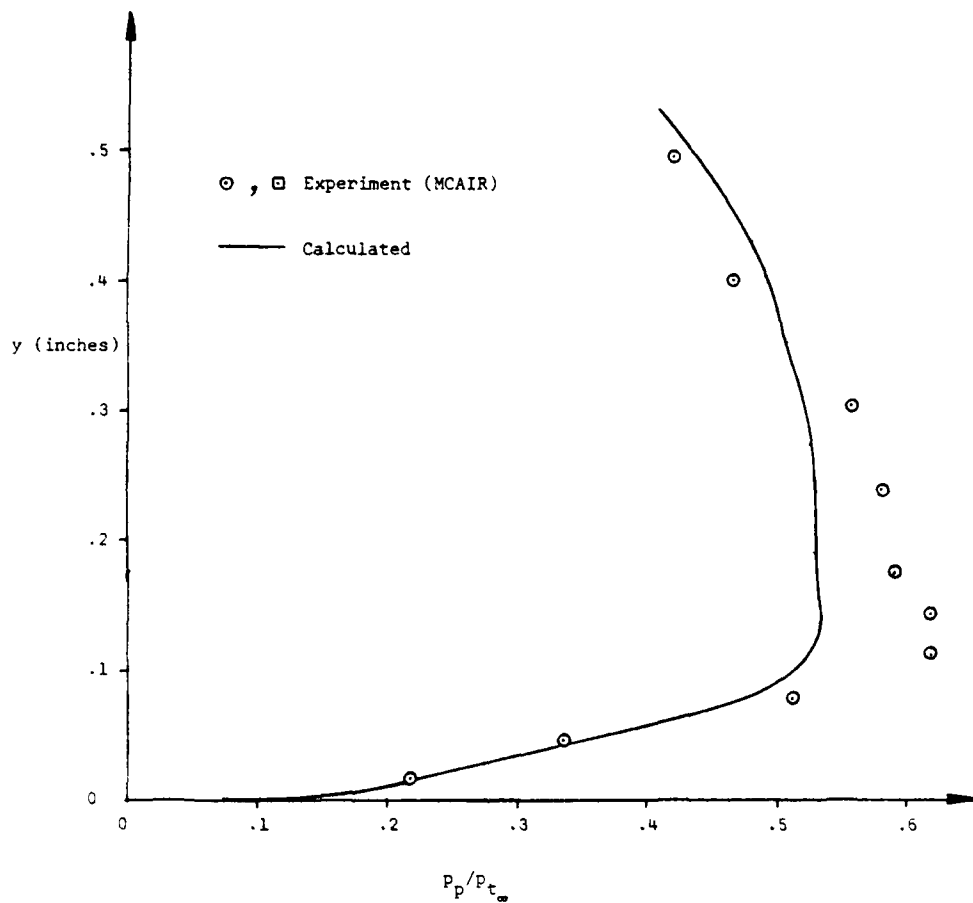
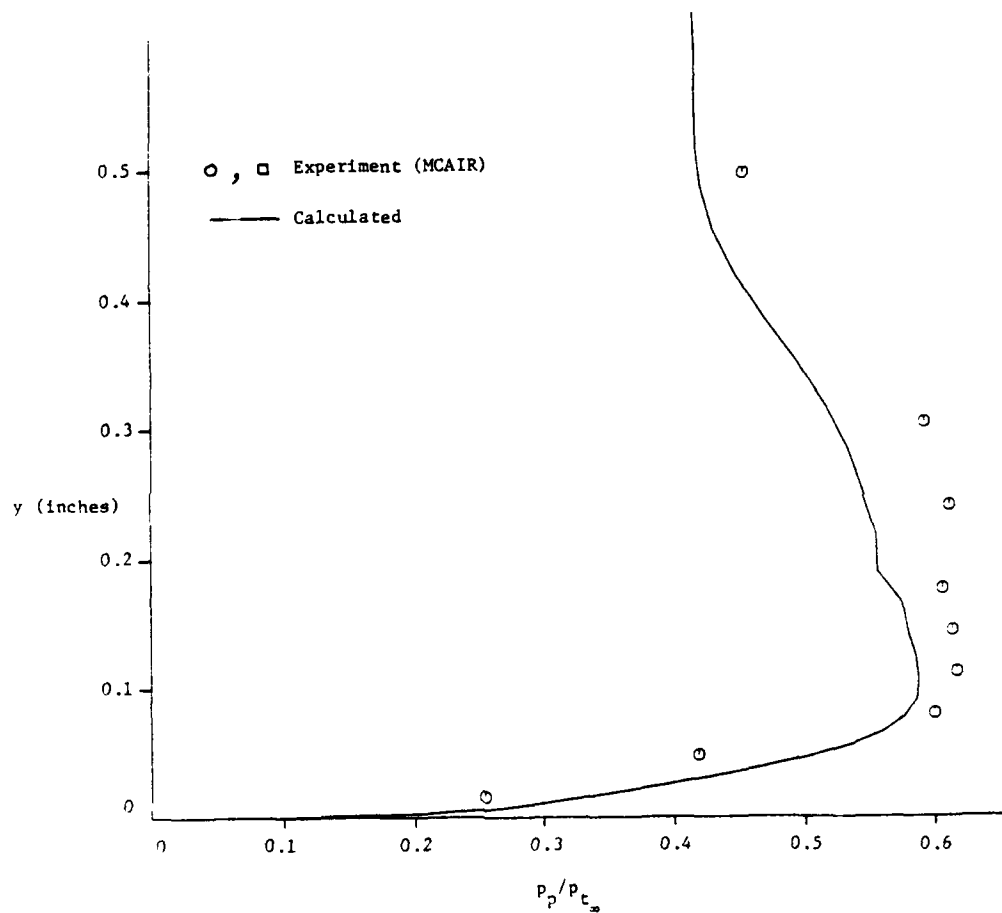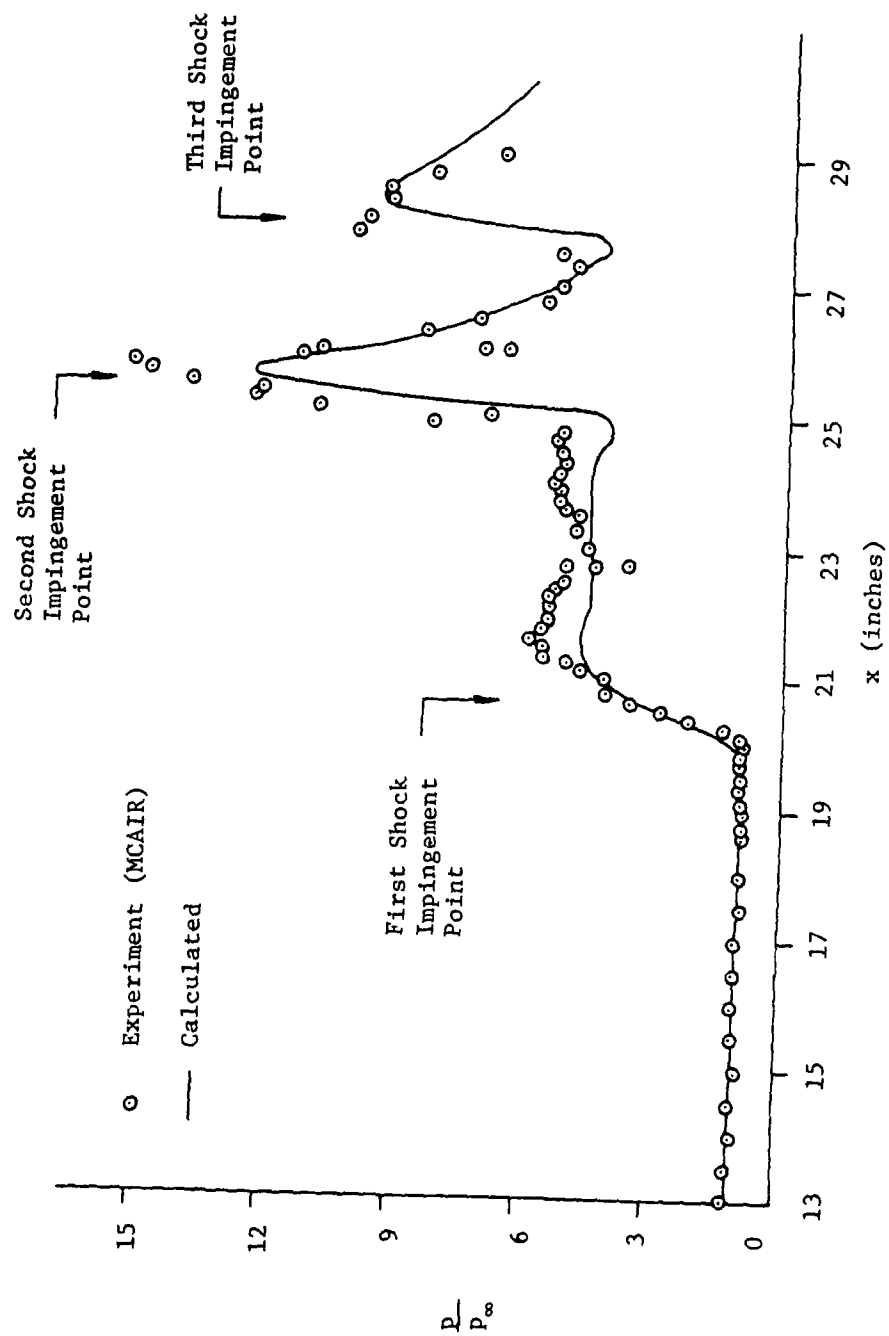Figure 24.   Pitot Pressure on Cowl at Station ⑦
for $\delta_c = 6°$
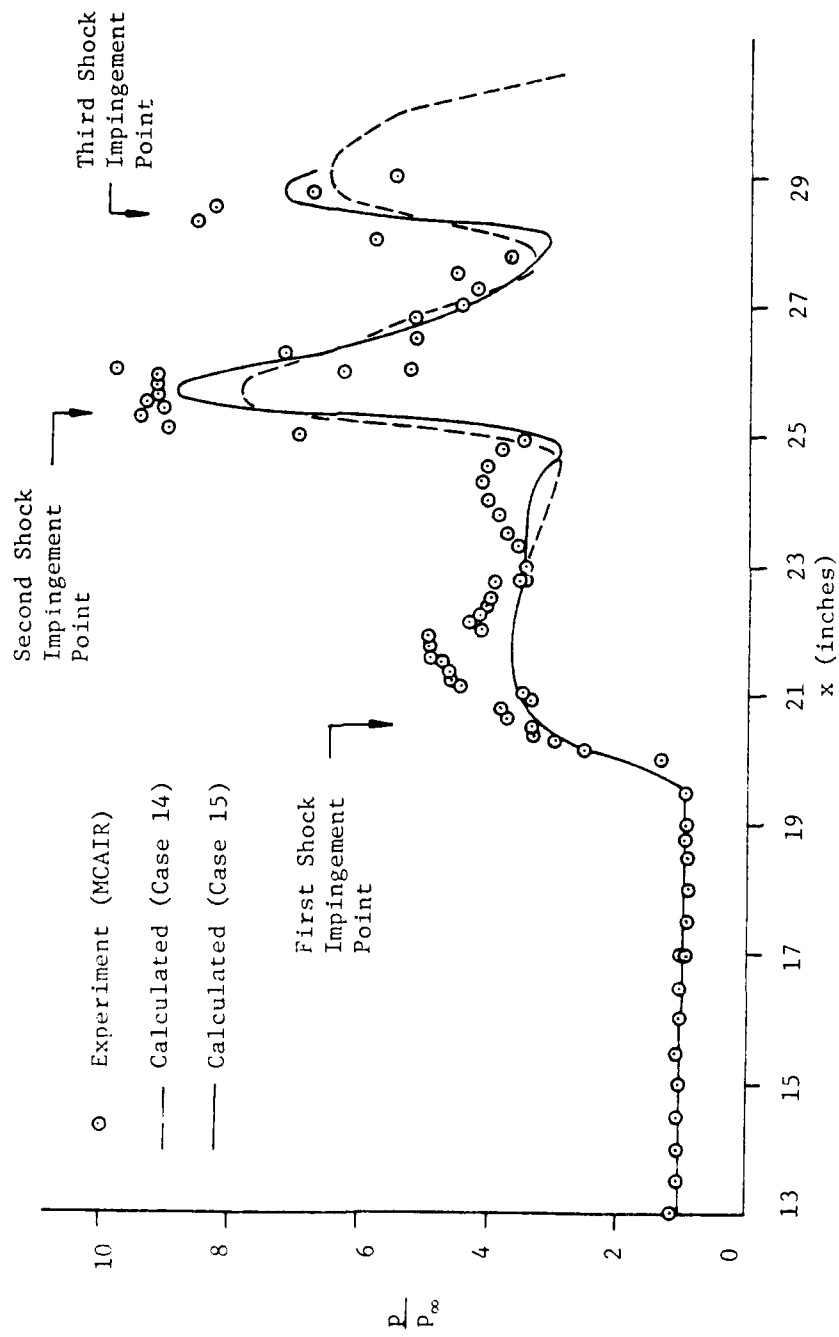
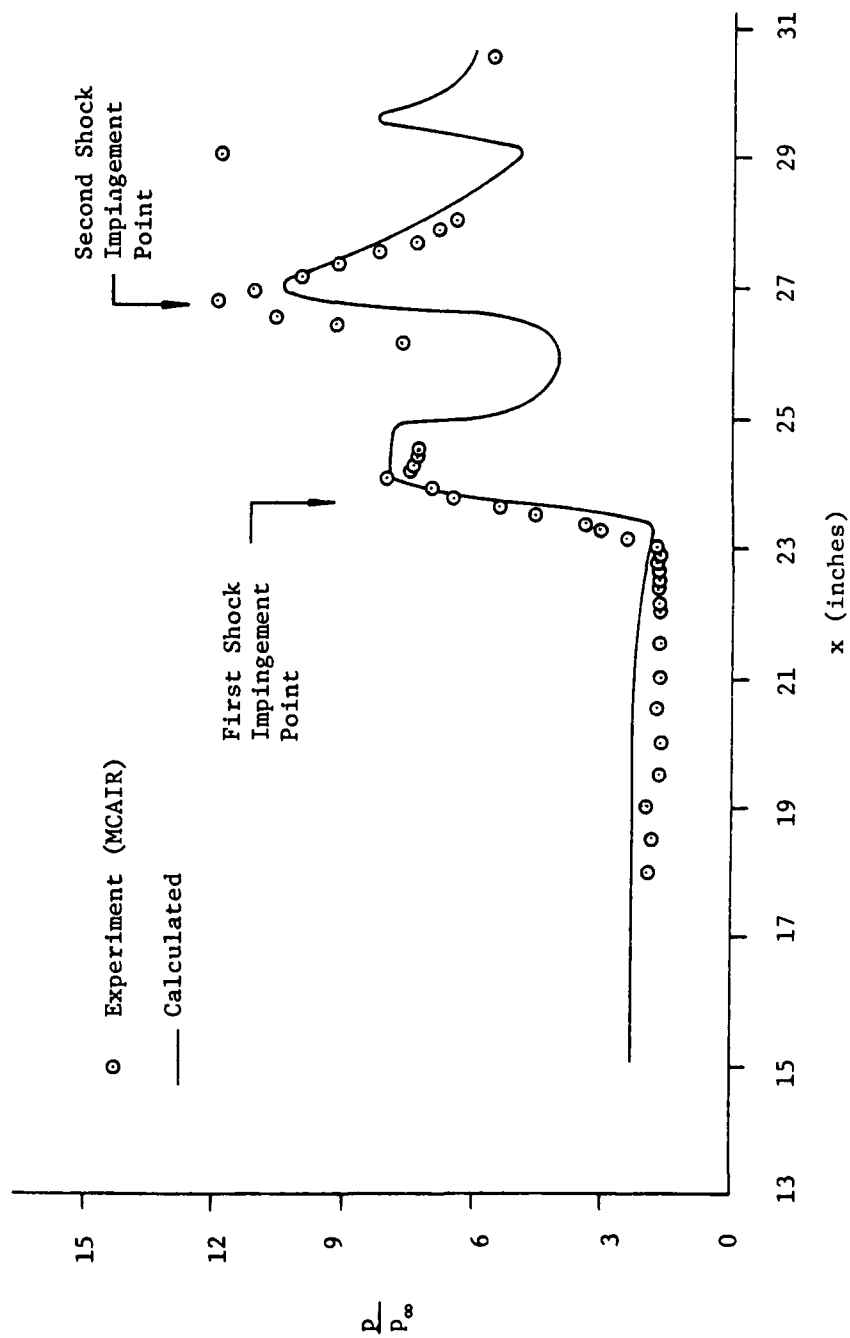Figure 25. Ramp Surface Pressure for $\delta_c = 8°$

73
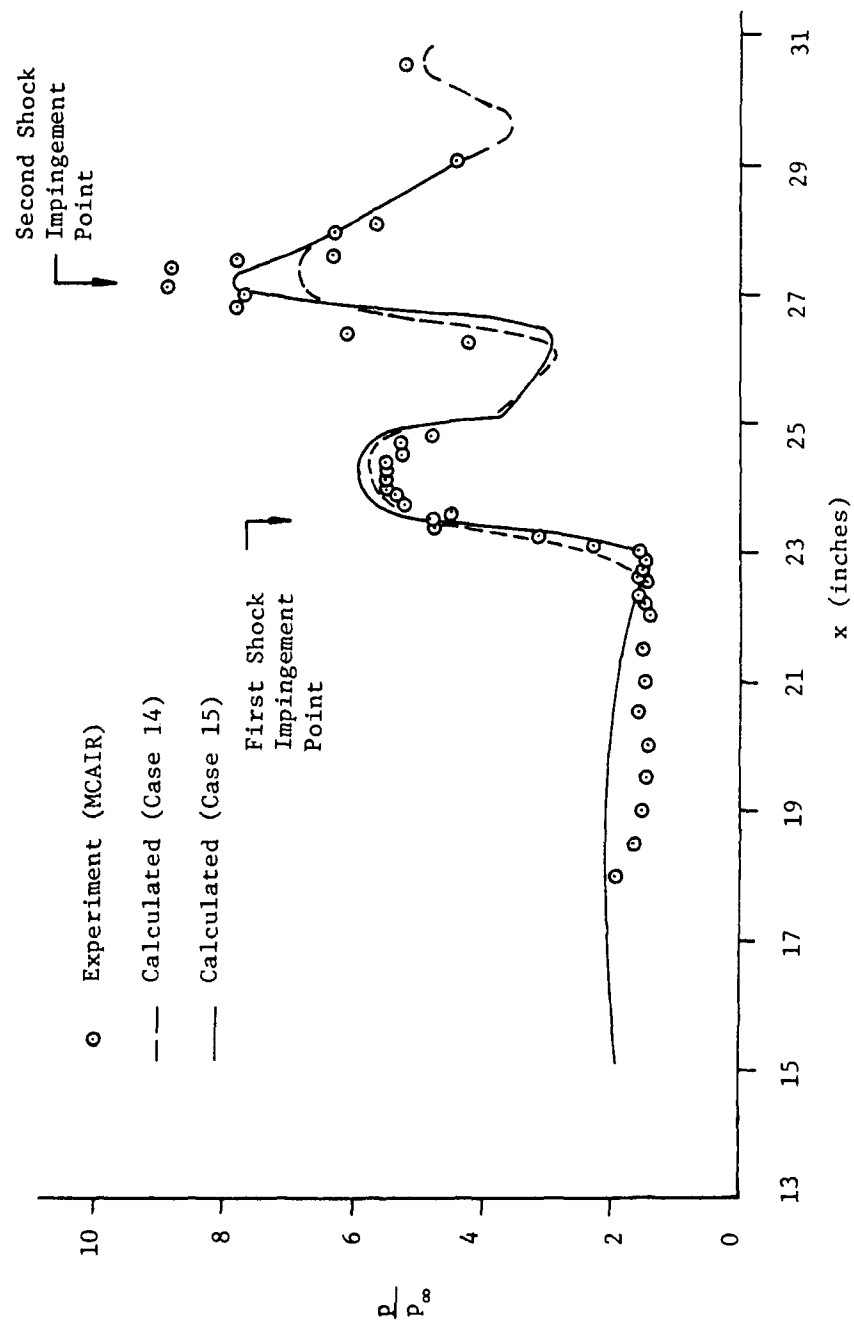
Figure 26. Cowl Surface Pressure for $\delta_c = 8°$
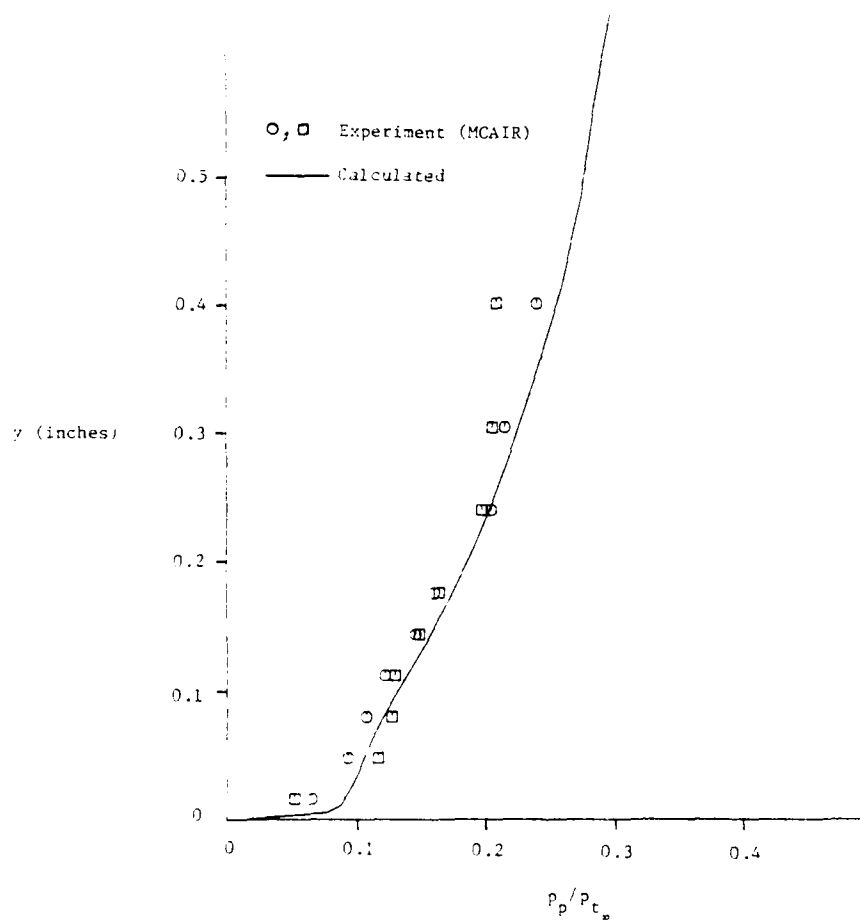
Figure 27a. Pitot Pressure on Ramp at Station ⬜1
for $\delta_c = 8°$ (Case 14)
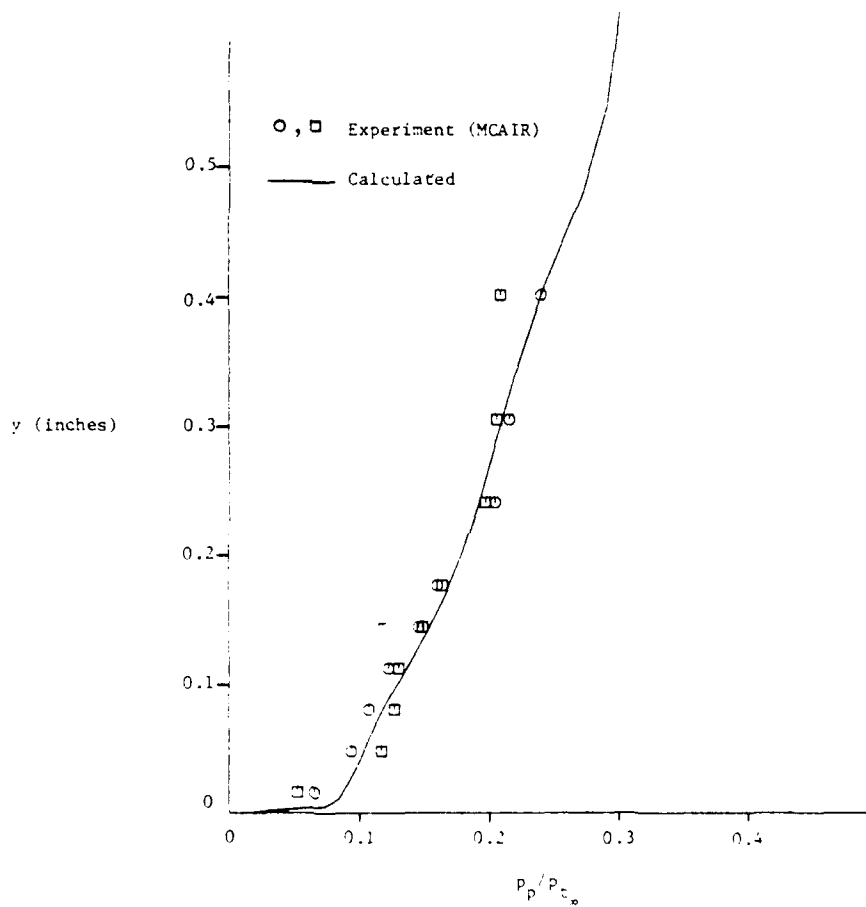
Figure 27b. Pitot Pressure on Ramp at Station ☐1
for $\delta_c = 8°$ (Case 15)
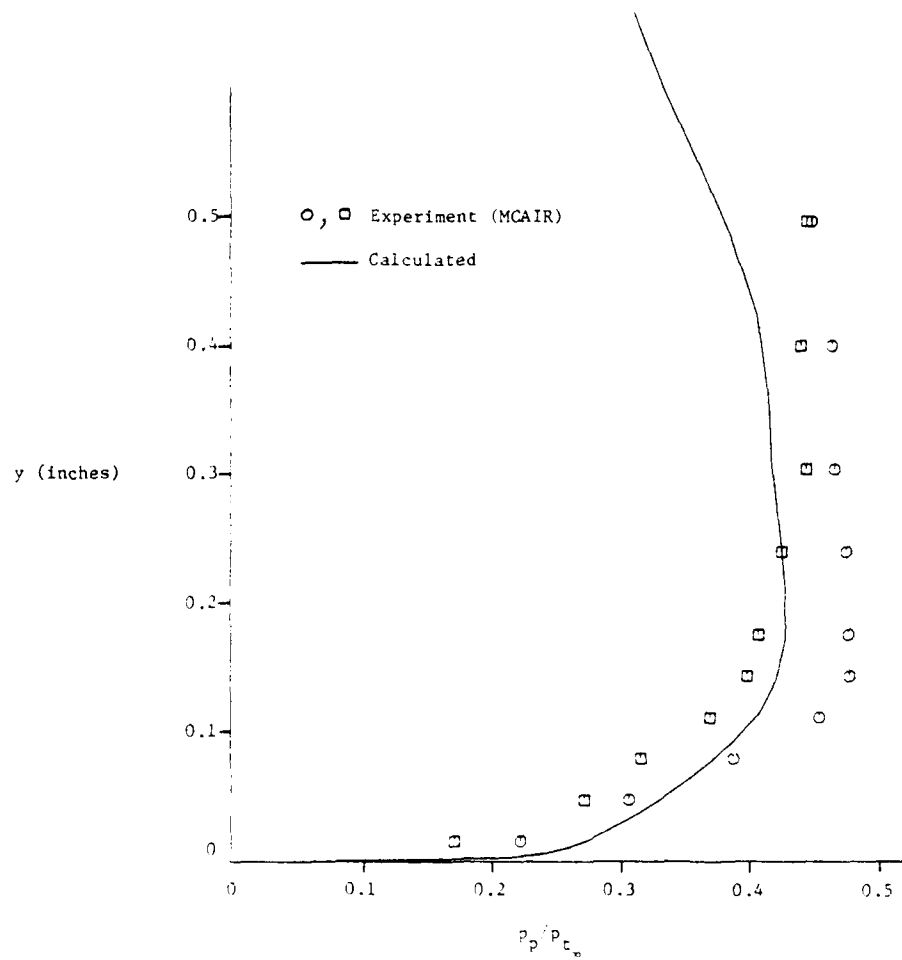
Figure 28a. Pitot Pressure on Ramp at Station ☐2
for $\delta_c = 8°$ (Case 14)

y (inches)   0.3 —

0.2 —

0.1 —

0   0.1   0.2   0.3   0.4   0.5

p_p / p_{t_2}
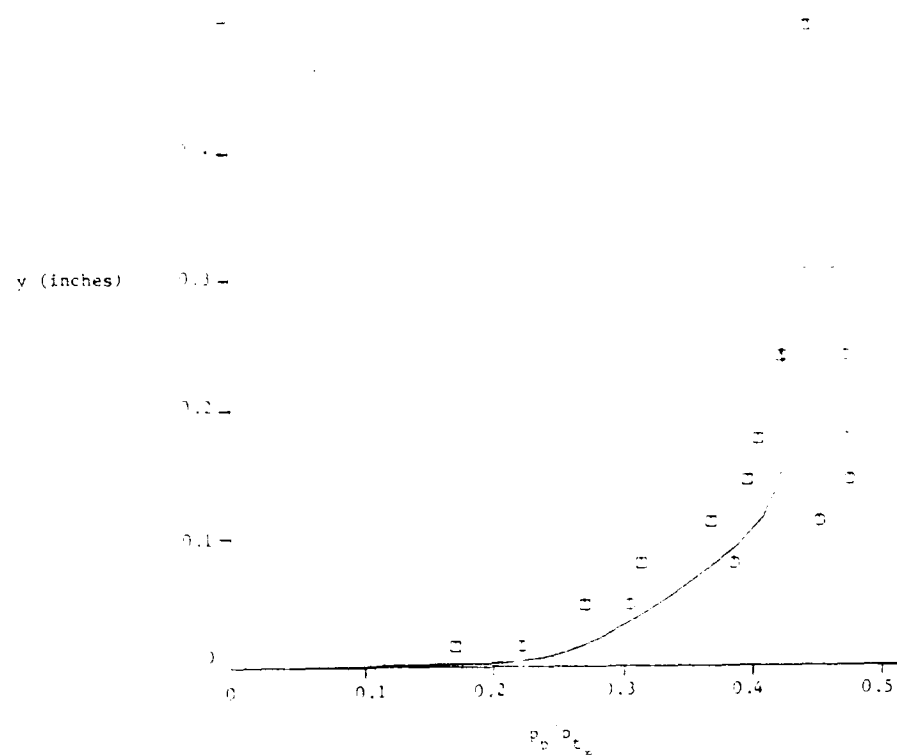
Figure 28b.   Pitot Pressure on Rump at Station 2
              for $\delta_c = 8°$ (Case 15)

78
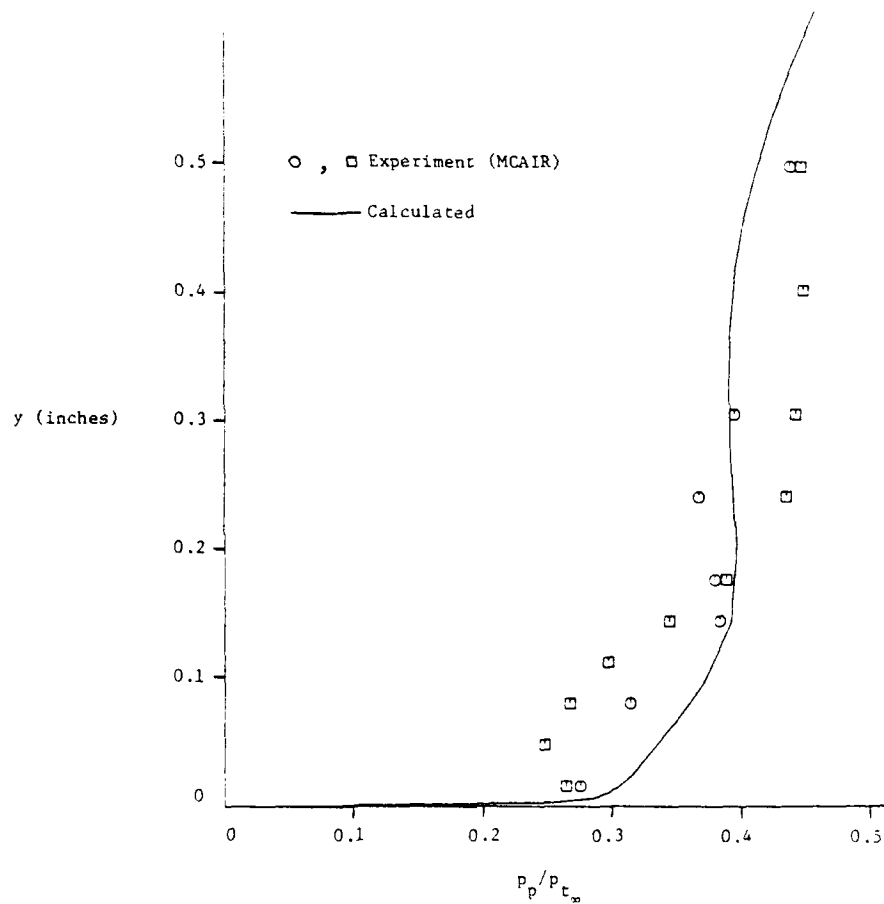
Figure 29a. Pitot Pressure on Ramp at Station ③
for $\delta_c = 8°$ (Case 14)
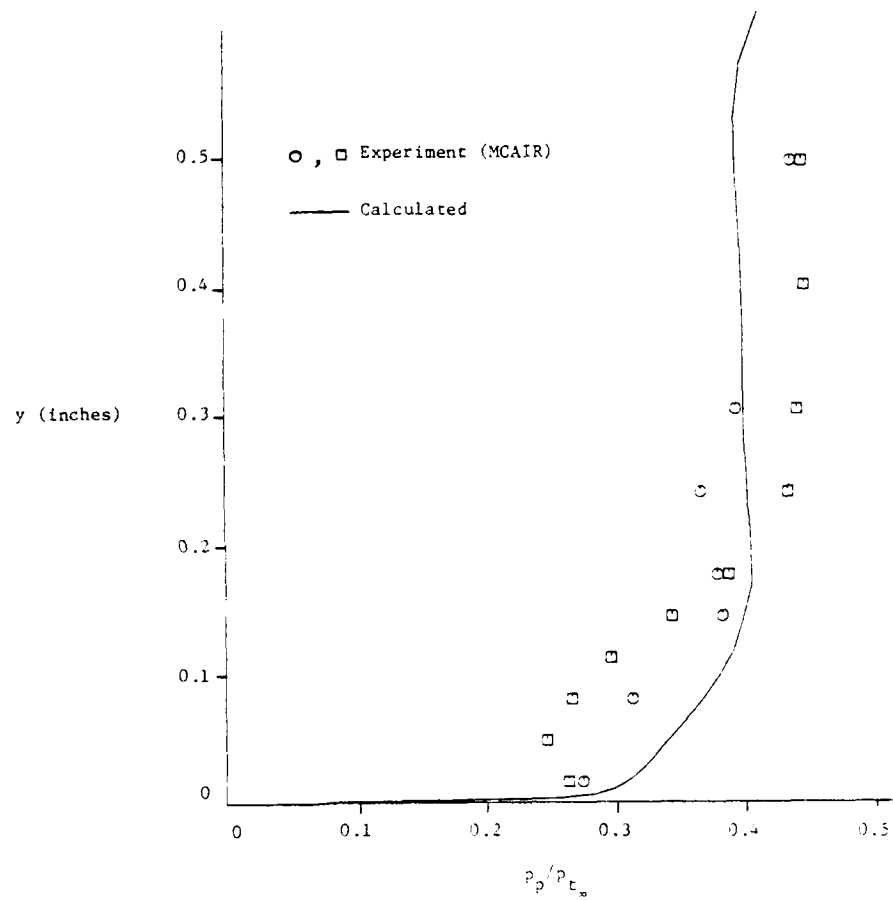
Figure 29b. Pitot Pressure on Ramp at Station $\boxed{3}$
for $\delta_c = 8°$ (Case 15)
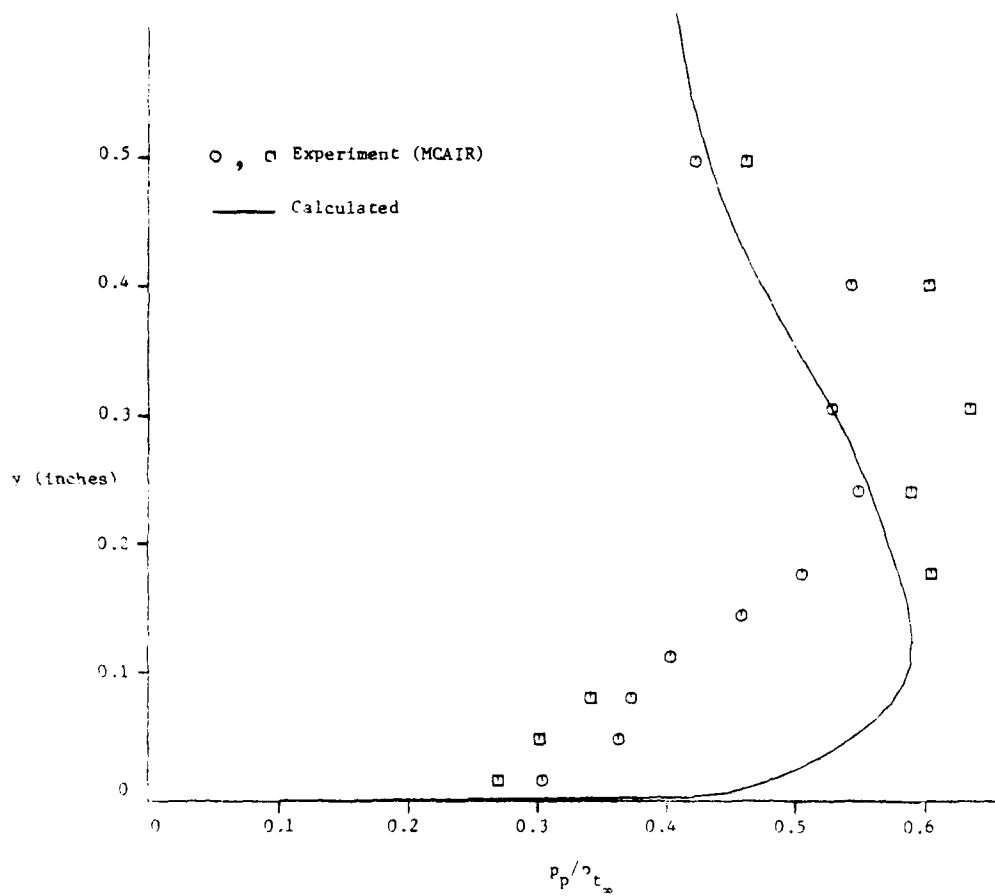
Figure 30a. Pitot Pressure on Ramp at Station [4]
for $\delta_c = 8°$ (Case 14)

2 of 2
AD A
084 789

END
DATE
FILMED
7-80
DTIC
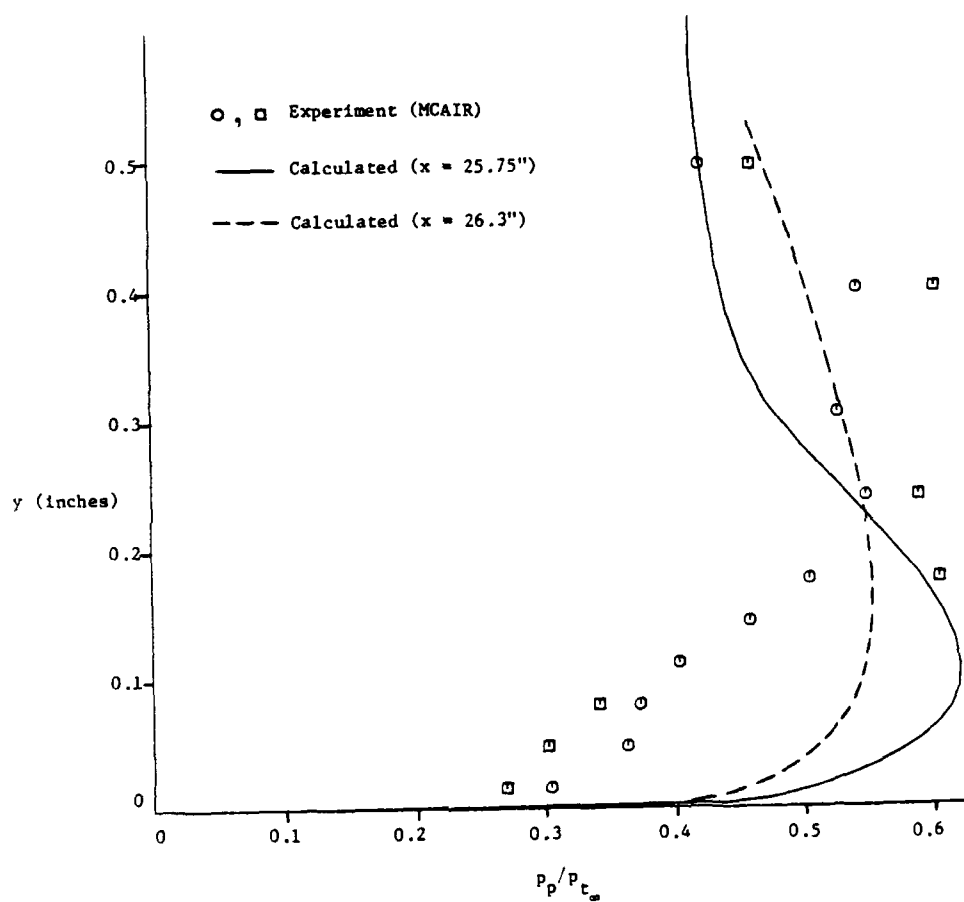
Figure 30b. Pitot Pressure on Ramp at Station $\boxed{4}$
for $\delta_c = 8°$ (Case 15)
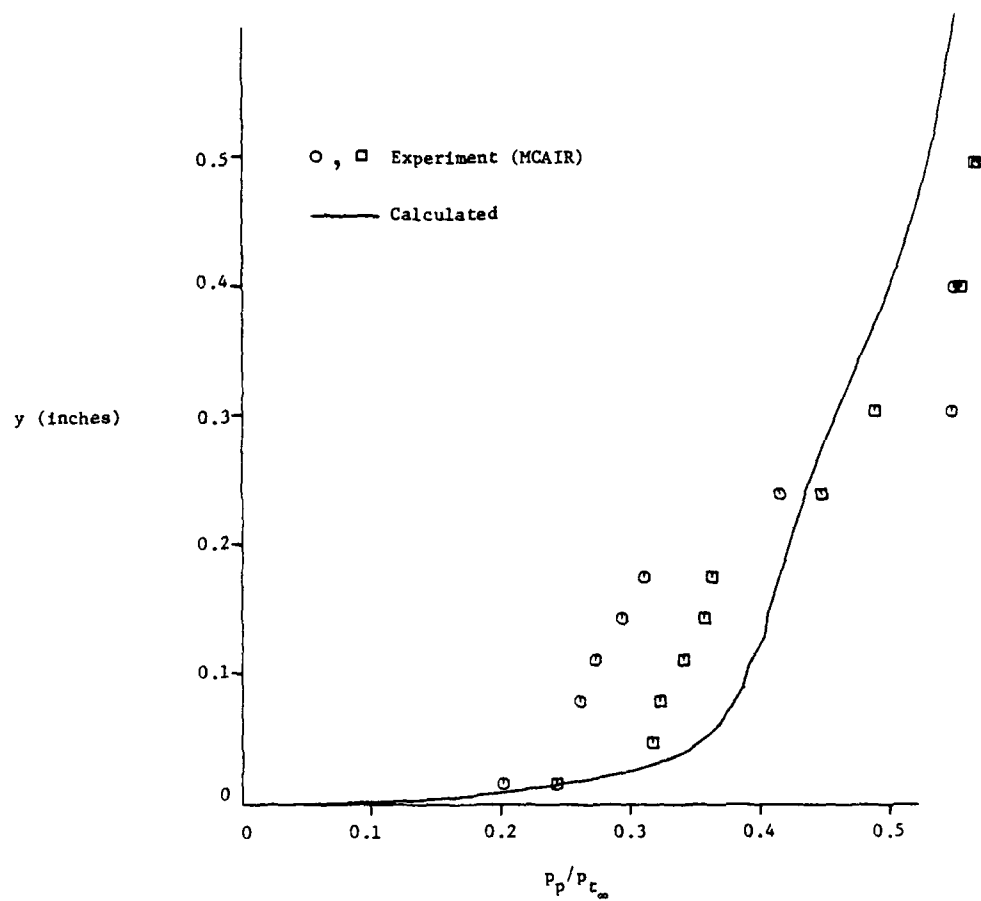
Figure 31a. Pitot Pressure on Ramp at Station [5] for $\delta_c = 8°$ (Case 14)
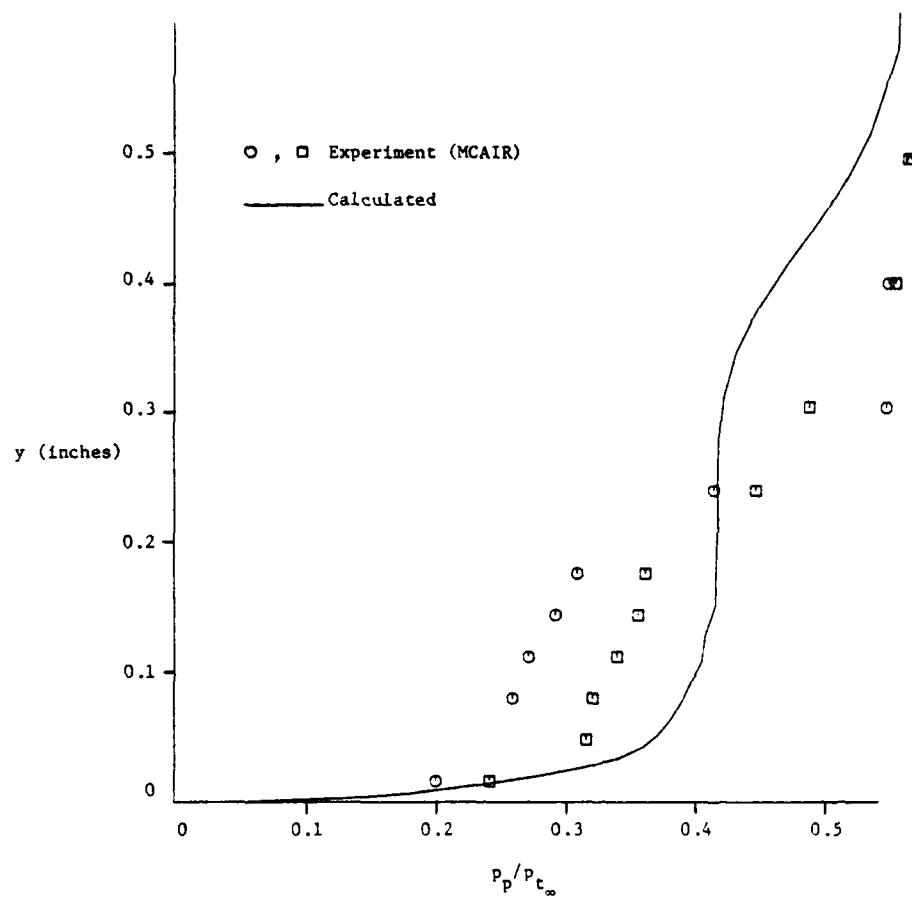
Figure 31b. Pitot Pressure on Ramp at Station $\boxed{5}$ for $\delta_c = 8°$ (Case 15)

84

Figure 32a.   Pitot Pressure on Cowl at Station ⑥
for $\delta_c = 8°$ (Case 14)
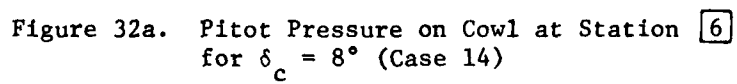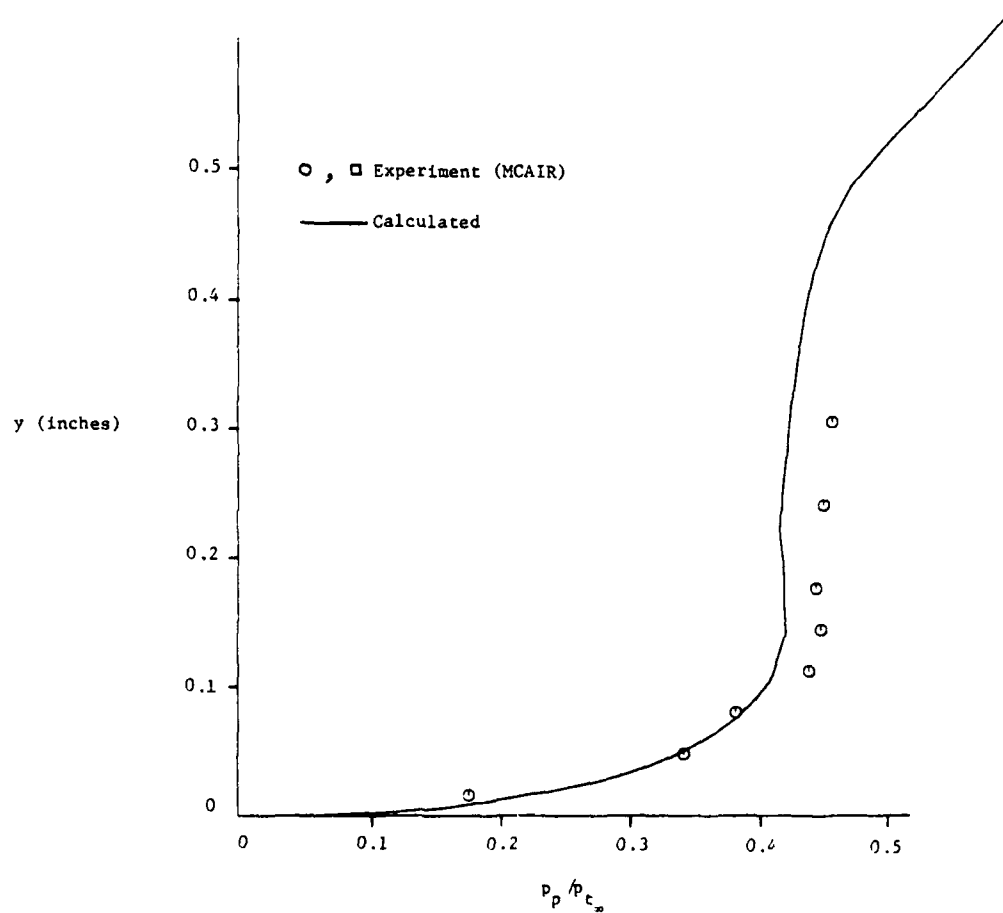
Figure 32b. Pitot Pressure on Cowl at Station $\boxed{6}$ for $\delta_c = 8°$ (Case 15)

Figure 33a. Pitot Pressure on Cowl at Station $\boxed{7}$
for $\delta_c = 8°$

Figure 33b.   Pitot Pressure on Cowl at Station $\boxed{7}$
for $\delta_c = 8°$ (Case 15)

Figure 34. Ramp Surface Pressure for $\delta_c = 10°$

Figure 35. Cowl Surface Pressure for $\delta_c = 10°$

90
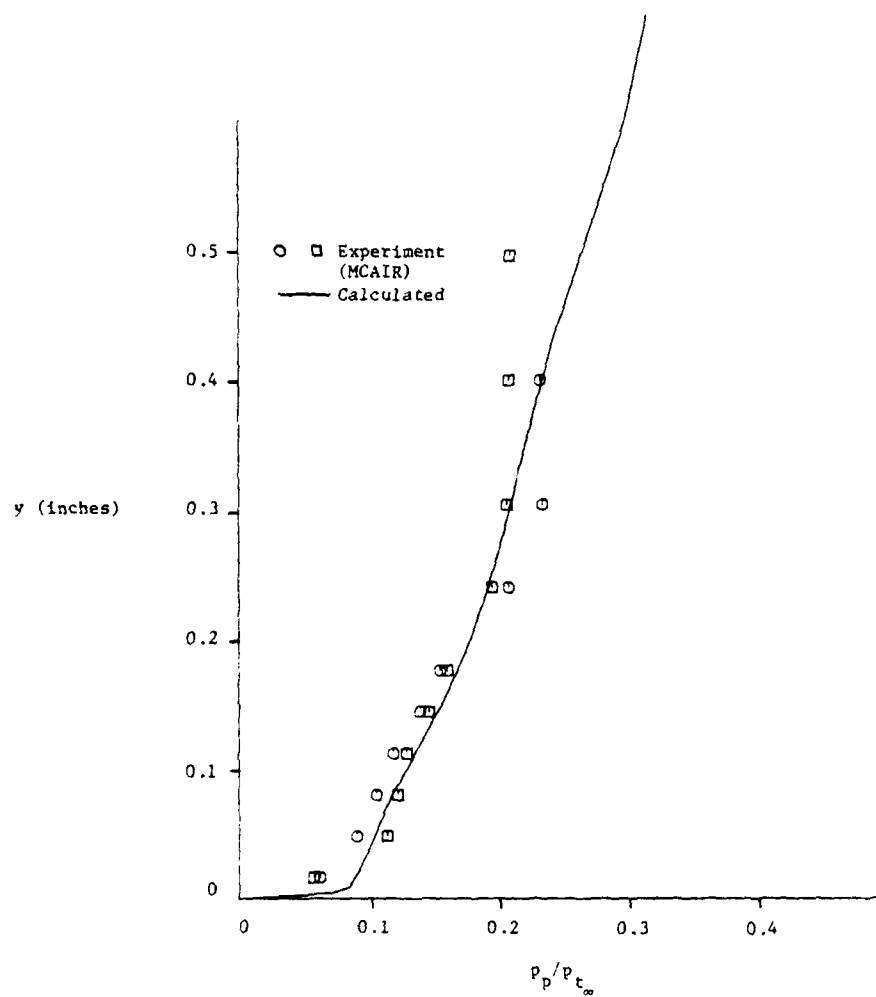
Figure 36. Pitot Pressure on Ramp at Station $\boxed{1}$
for $\delta_c = 10°$
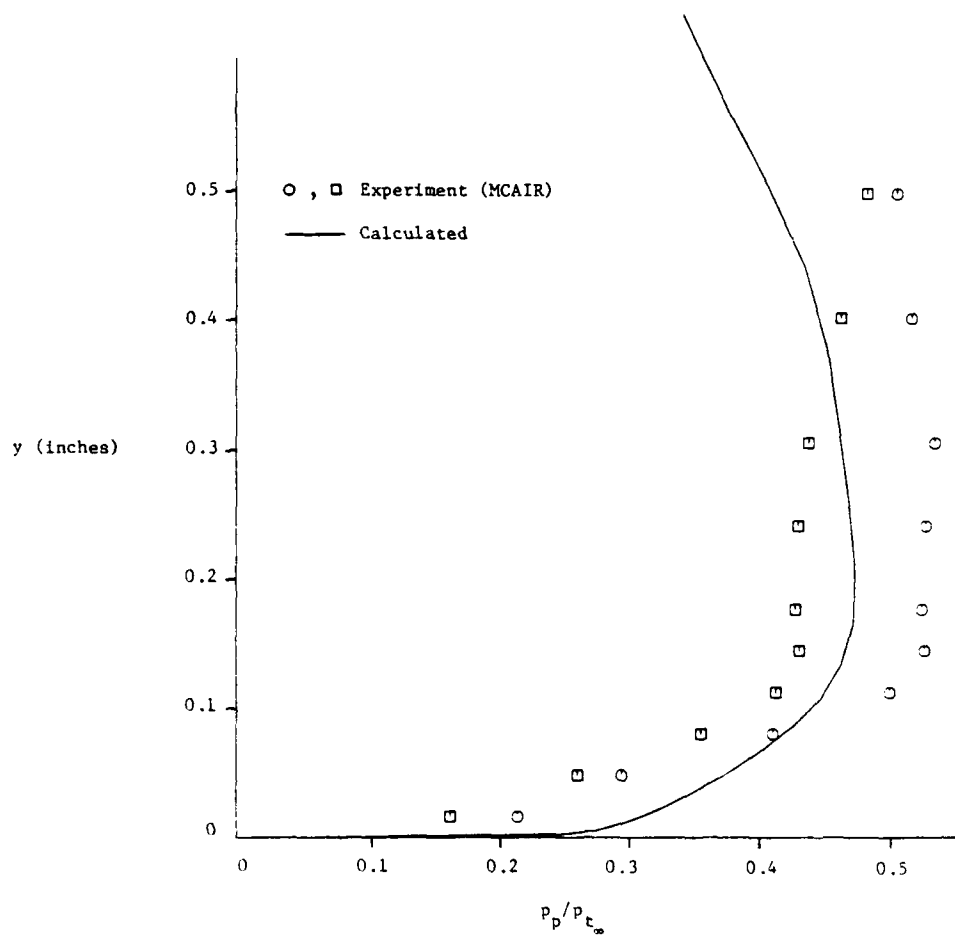
Figure 37. Pitot Pressure on Ramp at Station $\boxed{2}$
for $\delta_c = 10°$
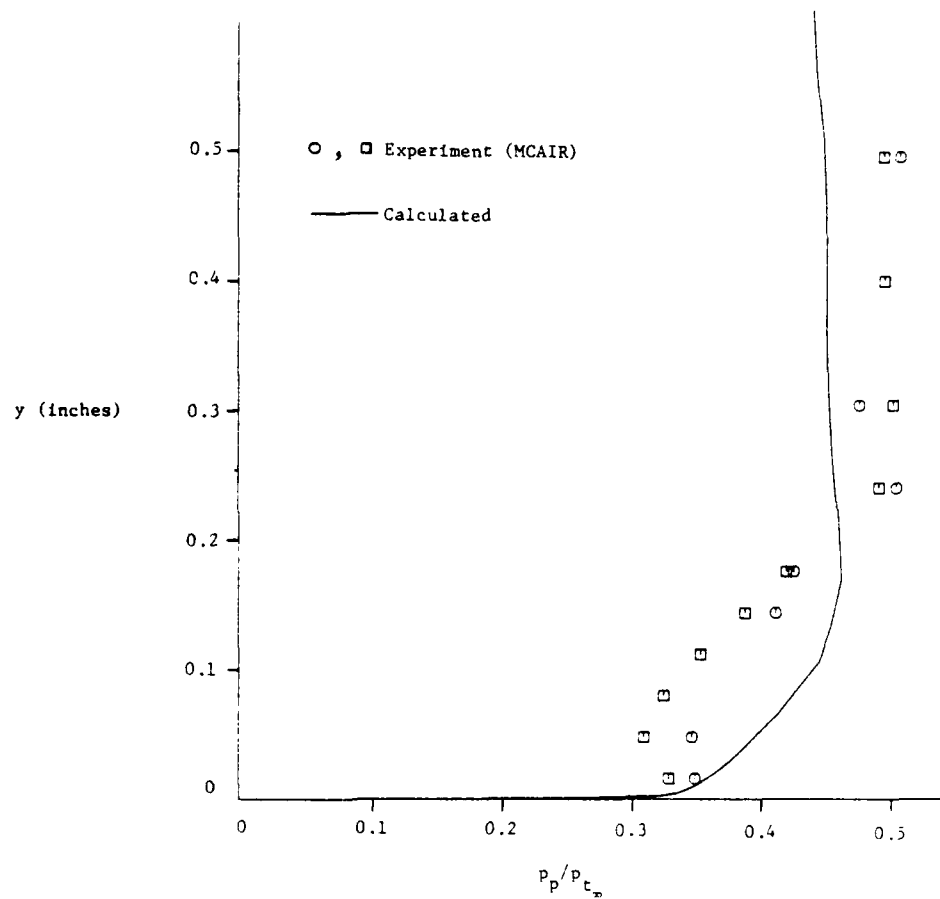
Figure 38. Pitot Pressure on Ramp at Station $\boxed{3}$ for $\delta_c = 10°$

93
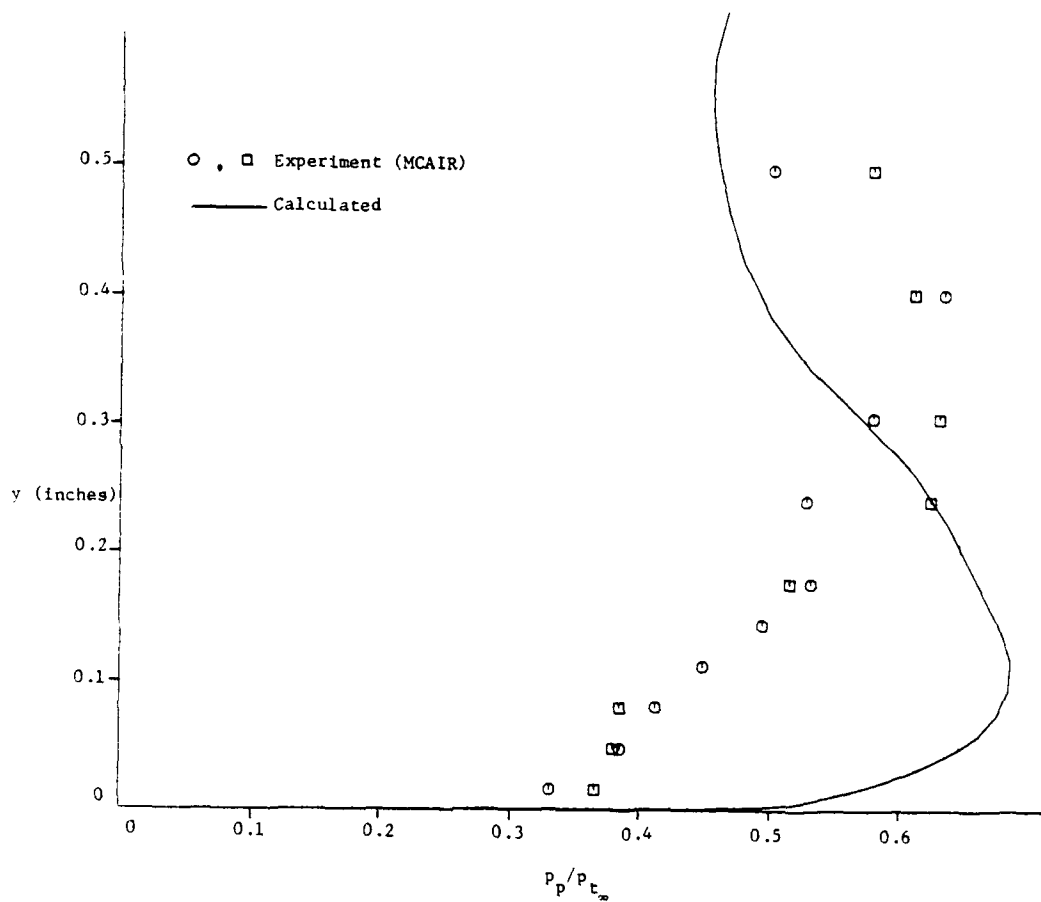
Figure 39.   Pitot Pressure on Ramp at Station $\boxed{4}$
             for $\delta_c = 10°$
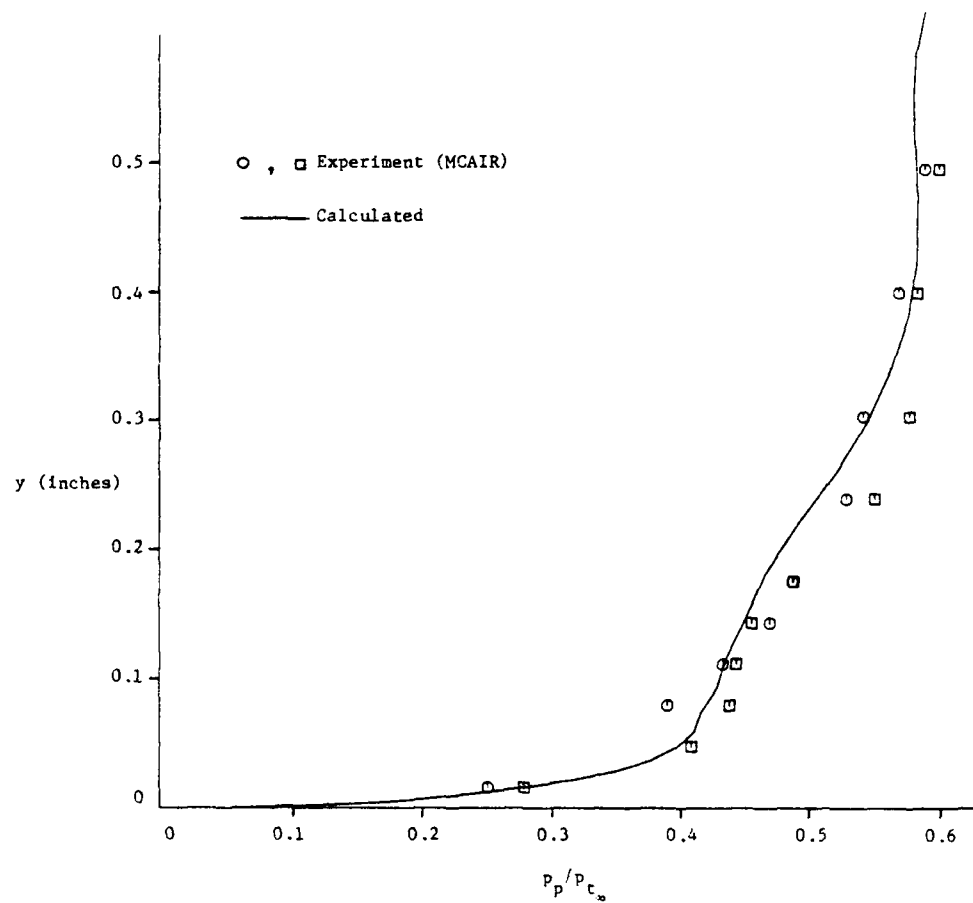
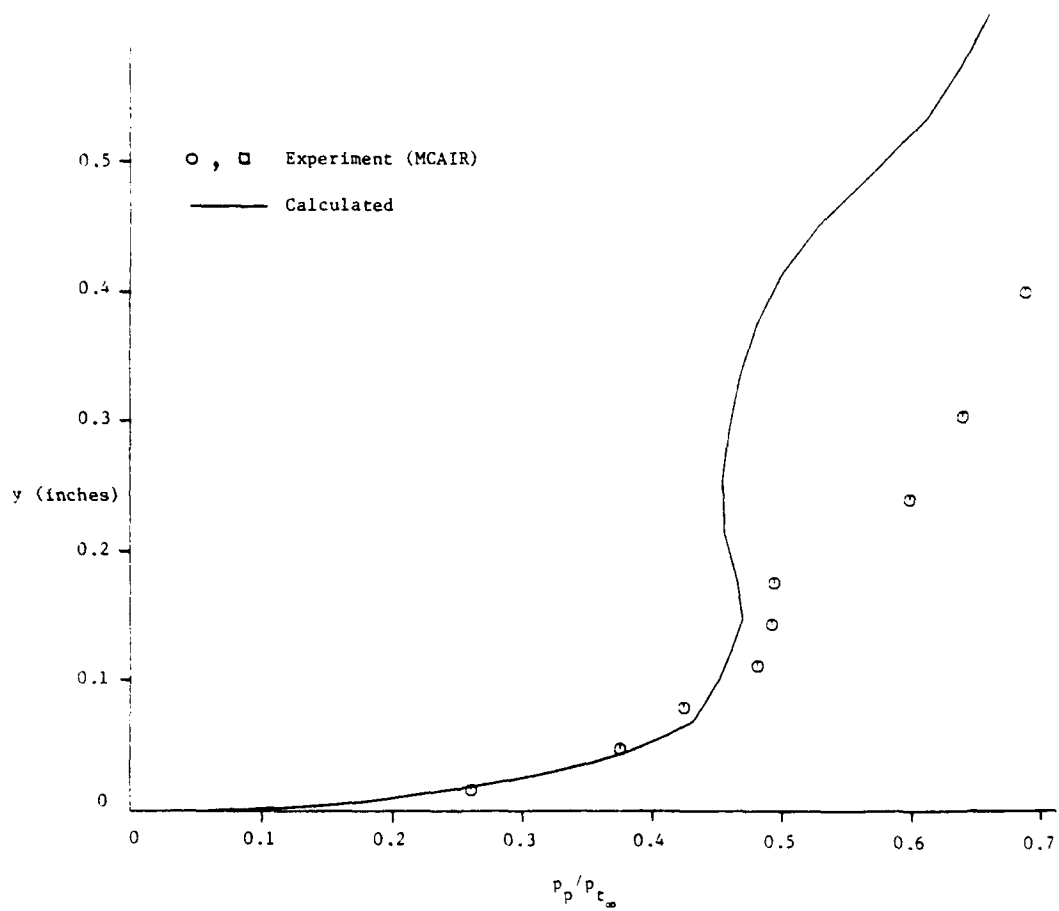Figure 40. Pitot Pressure on Ramp at Station [5]
for $\delta_c = 10°$

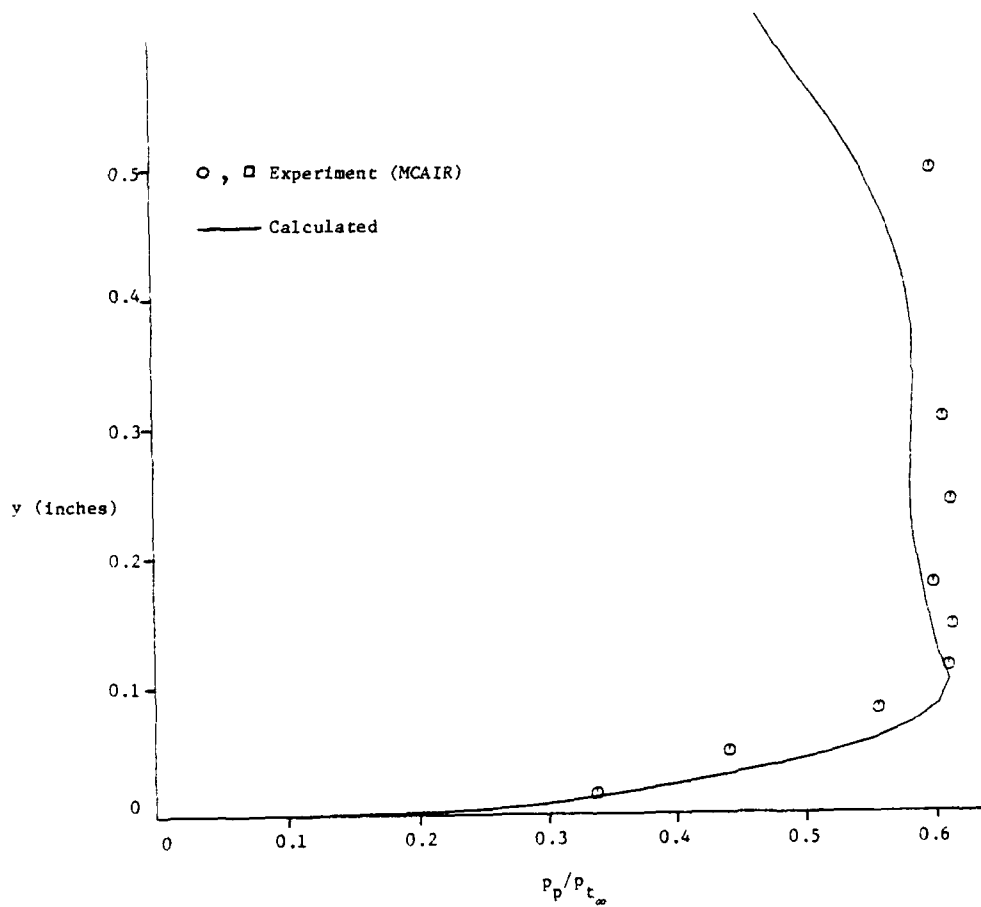Figure 41. Pitot Pressure on Cowl at Station 6
for $\delta_c = 10°$

Figure 42. Pitot Pressure on Cowl at Station ⑦
for δ_c = 10°

97